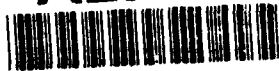


AD-A278 739



FORMATION PAGE

Form Approved
OMB No. 0704-0188

②

to average 1 hour per response, including the time for reviewing instructions, searching existing data sources, gathering the collection of information. Send comments regarding this burden estimate or any other aspect of this form, to Washington Headquarters Services, Directorate for Information Operations and Reports, 1215 Jefferson Avenue, Suite 1204, Washington, DC 20540-6031, and to the Office of Management and Budget, Paperwork Reduction Project (0704-0188), Washington, DC 20503.

1. AGENCY USE ONLY (Leave blank)		2. REPORT DATE March 25, 1994		3. REPORT TYPE AND DATES COVERED Final Report 7/1/91 - 9/30/93	
4. TITLE AND SUBTITLE (U)RECOVERY OF FROZEN FLOW LOSSES IN ARCJETS				5. FUNDING NUMBERS PE -61102F PR - 2308 SA-AS G-AFOSR-91-0318	
6. AUTHOR(S) V. V. Subramaniam					
7. PERFORMING ORGANIZATION NAME(S) AND ADDRESS(ES) The Ohio State University, Dept. of Mech. Eng. Office of Sponsored Programs 1960 Kenny Road, Columbus, Ohio 43210				8. PERFORMING ORGANIZATION REPORT NUMBER AFOSR-TR- 94 0259 RF725071/769221	
9. SPONSORING/MONITORING AGENCY NAME(S) AND ADDRESS(ES) AFOSR/NA 110 Duncan Avenue, Suite B115 Bolling AFB, DC 20332-0001				10. SPONSORING/MONITORING AGENCY REPORT NUMBER	
11. SUPPLEMENTARY NOTES					
12a. DISTRIBUTION / AVAILABILITY STATEMENT Approved for public release; distribution is unlimited				12b. DISTRIBUTION CODE	
13. ABSTRACT (Maximum 200 words) This research explores ways of reducing frozen flow losses via state-resolved numerical simulations (quasi 1-D, 2D, and 2D with swirl). Frozen flow losses in molecular vibration, rotation, and electronic excitation are believed to account for significant losses in thrust and efficiency of arcjet thrusters. This report summarizes the accomplishments in the first two years of a four year research program designed to quantify frozen flow losses, and to generate design tools useful for the designer to enhance arcjet performance.					
14. SUBJECT TERMS Frozen Flow losses, arcjets, plasma thrusters, numerical simulations, supersonic reacting flows				15. NUMBER OF PAGES	
				16. PRICE CODE	
17. SECURITY CLASSIFICATION OF REPORT Unclassified	18. SECURITY CLASSIFICATION OF THIS PAGE Unclassified	19. SECURITY CLASSIFICATION OF ABSTRACT Unclassified	20. LIMITATION OF ABSTRACT UL		

DTIC
SELECTE
APR 29 1994
S B D

DTIC QUALITY INSPECTED 3

94-12917



94 4 28 038

TABLE OF CONTENTS

Approved for public release;
distribution unlimited.

1.0	INTRODUCTION	2
2.0	BACKGROUND	3
3.0	RESEARCH OBJECTIVES	6
4.0	STATUS OF RESEARCH EFFORT	6
4.1	ACCOMPLISHMENTS FROM FIRST TWO YEARS	6
4.2	ON-GOING AND FUTURE WORK	8
5.0	REFERENCES	9
6.0	PERSONNEL	12
7.0	INTERACTIONS	12

Appendix A:	A-1
Appendix B:	B-1
Appendix C:	C-1

Accession For	
NTIS GRA&I	<input checked="" type="checkbox"/>
DTIC TAB	<input type="checkbox"/>
Unannounced	<input type="checkbox"/>
Justification	
By _____	
Distribution/ _____	
Availability Codes	
Dist	Avail and/or Special
A-1	

RECOVERY OF FROZEN FLOW LOSSES IN ARCJETS

Grant No. AFOSR-91-0318

**Final Technical Report
(1991-1993)**

**V. V. Subramaniam, V. Babu, and S. Aithal
Department of Mechanical Engineering
The Ohio State University
Columbus, Ohio 43210**

1.0 INTRODUCTION

The recent successful commercial launch of two 1.8 KW hydrazine arcjet thrusters on AT&T's TELSTAR IV satellite marks a new era in electric propulsion. The arcjet's key contribution in the commercial sector is in reduced launch costs and extended satellite operational lifetime. This is achieved primarily by increasing the specific impulse above that of conventional chemical thrusters. For military applications however, launch costs are a secondary concern compared to extended satellite lifetime for multiple missions and quick response to mission goal changes. These military applications will require arcjets capable of operation over a wide range of powers from ~1 KW up to ~50 KW. Present understanding of arcjet physics, arcjet design, and arcjet performance especially with regard to scale-up with input power level. This report describes progress made during the first two years of a four-year research program designed to address these issues.

The arcjet thruster is one in a class of electrothermal devices that generates thrust by ohmic heating of the subsonic propellant stream, followed by rapid expansion to supersonic speeds. An important distinction between these thrusters and conventional chemical thrusters is the fact that the input electrical energy is transferred to the propellant via Ohmic or Joule heating, as opposed to combustion. However, the arcjet shares a key feature in common with its chemical thruster counterparts, namely, frozen flow losses.

Frozen flow losses refers to the fraction of input energy that is added to the propellant gas flow which *does not* appear in the form of exit kinetic energy (i.e. translational energy). The thrust generated derives solely from this exit kinetic energy. Fig. 1 shows how the input electrical energy is partitioned into several channels. It is clear that only a fraction of the input energy

surfaces as useful work done by the thrust force. Frozen flow losses include penalties associated with dissociation of propellant molecules, ionization processes, electronic excitation of molecules/atoms, and vibrational/rotational excitation of molecules. Each of these processes has a characteristic relaxation time associated with it, and the resulting non-equilibrium effects are drastically coupled to the flow field. The term "non-equilibrium" has been freely given different meanings in the electric propulsion community. For this reason, the type of non-equilibrium phenomena of relevance to arcjet flows is clarified in the following section, followed next by a description of completed and on-going research.

This final report summarizes the research performed under grant no. 91-0318, during the period September 1991 - September 1993.

2.0 BACKGROUND

Although early tests of arcjet thrusters in the 1960s contributed to the development of a prototype device[1-4], dangerous halting of further development in the 1970s with subsequent revival of space-based defense concepts in the 1980s have led to stagnation in fundamental understanding of the operating characteristics and performance of these devices. In the mid-1980s therefore, the 1 KW and 30 KW designs from the 1960s were revived, tested for lifetime and endurance using ammonia as the propellant, and appeared to meet the mission requirement ($I_{sp} \sim 800s$) set by the SDIO[5]. However, in 1990, systematic errors were discovered in the thrust measurements made at JPL which led to performance evaluations that failed to meet the mission criteria for the ammonia arcjet. Consequently, *all* research efforts in the U.S. turned toward the hydrogen arcjet which could easily generate specific impulses on the order of 1500s. **This work was proposed at that time with the following simple argument in mind.** Although the ammonia arcjet had an I_{sp} far lower than the hydrogen arcjet, propellant storage and storage cost considerations favor the ammonia arcjet over the hydrogen arcjet. Any gain in I_{sp} in the ammonia arcjet would therefore be a benefit, in addition to the ease of storage and lowering propellant storage costs. Unfortunately, polyatomic propellants such as ammonia usually react to form significant amounts of highly vibrationally excited diatomic species. Thus, a substantial amount of the input electrical energy is lost in frozen flow (i.e. rotational, vibrational, and electronic mode non-equilibrium). Clearly, if these frozen flow losses are to be reduced and if sustained operation is to be achieved at high power levels and high specific impulses, a fundamental understanding of the transport and chemical processes is necessary. Scale-up in power is not possible without consideration of the disequilibria between internal and translational modes of molecular motion. It is therefore important to define exactly what is meant by a "non-equilibrium" process.

The words "non-equilibrium" are used in the scientific community to denote a process whose characteristic time scale is comparable to (i.e. neither orders of magnitude larger nor smaller than) the time scale set by a flow. There are in general two time scales in a real flowing fluid. The

first is the convective time scale defined as a macroscopic characteristic length (such as constrictor diameter, constrictor length, channel diameter, etc.) divided by a characteristic velocity, and the second is a diffusive time scale defined as the square of a characteristic length divided by the kinematic viscosity. According to classical thermodynamics, a *system* is in equilibrium if there are no gradients in any properties of the fluid. However, when there is a flowing compressible fluid, there are gradients in velocity, density, etc. Consequently, one of the "ideal" flows that is commonly used for model comparisons is one that is in *local* thermodynamic equilibrium. Such an *equilibrium flow* is one in which the time scales for all processes are infinitely smaller than either the convective or diffusive time scale. A second "ideal" flow is "*frozen*" *flow*, which refers to the case where the time scale for a particular process is much longer than the convective or diffusive time scale. Hence, the chemical composition is "frozen" or unchanging.

A given process (i.e. dissociation, ionization, recombination, reaction, etc.) is out of equilibrium in a flow if the time scale for this process is comparable to the convective time scale. Hence it is possible for flows to consist of many processes, some of which are in local thermodynamic equilibrium, some that are frozen, and others that are out of thermodynamic equilibrium. The processes that are out of equilibrium in this sense are called "non-equilibrium processes". Since classical thermodynamics does not account for the rate at which a process may take place, there is no recourse but to resort to the area of chemical kinetics. Chemical kinetics is a term broadly used by many scientists to denote finite-rate reactions (as opposed to infinite rates which correspond to equilibrium conditions, and zero rates which correspond to frozen states). Thus any reaction (to be distinguished from an elementary process or elementary reaction) is described by some rate at which it proceeds. In many applications, reactions are described by overall rates and an overall chemical equation despite the fact that the actual process takes place via several elementary steps.

In reality, chemical processes (dissociation, ionization, recombination, reaction, etc.) proceed at different rates depending on the detailed initial state of the reactants. For atomic reactants this means that the reaction may proceed from a specific electronic configuration or state of the atom. For molecular reactants, the reaction may proceed from **specific vibrational and rotational levels in a specific electronic state**. The rate of such a process or reaction therefore depends on vibrational quantum number and rotational quantum number for a given electronic state. The kinetic rates for such elementary processes are what are known as "*state-specific kinetic rates*". There has been a rapid growth in the generation of state-specific rate data for many molecules over the past decade or so, due in part to the sophisticated diagnostics methods that have been devised. The time is therefore ripe to make use of such detailed and accurate information where available, and to combine them with recent rapid advances in *supercomputing*.

For high speed flows of interest to rocket engines (chemical or electrical), such state-specific information is vital because it determines transport properties (since they are dependent on

the chemical composition of the gas mixture), which are continuously changing due to the varying flow field. However, also of vital importance is the fact that when molecular species are present in high speed flows (and this is true of all molecular propellants in supersonic nozzle flows whether it is a chemical or an electrical thruster), a substantial amount of energy is tied up in the internal modes (vibration, rotation, electronic). This energy is of no use in generating thrust because it is not in translation (i.e. it is not directed kinetic energy). Consequently, energy tied up in these internal modes is "lost", and termed "frozen flow losses". The term "frozen flow losses" is apt because the characteristic relaxation time for the vibrational modes, or rotational modes, or electronic modes are longer than the local convective time scale. Hence, the energy is "frozen" in these modes. This is not to be confused with the "frozen flow" concept addressed earlier which usually refers to non-varying chemical composition.

With the aforementioned definitions and distinctions in mind, the existing literature on arcjet flows can now be reviewed. Several research groups have undertaken study of arcjet flow dynamics both computationally and experimentally. Their work will be reviewed here briefly. Schrade et. al. [6] have modelled two-dimensional, axi-symmetric, fully ionized flow in an MPD arcjet. While this has relevance to the hybrid (electromagnetic/electrothermal) device, it is not directly applicable to the arcjet which is a purely electrothermal device. The main drawback is that the detailed finite rate chemistry which is vital to arcjet performance, is not modelled. More recently, Schrade et. al.[7,8] have extended their two-fluid, quasi one-dimensional model in order to study the interaction between the flow in the hot arc and the cooler outer flow in the constrictor region of the arcjet. Their focus has been mainly to understand the arc attachments and arc dynamics in the constrictor region[9]. Butler et. al.[10], King and Butler[11], and Rhodes and Keefer[12] have also begun modelling of two-temperature axi-symmetric flows in arcjets. A common denominator however in all the aforementioned works is that the state-resolved chemistry (especially including vibrational and electronic non-equilibrium) is neglected. Additionally, many of these investigators are utilizing methods (such as SIMPLE[13], for instance) commonly avoided for viscous supersonic internal flows, on grids that are coarse (less than 50 x 50 for instance). Rhodes and Keefer even mention that when swirl is added to their model, no converged solution could be obtained[12]. Such results, although first in modelling of arcjet flows, should therefore be treated with cautious optimism.

More recently, several works[14-16] have attempted to improve the state-of-the-art in modelling of arcjet flows. However, these efforts have been plagued by problems ranging from long run times (on the order of hundreds of CPU hours on CRAY supercomputers) to ad-hoc assumptions such as the use of conductivity floors. Run times on the order of hundreds of CRAY hours hardly constitutes a useful design tool, and ad-hoc fixes such as the use of a "conductivity floor" will not be very useful in yielding predictive design tools (since adjustable constants can be made to vary to fit almost any experimental result).

In contrast, the method developed in the work reported here is found to be highly accurate

and reliable. Furthermore, our scheme is equally applicable to quasi 1-D, 2-D axi-symmetric, as well as 3-D problems including large sets of master rate equations describing rate processes. The ultimate power of this technique is evident especially when applied on modern supercomputers. The present research therefore represents a significant advance in the state-of-the-art.

3.0 RESEARCH OBJECTIVES

The objectives of this four-year research program are (1) to study and quantify detailed vibrational and electronic non-equilibrium energy transfer processes in the arcjet nozzle, (2) to quantify the ro-vibrational populations using modern information on state-resolved rate constants to enable accurate determination of frozen flow losses, and (3) numerically study the effects of dilution of the propellant feed with a fast Vibration-Translation (VT) relaxer, on recovery of frozen flow losses.

4.0 STATUS OF RESEARCH EFFORT

The discussion below summarizes the highlights of the research efforts under the first year of this grant. A more detailed discussion can be found in the appendices and references[17-19].

4.1 ACCOMPLISHMENTS OF FIRST TWO YEARS

The first two years of Grant AFOSR-91-0318 have focused on selection of a numerical scheme that (1) is appropriate for supercomputing, (2) that scales from quasi-1D through 2-D to fully 3-D problems, and (3) which can be easily extended to hundreds of states associated with the different species present in the supersonic nozzle of the hydrazine and ammonia arcjets.

Use of numerical methods for highly non-equilibrium high speed reacting *internal* flows are not by any means trivial. Although the numerical techniques of MacCormack[20-22] and Beam and Warming[23] are well developed for supersonic external compressible flows, the incorporation of finite rate kinetics and the problem of *internal* flow complicates the schemes substantially. Stringent demands must therefore be placed on computational speed, stability, and accuracy especially if a 3-D simulation is the ultimate goal. The chosen numerical scheme known as the Linearized Block Implicit (LBI) method first developed by Briley and McDonald[24] shows tremendous promise. It is the only method that is well suited to supercomputers, and extends all the way from quasi 1-D, to 2-D axi-symmetric, through to fully 3-D situations. This research effort has been divided into 2 two-year increments (overall, a four year effort), in which the first two years have been devoted to numerical models of cold flow, ionizing

flow, and vibrationally non-equilibrium flow under quasi-1D, 2-D with swirl, and fully 3-D assumptions. Each of these cases is summarized separately below, but extensive details may be found in the appendices as well as in the annual report for the first year[25].

(i) Quasi 1-D Flow:

Sample calculations of quasi 1-D flow with gas internal-mode molecular energy transfer in the 30 KW geometry of the arcjet (see Appendix A) have been performed for the case of smooth acceleration to supersonic speeds. Each of these energy transfer processes represent elementary mechanisms and could just as easily represent chemical reactions. Thus, although the arc and propellant chemistry are not modelled in this case, this calculation illustrates the power of the numerical algorithm and its ultimate usefulness for simulating real arcjet flows. In the case of the CO/N₂ mixture as many as 80 total internal vibrational states are modelled. These could easily have been as many chemical species, or represented the internal vibrational modes in a N₂/H₂ mixture.

(ii) 2-D Axi-symmetric Flow (with swirl):

Few existing works have successfully examined viscous supersonic internal flows with swirl. We have completed both cold flow and arcjet simulations (i.e. governing equations for 2-D axi-symmetric, viscous flow with swirl, combined with Maxwell's equations, and with finite rate ionization, recombination, and dissociation processes) in the 30 KW arcjet geometry. The governing equations and details of the application of the LBI method to these equations is given in the appendices. Detailed examination of the effect of swirl on cold flow in geometries of interest to the arcjet thruster reveal that the upstream plenum length, i.e. distance from the swirl injector to the beginning of the converging section, is a **critical design parameter for a given operating propellant mass flow rate**. For the case of high mass flow rates on the order of g/s, the swirl component of the absolute velocity is found to decrease in the streamwise direction so that by the time the constrictor is reached the *inlet swirl fails to persist*. On the other hand, for mass flow rates on the order of mg/s, the swirl component of the absolute velocity *increases* in the streamwise direction and reaches a maximum value in the constrictor region.

The enhancement of injected swirl may be explained as follows. Injection of swirl into the arcjet is equivalent to an influx of angular momentum in the streamwise direction. If the torque due to the shear stress at the wall is insufficient to overcome this influx of angular momentum, then the inlet swirl will persist far enough downstream so that the decreasing cross-sectional area in the converging section of the arcjet geometry will cause an increase in the swirl. Although this result is observed at

low mass flow rates (i.e. on the order of mg/s), it strongly suggests that for any given mass flow rate, there exists a maximum plenum length beyond which the injected swirl will have no effect whatsoever on the arc downstream. This is because the torque due to the wall shear stress acting on the plenum boundaries is large enough to consume the inlet flux of angular momentum.

Illustrative results for arcjet flow are shown in Figures 1 through 14. These illustrative cases are for 80 mg/s of hydrogen flow at 100 A in the 30 KW geometry. A full discussion of these and other results for argon and nitrogen propellants are discussed in a forthcoming paper[26].

(iii) Fully 3-D Simulations:

Development of a fully 3-D cold-flow code (using the LBI method) from a 2-D axisymmetric cold flow model is relatively straight forward. Although such a 3-D code has been tested, it has not been run extensively mainly in order to save computer time. We envision extensive numerical studies being conducted using our 2-D axisymmetric model, and the fully 3-D model being used for select cases once the intricate details of the arcjet flow problem have been fully explored.

The fully 3-D model is expected to be useful in situations where conditions of azimuthal symmetry break down. Such a situation can very easily occur in practice, where the centerline of the cathode and anode may not coincide due to slight misalignment during initial assembly. The resulting effects on any measurements made downstream of the cathode tip could be quite severe. This will be further explored.

4.2 ON-GOING & FUTURE WORK

Research has been initiated in four parallel areas, namely (1) incorporation of species diffusion (completed as of March 1994), (2) incorporation of vibrational and electronic non-equilibrium for diatomic species, (3) incorporation of governing equation for electron energy distribution function, and (4) modelling of anode attachment without ad-hoc fixes. Most of this will be completed in the second two years of this first 4-year effort. The second 2-year effort will involve completion of model development, extensive comparison with available experimental data, suggestions for new experiments, and detailed performance calculations for the 1 KW and 30 KW arcjets.

In comparison with our originally proposed work statement, we are exactly on schedule for completion of the proposed tasks for the second two-years of the full 4-year period. Since our approach to modelling of the arcjet flow is unique, novel, and extends the state-of-the-art, we anticipate greater interaction with experimentalists

making measurements on the 1 KW and 30 KW arcjet thrusters.

5.0 REFERENCES

- (1) H. A. Stine, and V. R. Watson, "The Theoretical Enthalpy Distribution of Air in Steady Flow along the Axis of a Direct-Current Electric Arc", NASA TN D-1331, Ames Research Center, Moffett Field, California, August 1962.
- (2) R. R. John, S. Bennett, L. A. Cass, M. M. Chen, and J. F. Connors, "Energy Addition and Loss Mechanisms in the Thermal Arc Jet Engine", paper AIAA-63-022, presented at the AIAA Electric Propulsion Conference, Colorado Springs, Colorado, March 11-13, 1963.
- (3) L. E. Wallner, and J. Czika, "Arc-Jet Thrustor for Space Propulsion", NASA TN D-2868, Washington, D.C., June 1965.
- (4) V. R. Watson, and E. B. Pegot, "Numerical Calculations for the Characteristics of a Gas Flowing Axially Through a Constricted Arc", NASA TN D-4042, Ames Research Center, Moffett Field, California, June 1967.
- (5) R. J. Cassady, P. G. Lichon, and D. Q. King, "Arcjet Endurance Test Program", Final Report AL-TR-90-069, prepared for the Phillips Laboratory, Air Force Systems Command, Edwards AFB, CA 93523-5000, March 1991.
- (6) B. Glocker, H. O. Schrade, and P. C. Sleziona, "Numerical Prediction of Arcjet Performance", paper AIAA-90-2612, presented at the 21st International Electric Propulsion Conference, July 18-20, 1990, Orlando, Florida.
- (7) M. Auweter Kurtz, H. L. Kurtz, H. O. Schrade, and P. C. Sleziona, "Numerical Modelling of the Flow Discharge in MPD Thrusters", *J. Propulsion & Power*, Vol. 5, No. 1, Jan.-Feb. 1989.
- (8) H. O. Schrade, and P. C. Sleziona, "Basic Processes of Plasma Propulsion", Interim Scientific Report, AFOSR-86-0337, July 1989.
- (9) H. O. Schrade, Private Communication, May 8, 1990.

- (10) G. W. Butler, B. A. Kashiwa, and D. Q. King, "Numerical Modelling of Arcjet Performance", paper AIAA-90-1474, presented at the 21st International Electric Propulsion Conference, July 18-20, 1990, Orlando, Florida.
- (11) D. Q. King and G. W. Butler, "Modelling and Measurement of N2 Arcjet Performance", paper AIAA-90-2616, presented at the 21st International Electric Propulsion Conference, July 18-20, 1990, Orlando, Florida.
- (12) R. P. Rhodes, and D. Keefer, "Numerical Modelling of an Arcjet Thruster", paper AIAA-90-2614, presented at the 21st International Electric Propulsion Conference, July 18-20, 1990, Orlando, Florida.
- (13) S. V. Patankar, *Numerical Heat Transfer and Fluid Flow*, Hemisphere Publishing Corp., McGraw-Hill, New York, 1980.
- (14) R. Rhodes, and D. Keefer, "Comparison of Model Calculations with Experimental Data from Hydrogen Arcjets", paper IEPC-91-111 presented at the 22nd AIDAA/AIAA/DGLR/JSASS International Electric Propulsion Conference, Viareggio, Italy, October 14-17, 1991.
- (15) G. W. Butler, and D. Q. King, "Single and Two Fluid Simulations of Arcjet Performance", paper AIAA-92-3104 presented at the 28th AIAA/SAE/ASME/ASEE Joint Propulsion Conference, Nashville, Tennessee, July 6-8, 1992.
- (16) S. A. Miller, and M. Martinez-Sanchez, "Multifluid Nonequilibrium Simulation of Electrothermal Arcjets", paper AIAA-93-2101 presented at the 29th AIAA/SAE/ASME/ASEE Joint Propulsion Conference, Monterey, California, June 28-30, 1993.
- (17) A. Chiroux de Gavelle de Roany, C. Flament, J. W. Rich, V. V. Subramaniam, and W. R. Warren, "Stron Vibrational Nonequilibrium in Supersonic Nozzle Flows", AIAA J., in press.
- (18) V. Babu, S. Aithal, and V. V. Subramaniam, "Vibrational Non-Equilibrium in Arcjet Flows", paper IEPC-93-129 presented at the 23rd International Electric Propulsion Conference, Seattle, Washington, September 13-17, 1993.
- (19) V. Babu, S. Aithal, and V. V. Subramaniam, "On the Effects of Swirl in Arcjet Thruster

Flows", paper IEPC-93-183 presented at the 23rd International Electric Propulsion Conference, Seattle, Washington, September 13-17, 1993.

- (20) R. W. MacCormack, "The Effect of Viscosity in Hypervelocity Impact Cratering", paper AIAA-69-354, presented at the AIAA Hypervelocity Impact Conference, April 30-May 2, 1969, Cincinnati, Ohio.
- (21) R. W. MacCormack, "A Numerical Method for Solving the Equations of Compressible Viscous Flow", paper AIAA-81-0110, presented at the AIAA 19th Aerospace Sciences Meeting, January 12-15, 1981, St. Louis, Missouri.
- (22) R. W. MacCormack, Lecture Notes on "Numerical Methods for Compressible Viscous Flow", presented during a short course on Advances in Computational Fluid Dynamics, December 6-10, 1982, The University of Tennessee Space Institute, Tullahoma, Tennessee.
- (23) R. M. Beam, and R. F. Warming, "An Implicit Factored Scheme for the Compressible Navier-Stokes Equations II: The Numerical ODE Connection", paper AIAA-79-1446, presented at the AIAA 4th Computational Fluid Dynamics Conference, July 23-24, 1979, Williamsburg, Virginia.
- (24) W. R. Briley, and H. McDonald, *J. Computational Physics* 24, pp. 372-397, 1977.
- (25) V. V. Subramaniam, "Recovery of Frozen Flow Losses in Arcjets", Annual Technical Report, Grant No. AFOSR-91-0318, October 1992.
- (26) V. Babu, S. Aithal, and V. V. Subramaniam, "Propellant Internal Mode Disequilibrium in Arcjet Flows", paper AIAA-94-2655 to be presented at the AIAA Fluid Dynamics, Thermophysics, Heat Transfer, Plasmadynamics & Lasers Conference, Colorado Springs, Colorado, June 20-23, 1994.

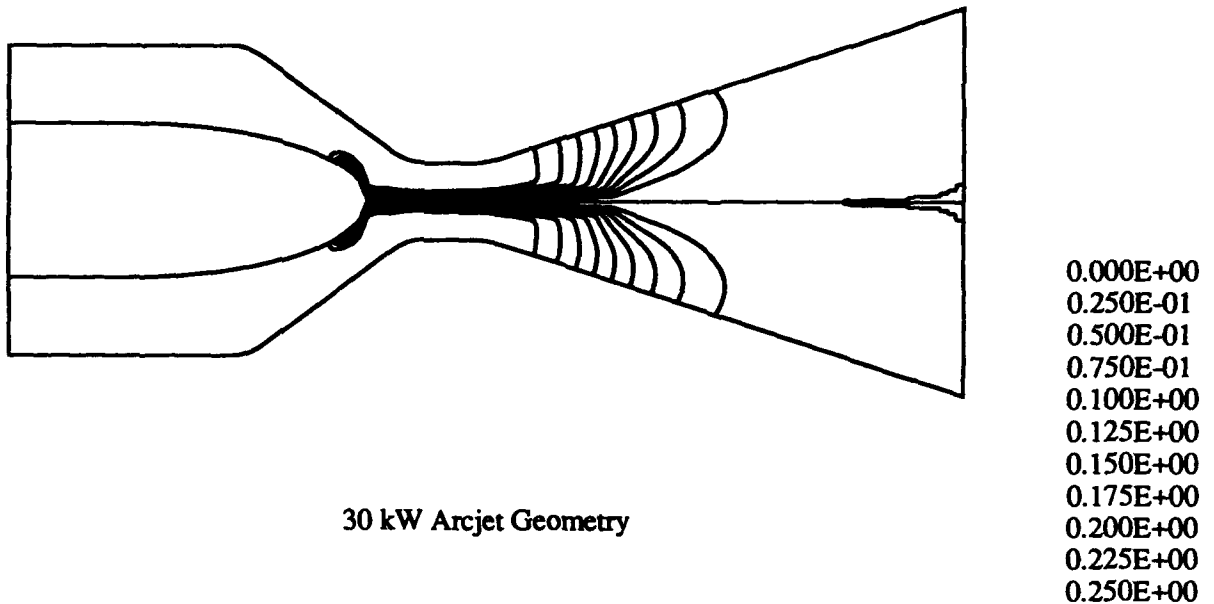
6.0 PERSONNEL

V. V. Subramaniam, Principal Investigator
V. Babu, Post-Doctoral Research Associate
S. Aithal, Graduate Student

7.0 INTERACTIONS

- (1) Dr. Siegfried Jannsen, The Aerospace Corporation.
- (2) Prof. W. R. Briley, Mississippi State University.
- (3) Prof. Dennis Keefer, University of Tennessee.
- (4) Dr. Frank Curran, NASA Lewis Research Center.

Current Contours



30 kW Arcjet Geometry

Fig. 1: Contours of ψ ($= rB$) or enclosed current contours are shown here for the hydrogen arcjet at 100 A and a mass flow rate of 100 mg/s in the 30 KW geometry. Details of the calculation are given in the appendices as well as in a forthcoming paper[26].

Temperature

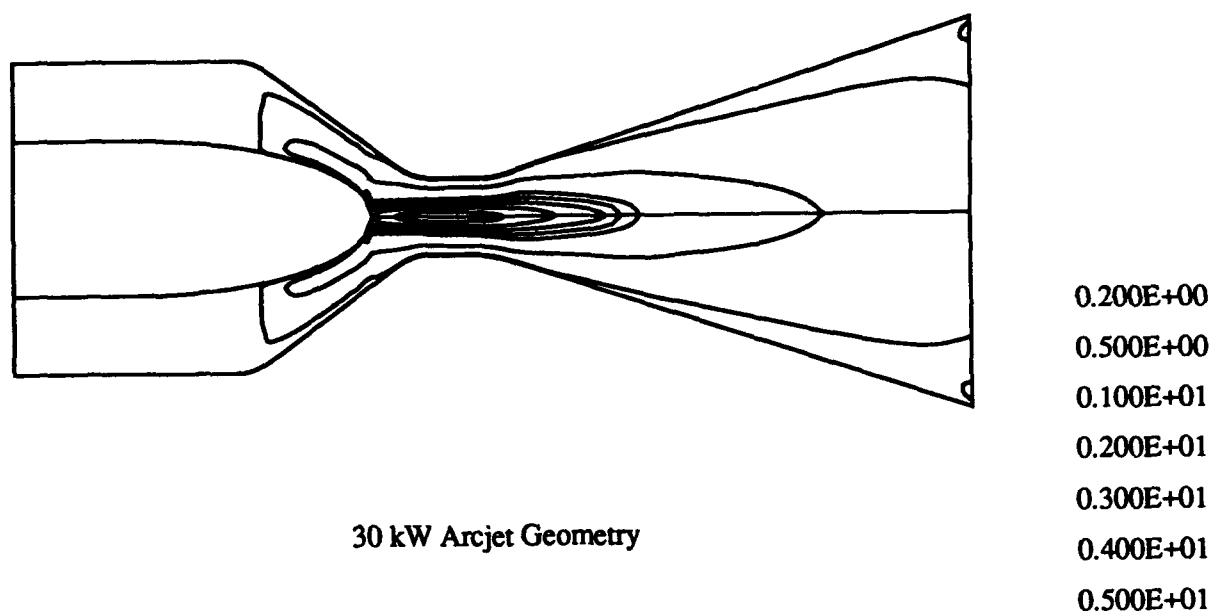
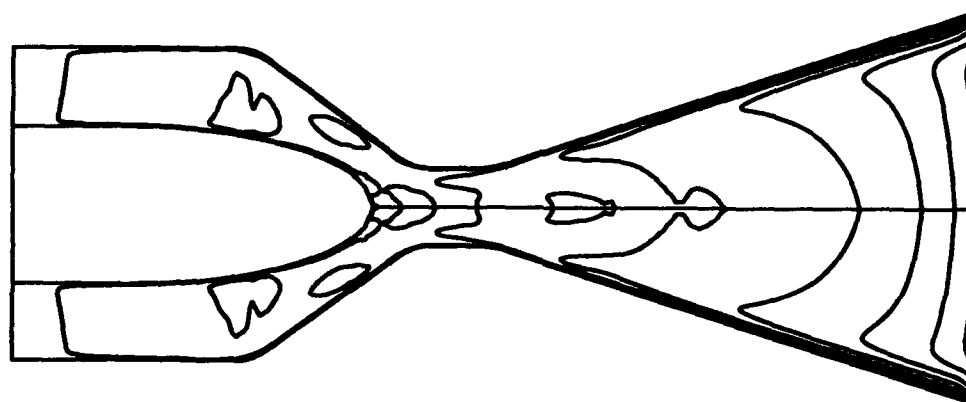


Fig. 2: Contours of temperature (non-dimensionalized by 10,000 K) are shown here for the one-temperature model. The inner-most contour represents 50,000 K, while the outer-most represents 2,000 K.

Mach Number

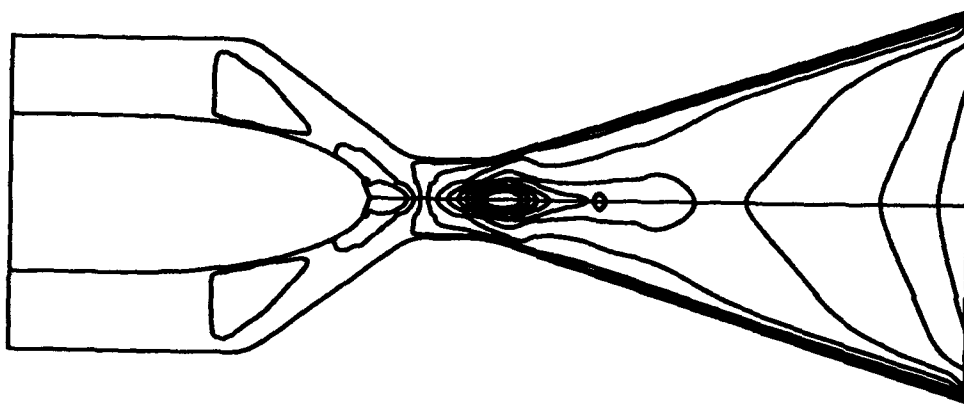


30 kW Arcjet Geometry

0.100E+00
0.300E+00
0.500E+00
0.700E+00
0.900E+00
0.110E+01
0.130E+01

Fig. 3: Contours of the Mach number (Flow velocity divided by the frozen speed of sound) are shown here. $M=1.3$ is the right-most contour.

Axial Velocity



30 kW Arcjet Geometry

-0.100E+00
0.000E+00
0.100E+00
0.200E+00
0.300E+00
0.400E+00
0.500E+00
0.600E+00
0.700E+00
0.800E+00
0.900E+00

Fig. 4: Contours of axial component of velocity (non-dimensionalized by 8,323.6 m/s) are shown here. Note the pockets of recirculating flow at the cathode tip as represented by negative axial velocity contours. These pockets have recently been observed experimentally by Cappelli at Stanford.

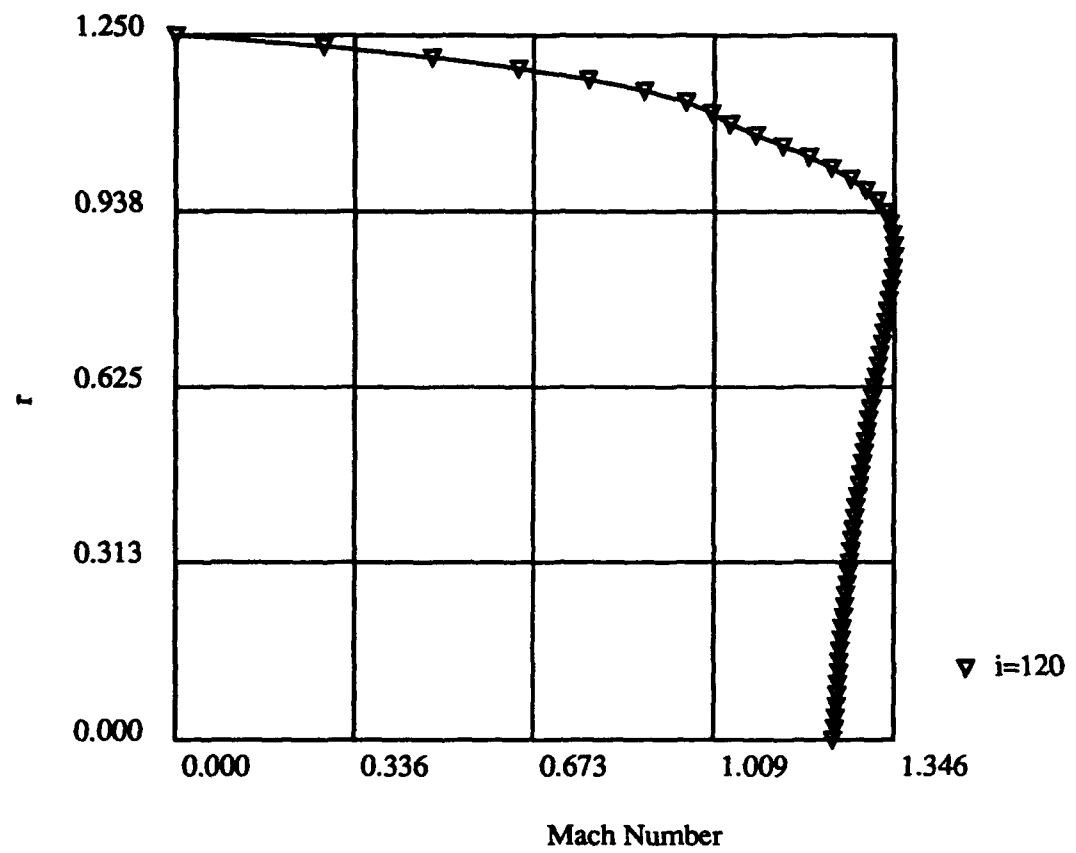


Fig. 5: The Mach number based on the frozen speed of sound is shown here versus radius (non-dimensionalized by 0.01 m) at the exit plane.

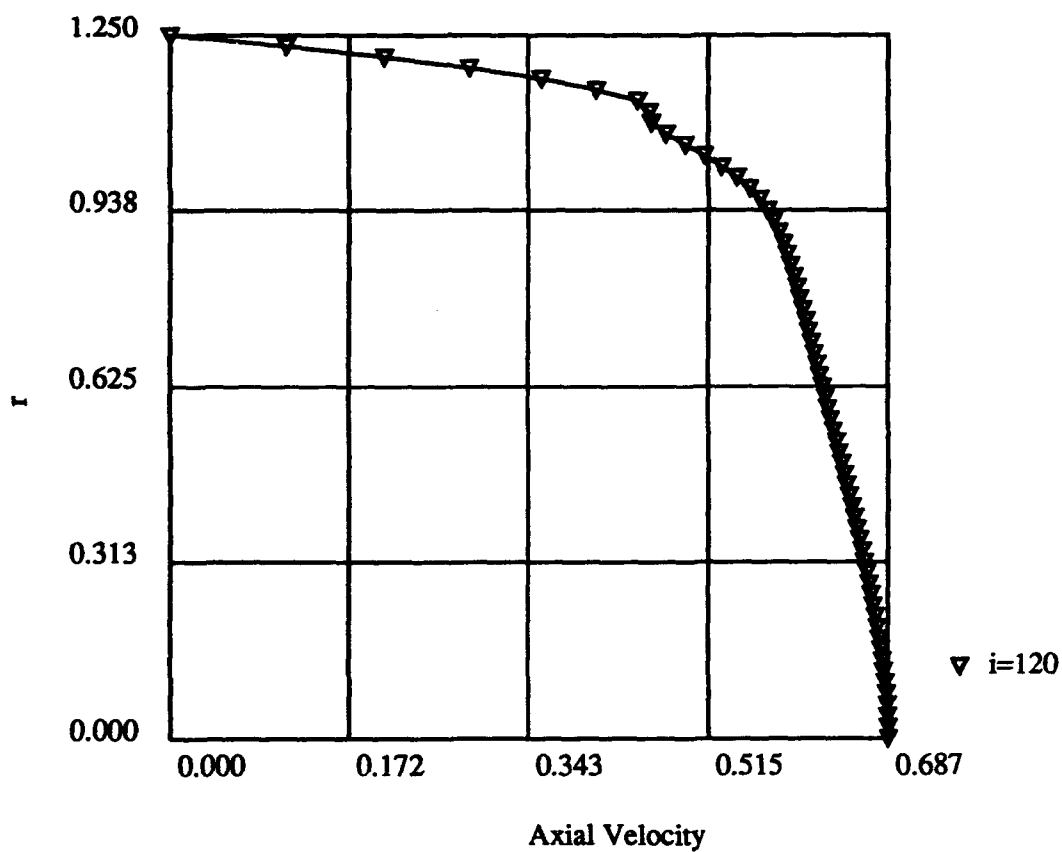


Fig. 6: The axial velocity (non-dimensionalized by 8323.6 m/s) is shown here versus radius (non-dimensionalized by 0.01 m) is shown here at the exit plane.

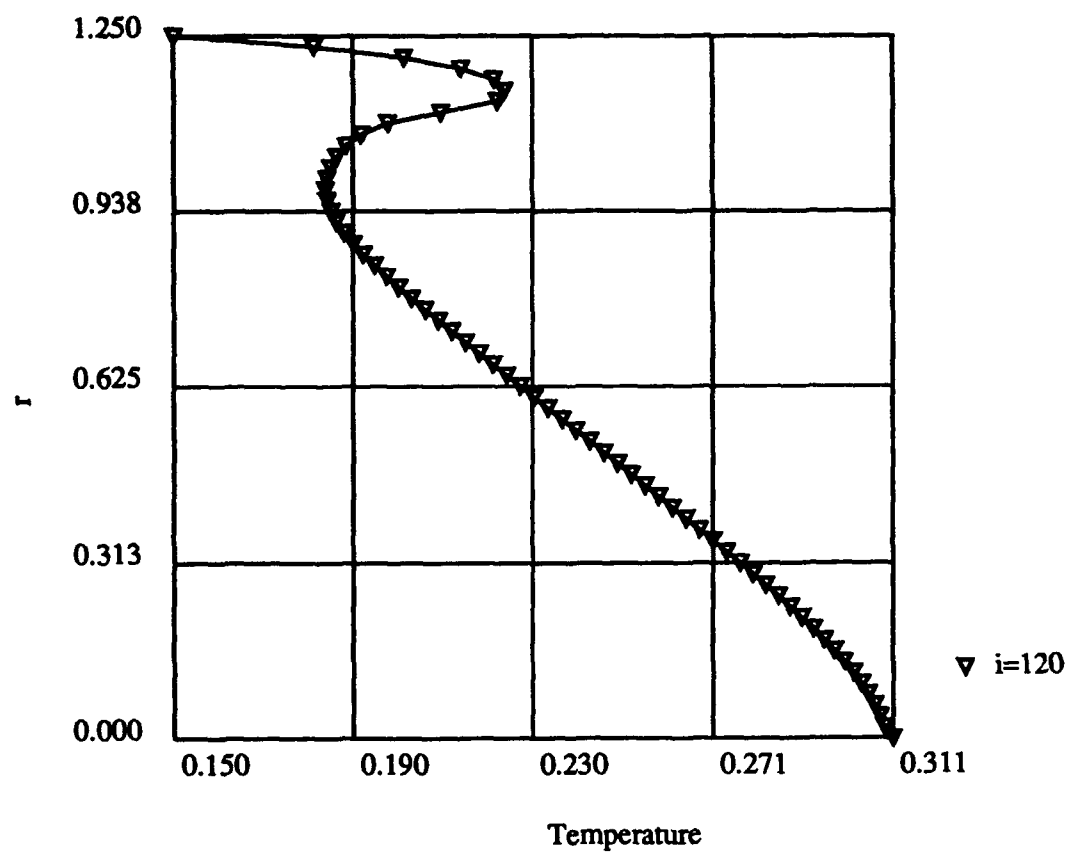


Fig. 7: The temperature (non-dimensionalized by 10,000 K) is shown here versus radius (non-dimensionalized by 0.01 m) is shown here at the exit plane.

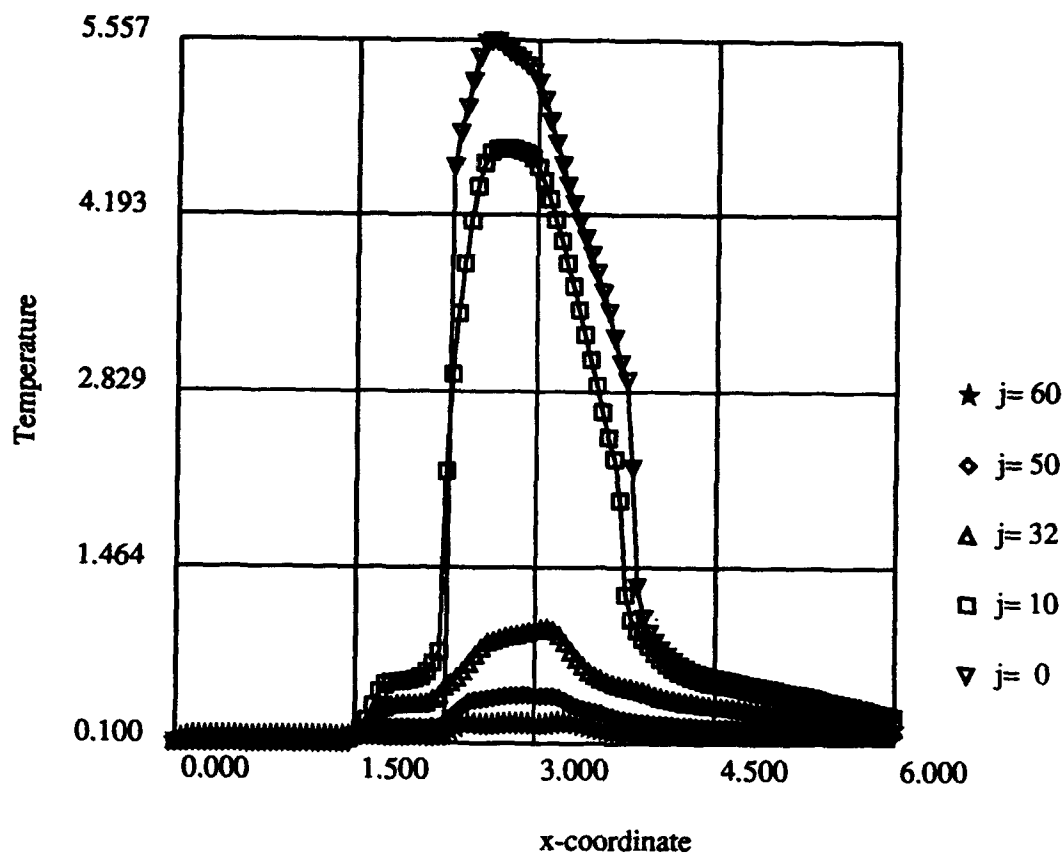


Fig. 8: Profiles of temperature (non-dimensionalized by 10,000 K) are shown here versus x (non-dimensionalized by 0.01 m) at various radial locations. $j=0$ corresponds to the cathode surface and channel centerline, while $j=60$ corresponds to locations near the anode.

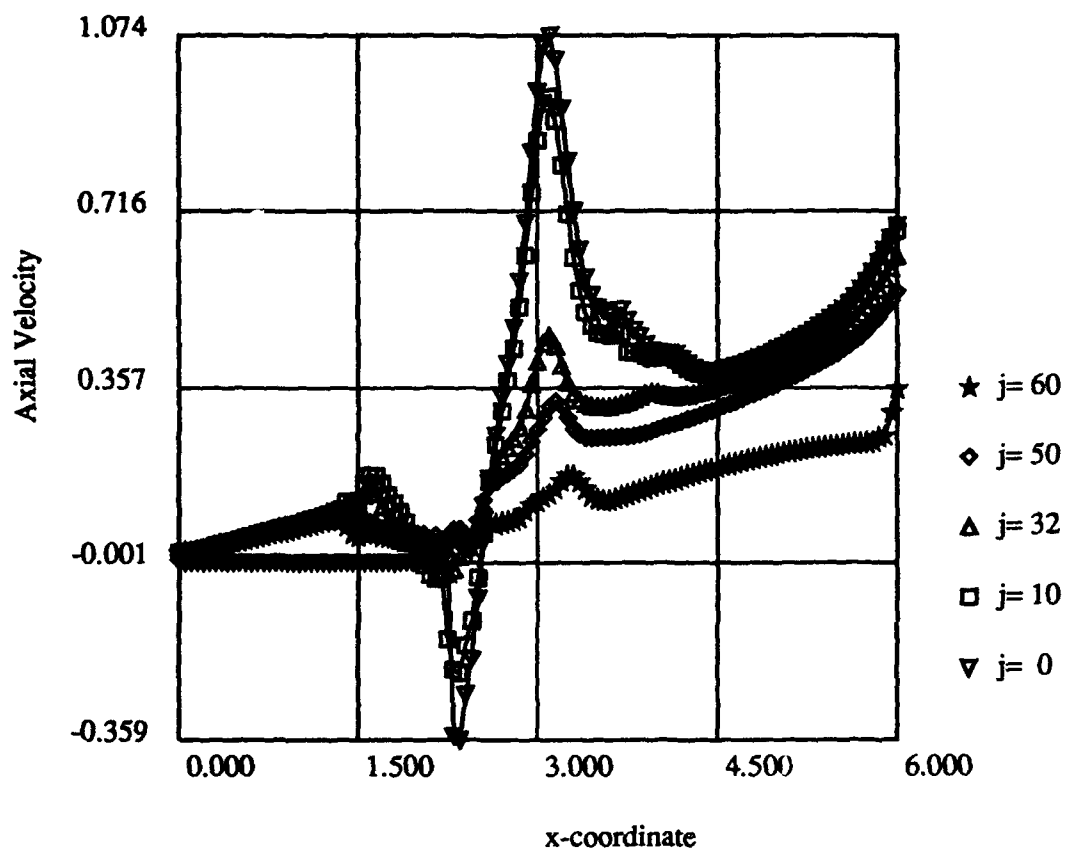


Fig. 9: Profiles of axial component of velocity (non-dimensionalized by 8323.6 m/s) are shown here versus x (non-dimensionalized by 0.01 m) at various radial locations. $j=0$ corresponds to the cathode surface and channel centerline, while $j=60$ corresponds to locations near the anode. Note the presence of the recirculation zones or separation bubbles at the cathode tip.

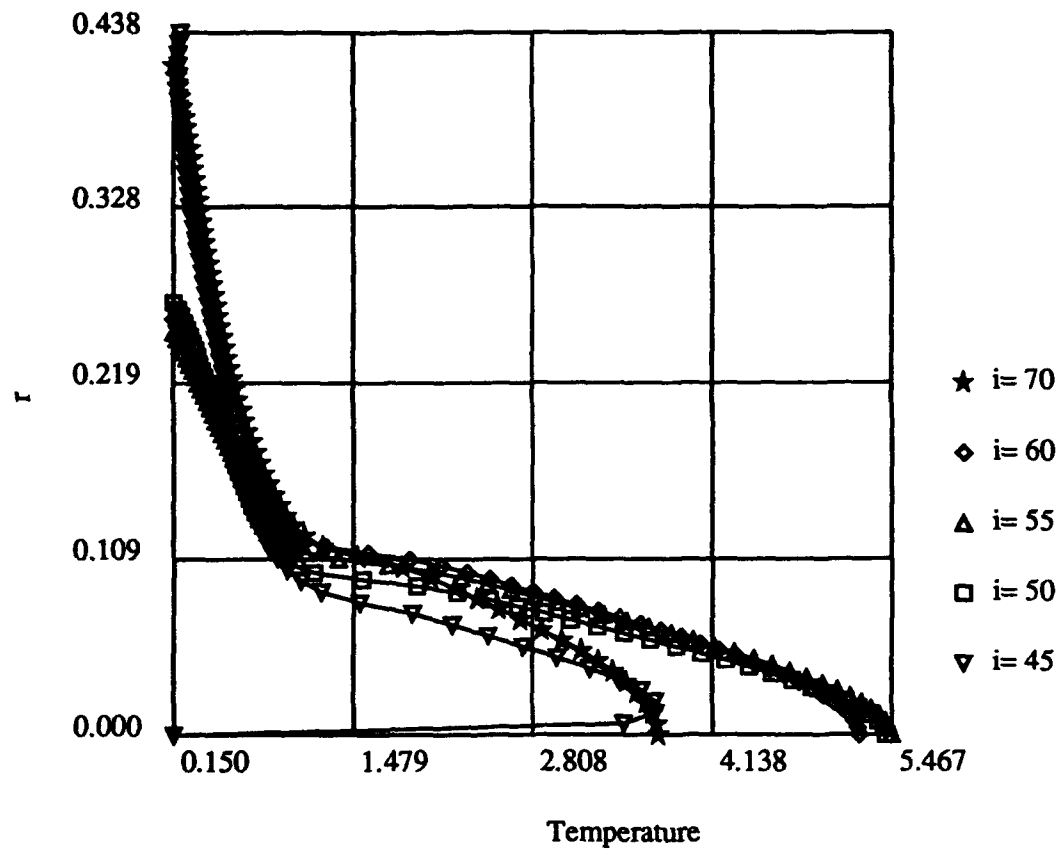


Fig. 10: Profiles of temperature (non-dimensionalized by 10,000 K) are shown here versus r (non-dimensionalized by 0.01 m) at various axial locations. $i=45$ corresponds to locations near the cathode tip, while $i=70$ corresponds to locations after the constrictor and in the nozzle. $i=50$, $i=55$, and $i=60$ all represent locations near the constrictor inlet, constrictor center, and constrictor exit respectively.

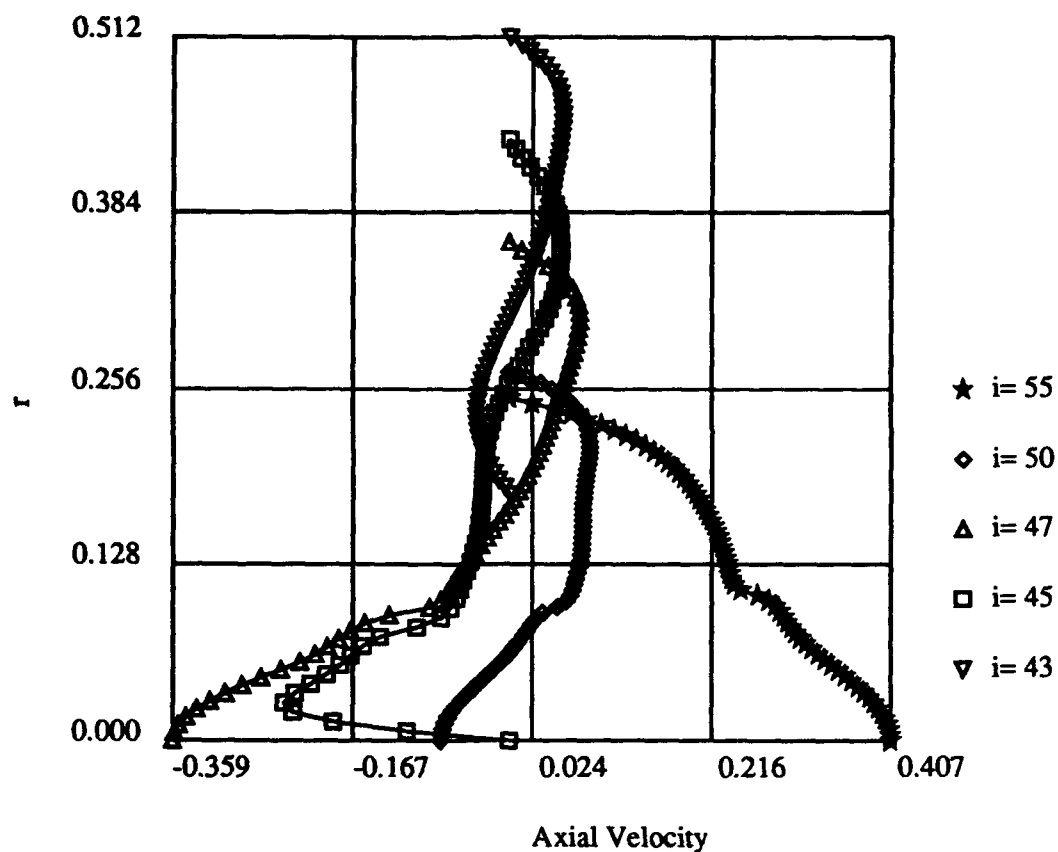


Fig. 11: Profiles of axial component of velocity (non-dimensionalized by 8323.6 m/s) are shown here versus r (non-dimensionalized by 0.01 m) at various axial locations. $i=45$ corresponds to locations near the cathode tip, while $i=70$ corresponds to locations after the constrictor and in the nozzle. $i=50$, $i=55$, and $i=60$ all represent locations near the constrictor inlet, constrictor center, and constrictor exit respectively.

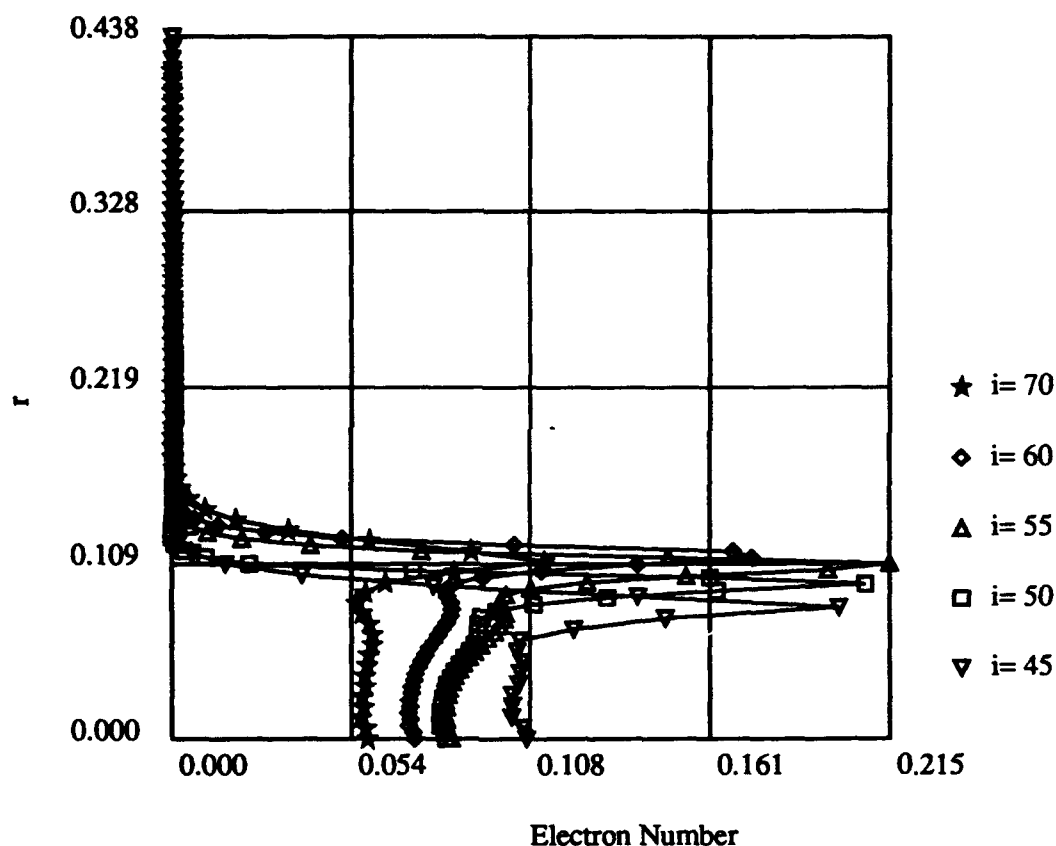


Fig. 12: Profiles of electron number density (non-dimensionalized by $5.8 \times 10^{22} \text{ m}^{-3}$) are shown here versus r (non-dimensionalized by 0.01 m) at various axial locations. $i=45$ corresponds to locations near the cathode tip, while $i=70$ corresponds to locations after the constrictor and in the nozzle. $i=50$, $i=55$, and $i=60$ all represent locations near the constrictor inlet, constrictor center, and constrictor exit respectively. Note the sharp gradients in the profiles which clearly define the arc boundary in the absence of diffusion. The electron number density is seen to increase with radius and then abruptly decrease outside the arc boundary. Such maxima are typical when there are opposing mechanisms, i.e ohmic heating tending to increase ionization while the temperature decreasing with radius tends to decrease the ionization.

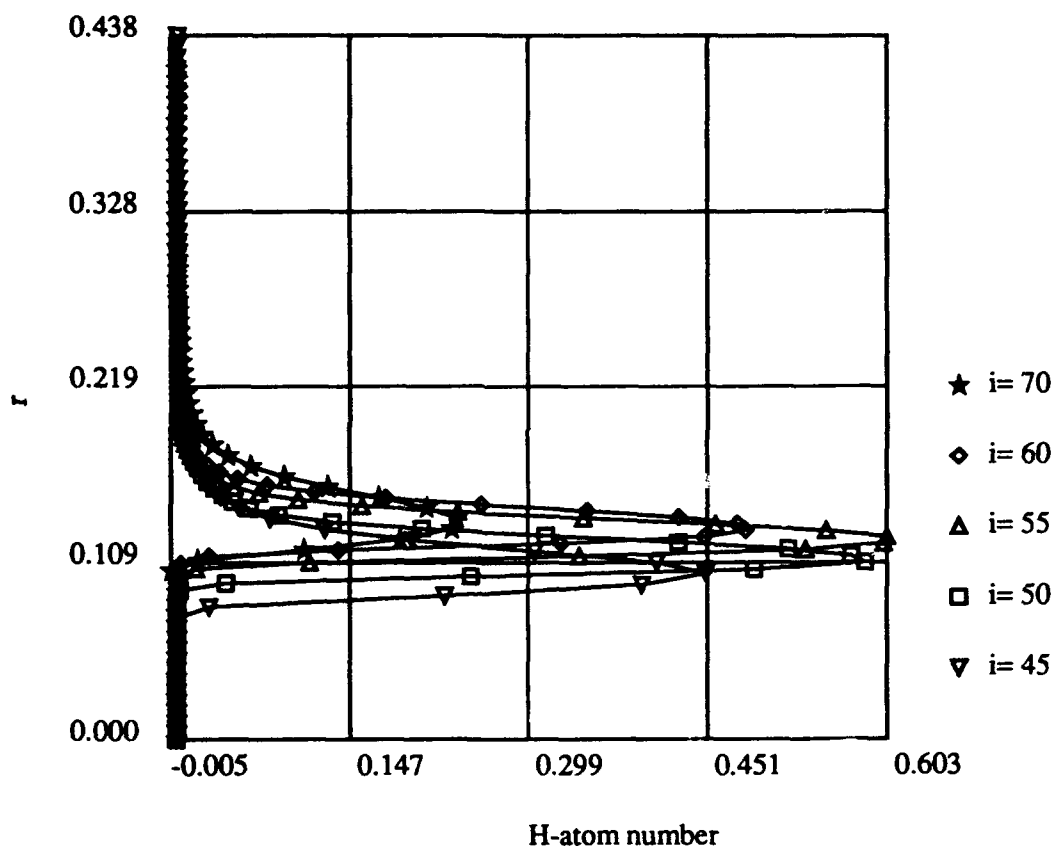


Fig. 13: Profiles of atomic hydrogen number density (non-dimensionalized by $5.8 \times 10^{22} \text{ m}^{-3}$) are shown here versus r (non-dimensionalized by 0.01 m) at various axial locations. $i=45$ corresponds to locations near the cathode tip, while $i=70$ corresponds to locations after the constrictor and in the nozzle. $i=50$, $i=55$, and $i=60$ all represent locations near the constrictor inlet, constrictor center, and constrictor exit respectively. Note that here in the absence of diffusion, the atomic hydrogen concentration has a maxima in the same location as the electron number density.

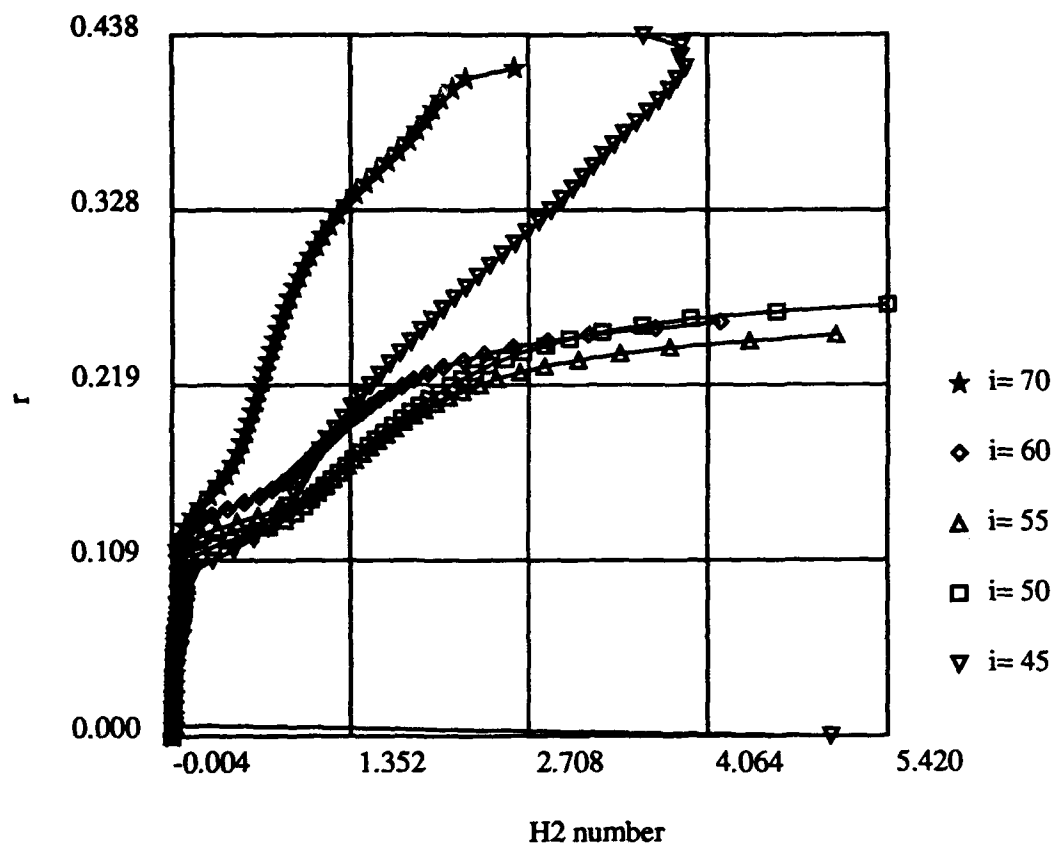


Fig. 14: Profiles of molecular hydrogen number density (non-dimensionalized by $5.8 \times 10^{22} \text{ m}^{-3}$) are shown here versus r (non-dimensionalized by 0.01 m) at various axial locations. $i=45$ corresponds to locations near the cathode tip, while $i=70$ corresponds to locations after the constrictor and in the nozzle. $i=50$, $i=55$, and $i=60$ all represent locations near the constrictor inlet, constrictor center, and constrictor exit respectively. Note that the molecular hydrogen concentration is largest near the anode, where both electron and atomic hydrogen concentrations are smaller.

APPENDIX A

Numerical Solutions of Viscous, Internal, Supersonic Flows

V. Babu & V. V. Subramaniam

Department of Mechanical Engineering
The Ohio State University
Columbus, OH 43210.

1 Introduction

The compressible Navier-Stokes equations govern the physics of flow fields in many applications. Recently, many aerospace applications involving both internal and external supersonic flows have arisen. These flows are often times further complicated by the effects of departure from thermodynamic equilibrium of the internal modes of molecular motion. This disequilibrium between internal modes (vibration, rotation and electronic excitation) and external modes i.e. translational molecular motions gives rise to complicated chemistry. Before such complex flows can be studied however, the basic supersonic viscous flow equations must be solved using a reliable numerical method that can be readily extended to multi-dimensions. This is the focus of the present article.

Many numerical methods have been devised to solve the compressible, Navier-Stokes equations, the most popular of these being the MacCormack scheme [1], the Beam-Warming scheme [2] and the linearized block implicit (LBI) scheme of Briley & McDonald [3]. There are many solutions for viscous, external, supersonic flows obtained with any of these methods (see for example [4, 5]), and there are a few recent works that include simple chemical kinetics [6, 7]. In contrast, there are only a limited number of available numerical solutions for internal, viscous supersonic flows [8]. Further, there has been only one recent work that investigates the effects of non-equilibrium state resolved chemistry and vibrational non-equilibrium in a supersonic expansion in a converging-diverging (C-D) nozzle [9]. This work however examines the flow under the quasi one-dimensional assumption. Our ultimate goal is to obtain two- and three-dimensional solutions that include such state resolved kinetics.

In this paper, numerical solutions to viscous subsonic and supersonic flows in C-D nozzles are presented both with and without the effects of swirl. The area ratios of the nozzles that we consider are high, being of the order of 25 and can be even higher. The LBI scheme of Briley & McDonald [3] is used to obtain these solutions. The importance of studying such flows in this geometry cannot be emphasized enough, for, the essential physics of internal, supersonic flows in many problems of practical interest can be related to the flow in a corresponding C-D nozzle geometry. With this in mind, we present both inviscid quasi one-dimensional solutions and two-dimensional axisymmetric, viscous flow solutions. We find that the key to obtaining these solutions is the proper modelling of the exit boundary conditions and specification of the

proper initial conditions so that the flow can accelerate smoothly from subsonic to supersonic speeds. The algorithm itself is easily extendable to three dimensions.

This paper is organized as follows. The governing equations and boundary conditions are presented first, followed by the numerical method. Quasi 1-D and 2-D axisymmetric solutions with and without swirl are discussed next, followed by a summary and conclusions of this work.

2 Formulation

The equations that govern the cold (i.e. non-reacting) viscous, supersonic flow are the compressible Navier-Stokes equations. For our present purposes, we consider them in cylindrical polar coordinates in 2-D axisymmetric form. These equations are made dimensionless by non-dimensionalizing coordinates by the throat radius, density by the inlet stagnation density, temperature by the inlet stagnation temperature, and velocities by the inlet stagnation speed of sound respectively. Pressure is eliminated from the system of equations by using the equation of state. This choice of non-dimensionalization differs from the conventional ones [5, section 5-1.6] but is closely related to the one used in [3]. Since in general in a reacting flow the properties such as specific heats and viscosity are locally varying (and in most instances by as much as orders of magnitude), non-dimensionalization using quantities such as local frozen speed of sound [10], pressure etc., are not useful. We choose therefore as reference quantities, stagnation conditions upstream at the inlet and as will be seen later, two of these quantities, namely, stagnation pressure and stagnation temperature have to be prescribed at the inlet as boundary conditions. Accordingly, we have in conservative, non-dimensional form:

$$\frac{\partial \rho}{\partial t} + \frac{1}{r} \frac{\partial(r\rho u)}{\partial r} + \frac{\partial(\rho w)}{\partial z} = 0, \quad (1)$$

$$\begin{aligned} \frac{\partial(\rho u)}{\partial t} + \frac{1}{r} \frac{\partial(r\rho u^2)}{\partial r} + \frac{\partial(\rho uw)}{\partial z} - \frac{\rho v^2}{r} = & -\frac{1}{\gamma} \frac{\partial(\rho T)}{\partial r} \\ & + \frac{1}{Re} \left(\nabla^2 u - \frac{u}{r^2} \right) + \frac{1}{3} \frac{1}{Re} \frac{\partial}{\partial r} (\nabla \cdot \vec{u}), \end{aligned} \quad (2)$$

$$\frac{\partial(\rho v)}{\partial t} + \frac{1}{r} \frac{\partial(r\rho uv)}{\partial r} + \frac{\partial(\rho vw)}{\partial z} + \frac{\rho uv}{r} = \frac{1}{Re} \left(\nabla^2 v - \frac{v}{r^2} \right), \quad (3)$$

$$\frac{\partial(\rho w)}{\partial t} + \frac{1}{r} \frac{\partial(r\rho uw)}{\partial r} + \frac{\partial(\rho w^2)}{\partial z} = -\frac{1}{\gamma} \frac{\partial(\rho T)}{\partial z} + \frac{1}{Re} \nabla^2 w + \frac{1}{3} \frac{1}{Re} \frac{\partial}{\partial z} (\nabla \cdot \vec{u}), \quad (4)$$

$$\begin{aligned} \frac{\partial(\rho T)}{\partial t} + \frac{1}{r} \frac{\partial(r\rho uT)}{\partial r} + \frac{\partial(\rho wT)}{\partial z} + (\gamma - 1)\rho T(\nabla \cdot \vec{u}) \\ = \frac{\gamma}{RePr} \nabla^2 T + \frac{\gamma(\gamma - 1)}{Re} \Phi, \end{aligned} \quad (5)$$

where, Φ is the dissipation function given by,

$$\Phi = 2 \left[\left(\frac{\partial u}{\partial r} \right)^2 + \left(\frac{u}{r} \right)^2 + \left(\frac{\partial w}{\partial z} \right)^2 \right] + \left(\frac{\partial v}{\partial z} \right)^2 + \left(\frac{\partial u}{\partial z} + \frac{\partial w}{\partial r} \right)^2 + \left(\frac{\partial v}{\partial r} - \frac{v}{r} \right)^2 - \frac{2}{3} \left(\frac{\partial u}{\partial r} + \frac{u}{r} + \frac{\partial w}{\partial z} \right)^2,$$

and

$$\nabla \cdot \vec{A} = \frac{e_r}{r} \frac{\partial}{\partial r} (r A_r) + e_z \frac{\partial A_z}{\partial z}, \quad \nabla^2 \phi = \frac{\partial^2 \phi}{\partial r^2} + \frac{1}{r} \frac{\partial \phi}{\partial r} + \frac{\partial^2 \phi}{\partial z^2},$$

where, $\vec{A} = A_r e_r + A_\theta e_\theta + A_z e_z$ is any vector and ϕ is a scalar.

In the above equations, $\vec{u} = u e_r + v e_\theta + w e_z$ is the velocity vector, $\gamma = C_p/C_v$ is the ratio of specific heats, $Re = \rho_o a_o r_{throat} / \mu$ is the Reynolds number, and $Pr = \mu C_p / k$ is the Prandtl number. The subscript o denotes stagnation conditions at the inlet and $a_o = \sqrt{\gamma R T_o}$ is the stagnation speed of sound at the inlet. It is assumed throughout in this paper that the coefficient of viscosity μ , the thermal conductivity k of the fluid, together with other properties such as γ remain constant at representative values. Variable properties can be easily handled by the LBI scheme [3].

2.1 Boundary Conditions

Boundary conditions for the five dependent variables (ρ, u, v, w, T) need to be specified along the inlet and exit boundaries, on the wall, and along the centerline of the nozzle geometry. No-slip conditions are imposed on the wall which is maintained at a constant temperature. The density at the walls can be specified either by applying the unsteady continuity equation [3] or the normal component of the momentum equation on the wall. We choose the latter, since it is physically more meaningful to cast the boundary conditions in terms of momentum flux, but apply the radial component of the momentum equation instead of the normal component on the wall. The choice of the radial component instead of the normal component is dictated by the need for simplicity. Thus we have,

$$u = v = w = 0, \quad T = T_{surface}, \quad @ r = R(z), \quad (6)$$

$$\frac{\partial p}{\partial r} = \frac{1}{Re} \left(\frac{\partial^2 u}{\partial r^2} + \frac{1}{r} \frac{\partial u}{\partial r} \right), \quad @ r = R(z), \quad (7)$$

where $r = R(z)$ is the equation for the outer wall of the nozzle.

Symmetry conditions are imposed along the centerline for all the variables except the swirl component of velocity v , which is set equal to zero, identically. These are written as,

$$\frac{\partial \rho}{\partial r} = \frac{\partial u}{\partial r} = \frac{\partial w}{\partial r} = \frac{\partial T}{\partial r} = 0, \quad v = 0, \quad @ r = 0. \quad (8)$$

Prescribing boundary conditions at the inlet and exit planes of the nozzle depends on whether the flow is subsonic or supersonic. All the solutions presented here consider subsonic inlets. Hence, following Briley & McDonald [3], the stagnation temperature and stagnation pressure at the inlet are specified. In addition, at the inlet, the radial component of velocity is set to zero and the swirl component of velocity is either zero or set to some prescribed distribution corresponding to injection. It is important to note here that the axial component of velocity which determines the mass flow rate through the nozzle, is not specified at the inlet but is determined from an extrapolation of the interior values (see the difference equation (11) below). The above conditions can be written in dimensionless form as,

$$u = 0, \quad v = V(r), \quad @ \quad z = 0, \quad (9)$$

$$T + \frac{\gamma-1}{2}(v^2 + w^2) = 1, \quad \frac{\rho}{T^{\frac{1}{\gamma-1}}} = 1, \quad @ \quad z = 0. \quad (10)$$

Along the exit plane, the flow is entirely subsonic in the case of converging nozzles or mixed subsonic-supersonic in the case of the C-D nozzles. In either case, all the variables except density on the exit plane are evaluated by extrapolation from the interior [3]. If the local Mach number M defined as w/\sqrt{T} is greater than one at a point on the exit plane, then the density is also evaluated by extrapolation. If, on the other hand, $M < 1$ at some point on the exit plane, then the exit static pressure is specified and the density is evaluated from the equation of state. In the case of C-D nozzles, the subsonic flow occurs within the boundary layer near the wall, and the correct value of the exit static pressure would usually not be known, unless the plume is modelled as well. Care must be exercised in choosing a value for the exit static pressure, for, if it is too high, the boundary layer on the wall in the diverging section of the nozzle can separate. This is an important detail that often escapes mention in the literature.

3 Numerical Method

As a first step towards solving equations (1)-(5), a non-staggered (non-uniform or uniform) grid is generated in the physical domain. The non-uniform grids are generated using the Roberts transformation [5, section 5-6.1]. This grid in the physical domain is then transformed into a uniform grid in a computational domain using an analytical coordinate transformation. The transformation is such that the nozzle contour is transformed into a rectangle in the computational domain [5, section 5-6.1]. This transformation can be conveniently written as follows [12]:

$$r = \frac{R}{2} + \frac{R}{2}\beta \tanh \left[(\xi - 1/2) \ln \left(\frac{\beta + 1}{\beta - 1} \right) \right] \quad 0 \leq r \leq R, \quad 0 \leq \xi \leq 1, \\ \zeta = z,$$

where, ξ is the radial coordinate and ζ is the axial coordinate in the computational domain. The quantity β is a stretching parameter. It is set equal to 1.5 for generating the non-uniform grid mentioned later in Section 4. In the limit as $\beta \rightarrow \infty$ the above transformation yields a uniform grid in the radial direction also. Equations (1)-(5) together with the boundary conditions (6)-(11) are then transformed to the computational domain and solved.

The transformed forms of these equations are solved using the LBI scheme of Briley & McDonald [11]. Since all the details of the scheme have already been reported elsewhere [11, 3], only the salient features will be discussed here. First, the equations are discretized in time using Crank-Nicolson differencing. Even though this scheme is second order accurate, the linearization of the non-linear time derivatives is only first order accurate, so that the algorithm overall is only first order accurate in time. This is not a major concern if only steady state solutions are desired, as is the case here. The non-linear spatial derivatives, however, are linearized to second order accuracy in time. These and the other spatial derivatives of the dependent variables are then discretized using second order accurate central differences. The transformation derivatives are evaluated analytically. The boundary conditions also involve non-linear quantities and are linearized to second order time accuracy in the same manner as the governing equations. All the spatial derivatives that appear in these boundary conditions are evaluated using second order accurate one-sided differences. The extrapolation that is required in the inlet and exit boundaries can be done implicitly in a manner suggested by Briley & McDonald [3]. This can be written in difference form at the inlet, for example, as,

$$\psi_{0,j}^{n+1} = 2\psi_{1,j}^{n+1} - \psi_{2,j}^{n+1} \quad 1 \leq j \leq M, \quad (11)$$

where, ψ is any variable that needs to be extrapolated. The superscript $n+1$ denotes the new time level and the subscripts denote the grid indices in the usual sense. Similar expressions are written for the exit plane.

The resulting coupled, linear algebraic equations are then solved by using the Douglas-Gunn ADI method. If this system of equations were written in matrix form, then solution by the ADI method can be viewed as computing the inverse of the matrix to within a certain splitting error which is of the same order (or higher) as the time discretization error in the original equations [11]. The ADI method itself involves the solution of block tridiagonal systems in each coordinate direction, with block size equal to the number of dependent variables, which, in our case is five. These systems can be solved using existing efficient LU decomposition methods [3].

3.1 Artificial Dissipation

It is well known that artificial dissipation of some form is necessary [4, section 18.5] in order to avoid spurious oscillations (and possible loss of convergence) especially at high Reynolds numbers. This difficulty arises due to the central differencing [13, section III-C-8] used for discretizing the convective terms in equations (1)-(5). Roache [13] shows that numerical solutions exhibit non-physical behavior if the cell Reynolds number $Re_{\Delta z} = |w| \Delta z / \nu$ is greater than two. This numerical instability can be avoided by using upwinded differencing for the convective terms or by adding explicitly a certain amount of second order or fourth order dissipation [4, p.439]. Briley & McDonald [3] used a second order dissipation term of the form $\epsilon_z \delta_z^2 \phi$, where

$$\epsilon_z = \frac{|w| \Delta z}{2} - \frac{\nu}{Re}, \quad Re_{\Delta z} > 2,$$

$$\epsilon_z = 0, \quad Re_{\Delta z} < 2.$$

This assures that the local cell Reynolds number is less than or equal to two. This dissipation term is added to each one of the governing equations with ϕ defined appropriately as in [3]. This

is done in the present work also. The dissipation term, while improving the stability of the numerical method, has a detrimental effect on the accuracy of the solution [3]. It is difficult to ascertain this loss of accuracy in a multidimensional problem such as the one we are dealing with here. Nevertheless, an attempt was made to minimize this loss of accuracy through the use of an adequate number of grid points such that all the scales of interest in the flow field are resolved properly.

4 Results & Discussion

In this section, we first present quasi 1-D solutions for the flow in a C-D nozzle, followed by viscous 2-D axi-symmetric solutions. The quasi 1-D solutions are obtained for the flow of air through a nozzle whose area variation is given as $A(z) = 1 + z^2$, $-1 \leq z \leq 10$. This profile gives an exit to throat area ratio of approximately 100. Two solutions are presented in Figure 1 - one with an exit pressure high enough to initiate a normal shock in the diverging section of the nozzle, and another where the flow accelerates smoothly from a subsonic velocity at the inlet to supersonic velocities at the exit. The fully supersonic solution has been obtained with *zero artificial dissipation*, while the other solution has been obtained with an amount of artificial dissipation sufficient to make the local cell Reynolds number equal to 2. *A linearly decreasing density profile and constant values for the velocity (typically zero) and temperature (typically 273 K) are used as initial guesses to start the solution procedure.* A total of 256 points are used and the calculations are stopped when the percent change in the dependent variables is less than 0.00001%. As a check on the accuracy of the solution the mass flow rate is computed at each axial station in the nozzle, and is found to be constant to within 0.00001%. These solutions take about 10 to 15 seconds of CPU time on the Cray Y-MP. It can be seen in Figure 1 that the two curves are barely distinguishable from each other up until the shock, which shows that the effect of the added artificial dissipation on the accuracy of the solution is minimal. We now turn to a discussion of the viscous flow solutions.

All the viscous flow solutions presented here are for the flow of air ($\gamma = 1.4, Pr = 0.701$) through a nozzle whose geometry is shown in Figure 2. It has a converging and a diverging section in which the outer radius of the nozzle is a linear function of the axial coordinate. The transition from the converging to the diverging section is achieved within five grid points through the use of a quadratically varying profile for the outer radius. The exit to throat area ratio for this nozzle geometry is 25. Our interest in this geometry arises from its use in space propulsion applications [14]. All the solutions presented here are obtained on a non-uniform grid with 256 points in the axial direction and 64 points in the radial direction. The calculations are performed until the percent change in the dependent variables is less than 0.00001%.

It is *essential* to specify proper initial conditions in order to obtain the supersonic solutions that are presented here. While this may not be necessary in the case of C-D nozzles with smaller area ratios, we find this to be crucial for the large area ratio that we consider here. The key feature of this initial guess is that it must allow the C-D nozzle to choke *very quickly*. This is important because once the nozzle chokes, the flow in the diverging section reaches supersonic velocities quite rapidly. The appropriate initial guess can be generated by solving the flow in a geometry that has the same converging section as the C-D nozzle followed by a constant area

section (with area equal to the throat area) in place of the diverging section. The exit static pressure of this geometry is adjusted until a converged solution with a maximum exit Mach number close to but less than one is obtained. This solution is then used as the initial guess for generating the flowfield in the C-D nozzle. For the present case, on the 256x64 grid, it takes approximately 4-5 minutes of CPU time on a Cray Y-MP to generate this initial guess. The desirable feature of this procedure is that it is easy to generate this initial guess even in complex geometries with minimal computational effort. With this initial guess, it takes approximately 8-10 minutes of CPU time on the Cray to obtain the solutions for the C-D nozzle, which are discussed in the following paragraphs.

The velocity vectors for the flow in the C-D nozzle at a Reynolds number (as defined in Section 2) of 50,000 are shown in Figure 3. A throat radius of 2 mm, inlet stagnation pressure of $1.03 \times 10^5 \text{ N/m}^2$, inlet stagnation temperature of 300 K and a coefficient of viscosity $\mu = 18 \times 10^{-6} \text{ N s/m}^2$ are used for calculating this Reynolds number. Different values of Reynolds numbers can be obtained, for example, by adjusting the inlet stagnation quantities. The velocity vectors show quite clearly the growth of the boundary layer near the wall in the diverging section. Only one half of the total number of points in the radial direction and one tenth of the total number in axial direction are shown in this figure for the sake of clarity. One can also see some wall-jet type velocity profiles in the vicinity of the throat where the flow accelerates rapidly in order to negotiate the sharp corner.

Profiles of Mach number along the radial grid lines $j = 0$ and $j = 38$ are shown in Figure 4 together with the Mach number profile from the corresponding frictionless, quasi 1-D solution. Here, the grid line corresponding to $j = 0$ represents the centerline. The profile along the $j = 38$ grid line is closest to the quasi 1-D profile. The maximum exit Mach number in the viscous case is about 4.6, which is less than the value of about 5.0 for the frictionless, quasi 1-D case. The profile along the centerline shows a sharp drop in the Mach number near a dimensionless axial coordinate of 8. One can see from the Mach number contours in Figure 5, a change in the shapes of these contours near the same axial location ($z \approx 8$). In this figure, the sonic line ($M=1$) is shown as the thick line. The radial Mach number profiles have their maxima located on the centerline up until $z = 8$ and these maxima move to a location near the center of the channel once we cross this particular axial location. These contours look very similar to those obtained using the method of characteristics [15] for inviscid flow in a similar geometry. They also agree very well qualitatively with the experimental results presented in [16]. It was first shown by Darwell & Badham [15] that compression waves could be generated in C-D nozzle geometries from the location where the curved throat section meets the diverging conical section, if the radius of curvature of the nozzle wall profile is discontinuous at this location. These compression waves can coalesce at the centerline at a point downstream to form a weak oblique shock. Experiments conducted subsequently by Back et al. [17, 18] and Cuffel et al. [16] showed this to be indeed true. The sharp drop in the Mach number along the centerline in Figure 4 is due the oblique shocks intersecting the centerline and the change in the shapes of the Mach number contours mentioned before is due to these incoming and reflected weak oblique shock waves. Indeed, the similarity between Figure 4 and the experimental profiles of Back et al. [17, Figure 2] is striking.

The exact mechanism by which these compression waves are generated is discussed in detail in [15, 18]. As the flow passes through the throat, the regions of the flow close to the wall are overturned so as to be parallel to the wall. Consequently, when the location where the

discontinuous change in wall curvature occurs is reached, the flow must be turned back towards the centerline, i.e. away from the wall. This can only occur through a series of compression waves. This can be seen quite clearly in Figure 6, where the dimensionless wall static pressure is plotted. A bump can be seen in the curve immediately past the throat section which is located at $z=4$. This bump is shown enlarged in the inset. Again, this profile shows excellent qualitative agreement with the corresponding plot in [18, Figures 3,5].

The existence of the incident and the reflected oblique shock waves can be seen clearly in the next two figures. Figure 7 shows a plot of the radial velocity along the grid line $j = 8$. The radial velocity is negative in the converging section and then it rapidly turns around at the throat becoming positive in the diverging section. The radial velocity then decreases sharply in the neighbourhood of $z = 8$ and becomes negative as the flow traverses the incident oblique shock waves. The fluid is turned in a clockwise direction towards the centerline by these waves, since they are right running. The radial velocity then increases just as rapidly, as the flow traverses the oblique shocks that are reflected from the centerline. These turn the fluid in an anti-clockwise direction away from the centerline, being left running waves. The radial velocity settles down to a constant value after about $z = 14$. The overturning of the fluid as it goes through the throat is evident from this figure when one compares the value of the radial velocity near $z \approx 7$ with the final value for $z > 14$.

The total pressure along the centerline ($j = 0$) and along the radial grid line $j = 10$ is plotted in Figure 8. The total pressure is essentially constant in the converging section where the boundary layer is developing so that the flow is mostly inviscid. But viscous effects become important in the throat region and the total pressure increases as a result of heating due to viscous dissipation. The total pressure then decreases continuously as the flow accelerates to supersonic speeds and *increases* across the incident and reflected oblique shock waves. In the case of the profile along the centerline, this increase is quite a sharp one, but away from the centerline, along $j = 10$, two bumps in the profile can be seen, each representing the pressure rise following the incident and reflected oblique shocks respectively. This agrees quite well with the experimental results ([17, Figure 1]). Mach number contours (Figure 9) and profiles (Figure 10) for a Reynolds number of 1000 (corresponding to a lower mass flow rate) show that the effects of the rapid turning near the throat are mitigated in a fully viscous flow. This is to be expected since at lower mass flow rates and lower inlet stagnation pressures, the viscous effects dominate the flow.

We now consider briefly the case where the swirl velocity at the inlet is as shown in Figure 11. This type of swirl profile is observed, for example, if the fluid were injected through ports peripheral to the nozzle wall. Thus the radial velocity at inlet is still zero, as before. The flow field in this case is very similar to the previous case with zero swirl and so they are not presented here. Contours of swirl velocity are shown in Figure 12. The injected swirl can be seen to decay within a short distance from the entrance due to viscous effects. However, we have observed that under some circumstances this injected swirl can persist and can get enhanced quite dramatically in geometries of the type used in [14].

5 Summary & Conclusions

Solutions to the 2-D, axi-symmetric, viscous, compressible flow in a C-D nozzle with a large exit to throat area ratio are presented. In addition, quasi 1-D solution for flow in a C-D nozzle with an exit to throat area ratio equal to 100 is also given. These solutions are obtained by using the LBI scheme of Briley & McDonald [3]. In order to successfully obtain solutions to this problem, proper initial and boundary conditions need to be specified as discussed in detail in this paper. We obtained solutions to the 2-D, axi-symmetric, inviscid Euler equations, though they are not presented here. This system of equations requires artificial dissipation in *both* the radial and the axial directions for numerical stability. For this reason, the so called "inviscid" solution is not truly inviscid but resembles the viscous solution quite closely. Furthermore, the computing effort required is approximately the same in both the cases and so it is better to compute the viscous solutions which are more reflective of reality than the corresponding inviscid solutions. Thus the quasi 1-D solution is the *only true inviscid solution*.

The viscous solution shows considerable departure from the quasi 1-D solution. Most importantly, oblique shocks generated due to overturning of the fluid close to the wall in the throat region are seen in the viscous solution. These oblique shocks were first predicted by Darwell & Badham [15] based on inviscid flow calculations and subsequently confirmed by the experiments of Back et al. [17, 18]. The qualitative agreement between our numerical results and the experimental results are excellent, thus illustrating the capability of the LBI scheme to capture the true physics of the problem. Addition of swirl to this flow does not produce any significant change in the flow field and the injected swirl is seen to decay.

The LBI scheme can be easily extended to three dimensions and can account for variable properties as well. It retains its unconditional stability properties in three dimensions also [11]. The scheme can also be used to study chemically reacting flows and its capability to handle the stiff systems that arise as a result of the chemical reactions has already been established [7]. Further, reacting flows such as those studied in [9] with state resolved kinetics can be effectively analyzed using the LBI method.

ACKNOWLEDGEMENTS

This work was supported by the Air Force Office of Scientific Research under Grant No. AFOSR 91-0318. We also gratefully acknowledge a grant from the Ohio Supercomputer Center for use of their Cray Y-MP. Helpful discussions with Prof. Briley of Mississippi State University are gratefully acknowledged.

References

- [1] MacCormack, R. W. *AIAA Paper 81-0110*, 1981.
- [2] Beam, R. M and Warming, R. F. *AIAA Journal*, 16, No. 4, 393-402, 1978.
- [3] Briley, W. R, and McDonald, H. *Journal of Computational Physics*, 24, pp. 372-397, 1977.

- [4] Fletcher, C. A. J, *Computational Techniques for Fluid Mechanics*, I & II, Springer-Verlag, New York, 1988.
- [5] Anderson, D. A, Tannehill, J. C and Pletcher, R. H. *Computational Fluid Mechanics and Heat Transfer*, Hemisphere Publishing Corporation, Washington, 1984.
- [6] Shamroth, S. J, Gibeling, H. J and McDonald, H. *Journal of Computational Physics*, 19, pp. 150-178, 1975.
- [7] Gibeling, H. J and Buggeln, R. C. *AIAA Paper No 91-2077*, 1991.
- [8] Russell, P. K and Pepper, D. W. *Numerical Heat Transfer with Personal Computers and Supercomputing: National Heat Transfer Conference*, R.K. Shah (Ed.), HTD 110, ASME, New York, N.Y, 1989.
- [9] Chiroux de Gavelle de Roany, A., Flament, C, Rich, J. W, Subramaniam, V. V and Warren, W. R. *AIAA Journal*, (In Press).
- [10] Vincenti, W. G and Kruger C. H. *Introduction to Physical Gas Dynamics*, John Wiley and Sons, Inc., New York, N.Y, 1965.
- [11] Briley, W. R, and McDonald, H. *Journal of Computational Physics*, 34, pp. 54-73, 1980.
- [12] Babu, V. *On the Numerical Solution of Incompressible, Three-Dimensional Navier-Stokes Equations*, Ph.D. Thesis, The Ohio State University, Columbus, Ohio, August, 1991.
- [13] Roache, P. J. *Computational Fluid Dynamics*, Hermosa Publishers, New Mexico, 1972.
- [14] Auweter-Kurtz, M., Kurtz, H. L, Schrade, H. O and Sleziona, P. C. *Journal of Propulsion and Power*, 5, No. 1, pp. 49-55, 1989.
- [15] Darwell, H. M and Badham, H. *AIAA Journal*, 1, No. 8, pp. 1932-1934, 1963.
- [16] Cuffel, R. F, Back, L. H and Massier, P. F. *AIAA Journal*, 7, No. 7, pp. 1364-1366, 1969.
- [17] Back, L. H and Cuffel, R. F. *AIAA Journal*, 4, No. 12, pp. 2219-2221, 1966.
- [18] Back, L. H, Massier, P. F and Cuffel, R. F. *Journal of Spacecraft*, 4, No. 8, pp. 1040-1047, 1967.

List Of Figures

Figure 1. Quasi 1-D Solutions.

Figure 2. C-D Nozzle Geometry.

Figure 3. Velocity vectors at $Re = 50,000$, with Re as defined in Section 2.

Figure 4. Mach number profiles along the centerline ($j = 0$) and $j = 38$ at $Re = 50,000$.

Figure 5. Contours of Mach number at $Re = 50,000$. The Mach 1 contour is indicated by a thick line.

Figure 6. Wall ($j = 64$) static pressure at $Re = 50,000$.

Figure 7. Radial velocity profile along $j = 8$ at $Re = 50,000$.

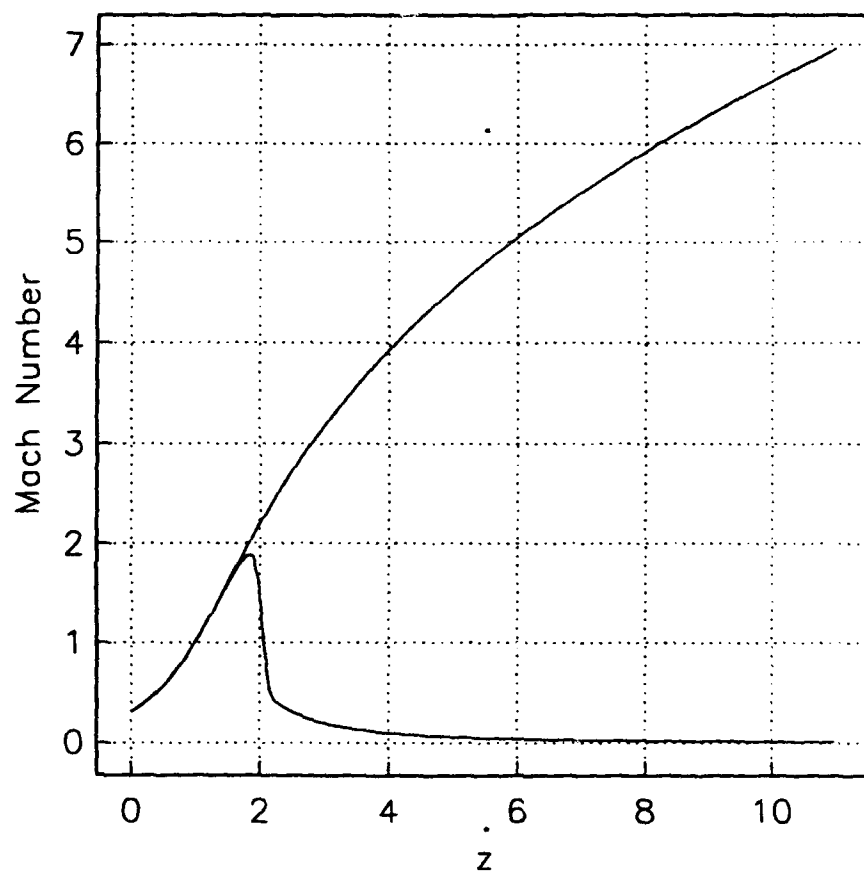
Figure 8. Total pressure along the centerline ($j = 0$) and $j = 10$ at $Re = 50,000$.

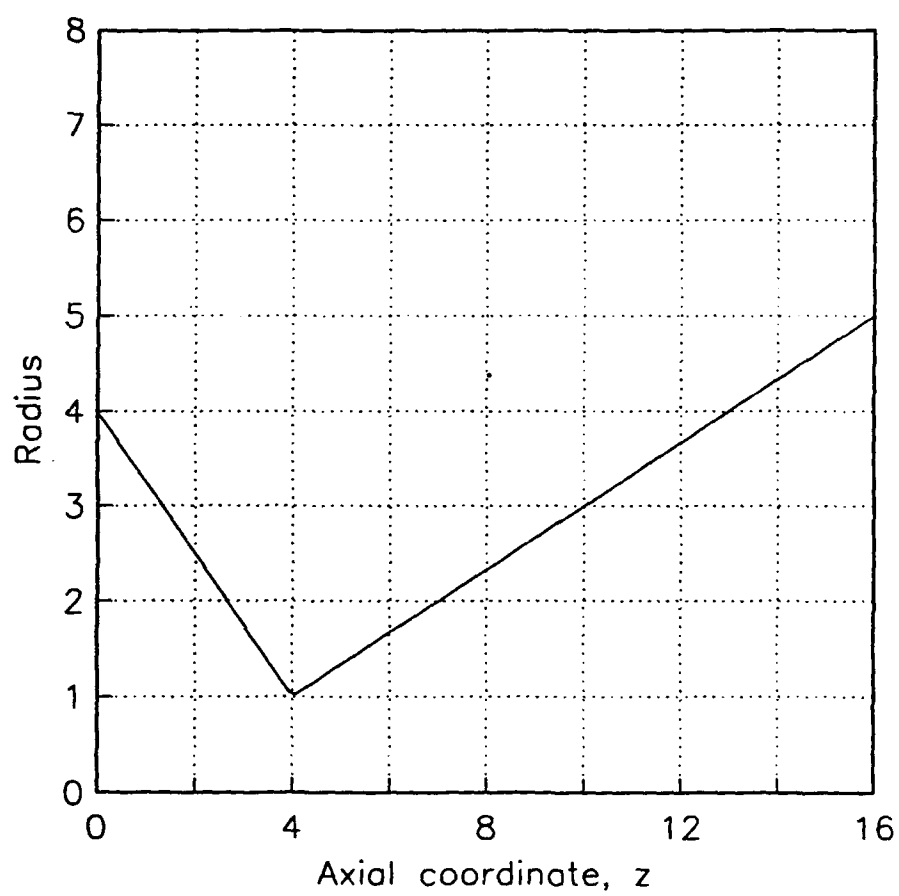
Figure 9. Mach number profiles along the centerline ($j = 0$) and $j = 38$ at $Re = 1000$.

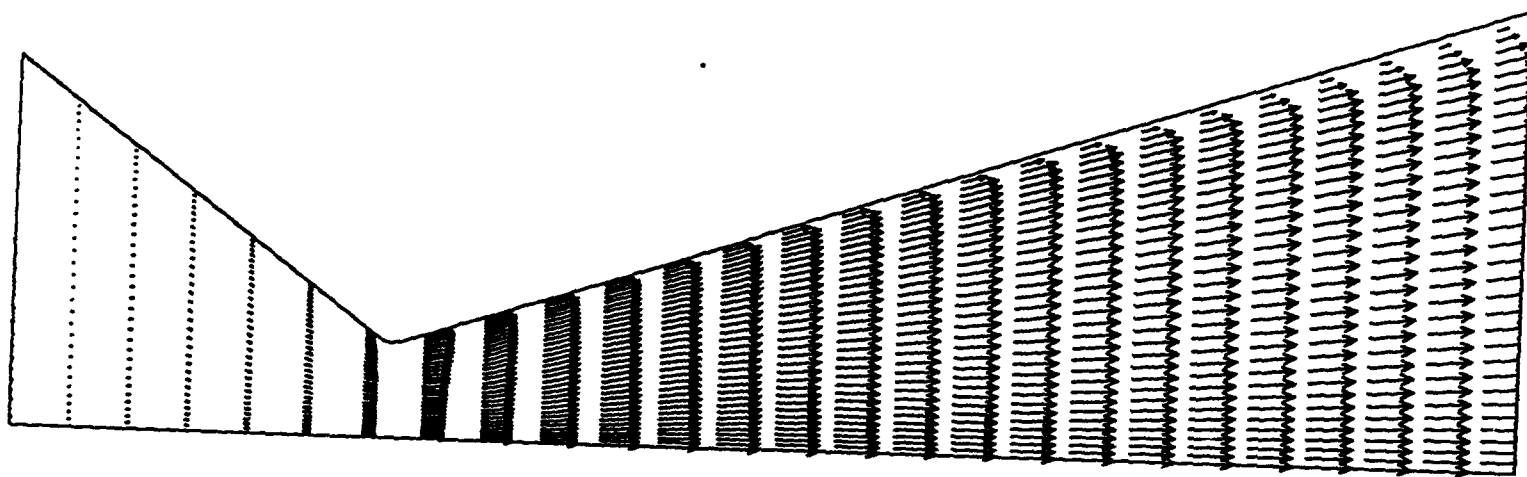
Figure 10. Contours of Mach number at $Re = 1000$.

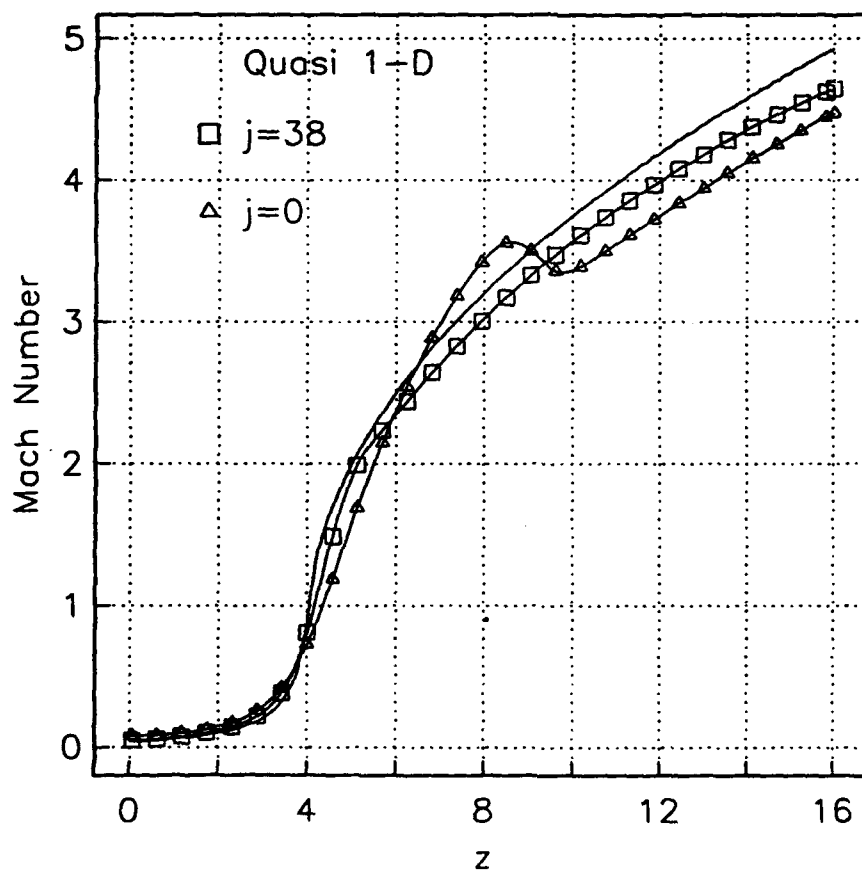
Figure 11. Swirl velocity profile at inlet.

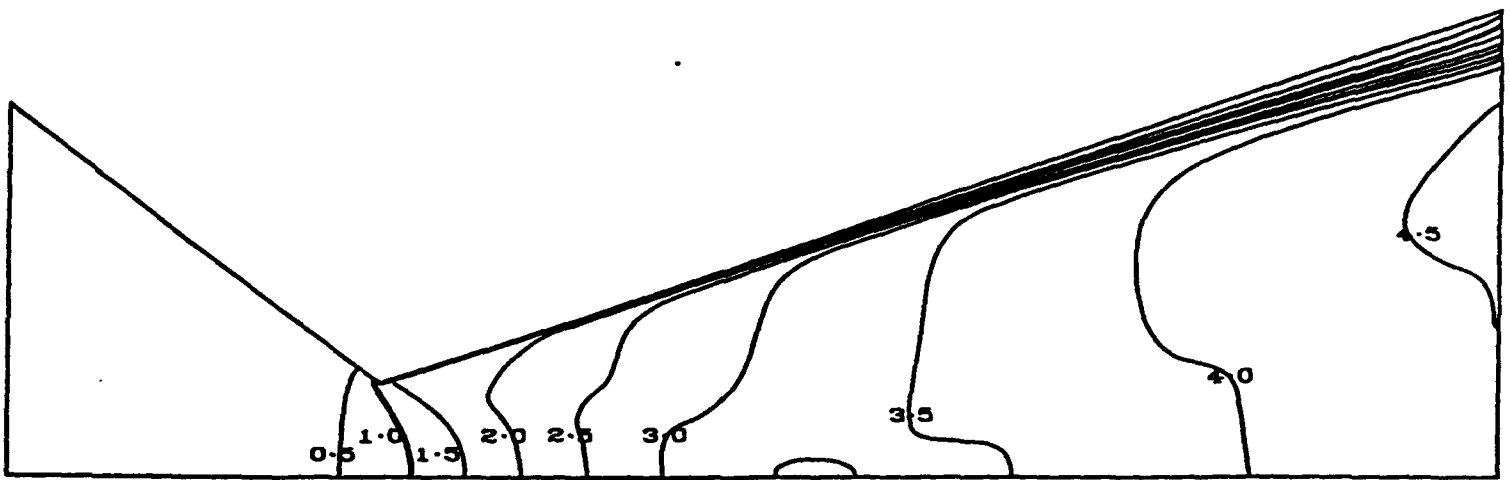
Figure 12. Contours of swirl velocity at $Re = 50,000$. The contours decrease in value geometrically by a factor of 10 from left to right.



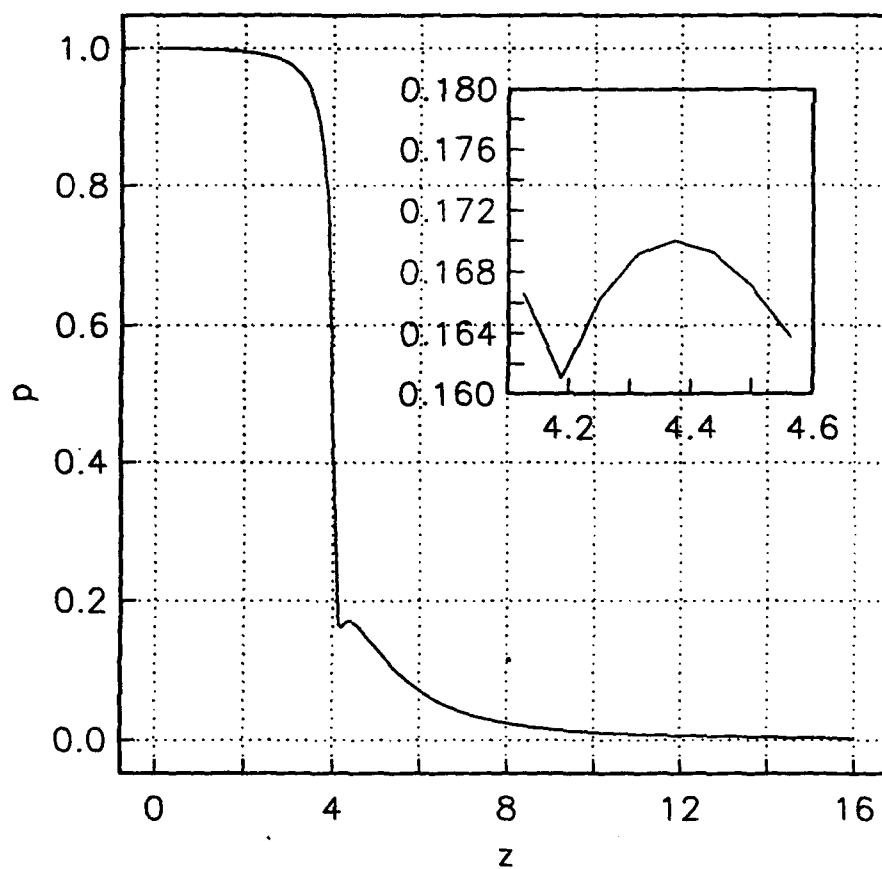


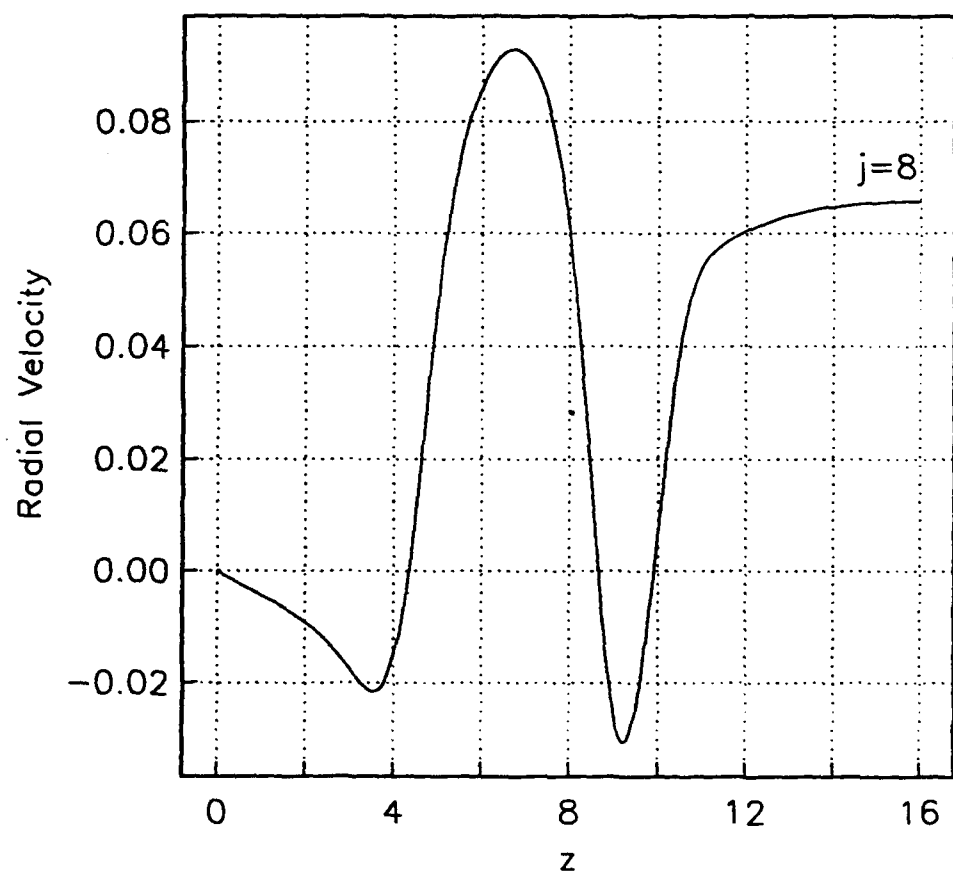


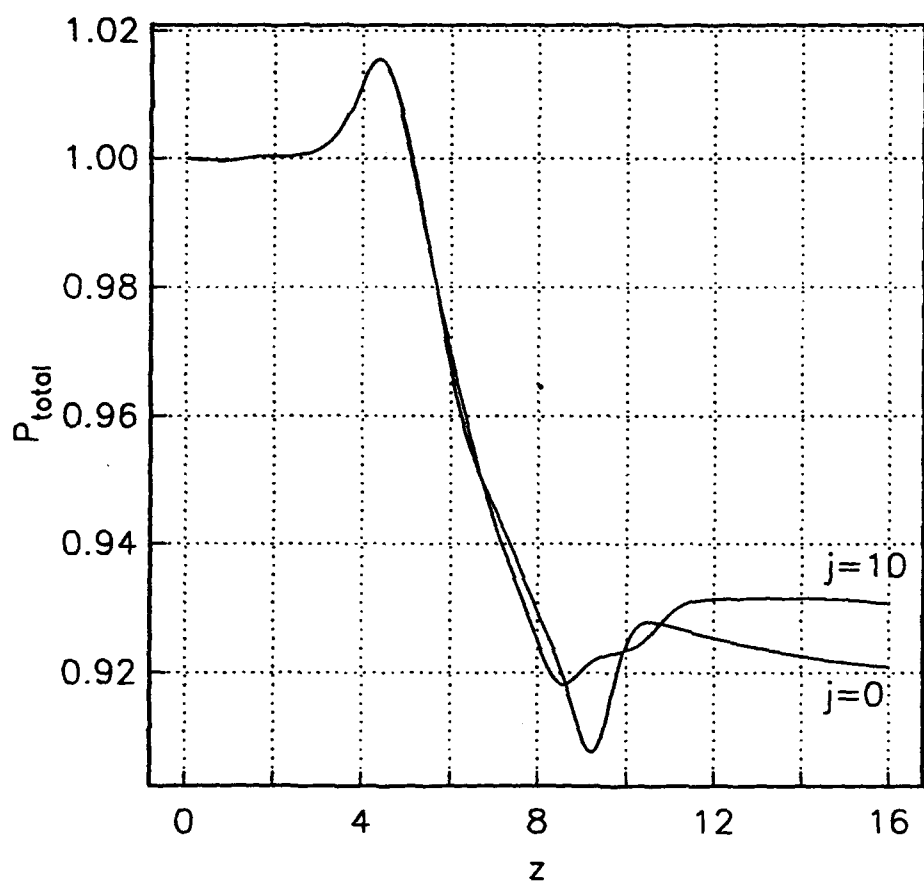


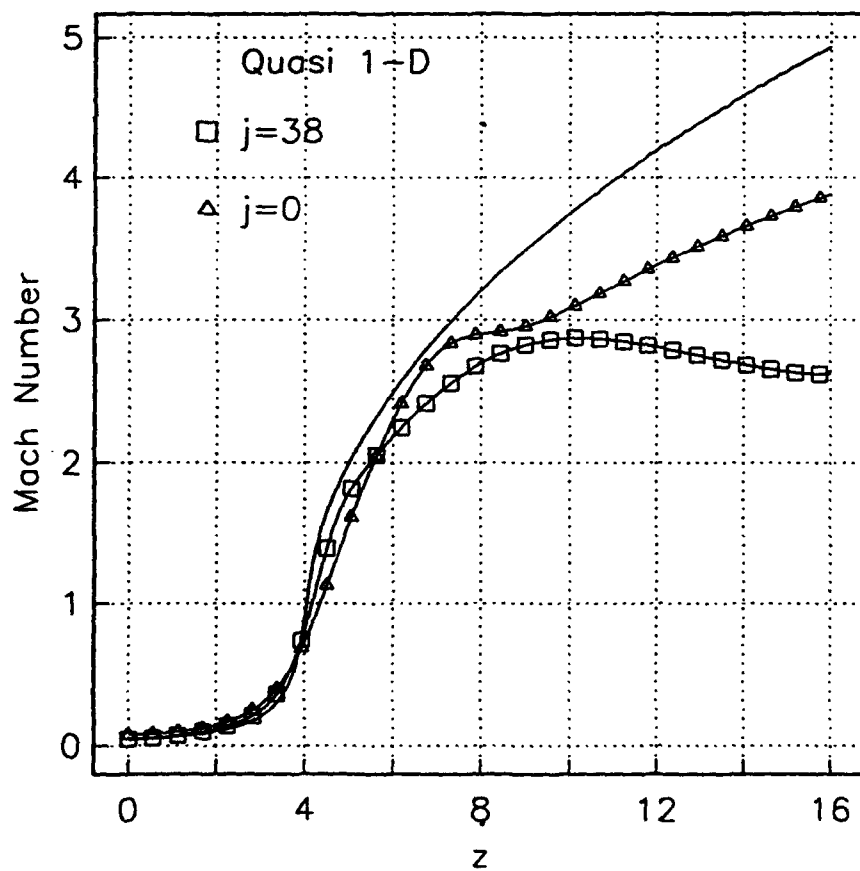


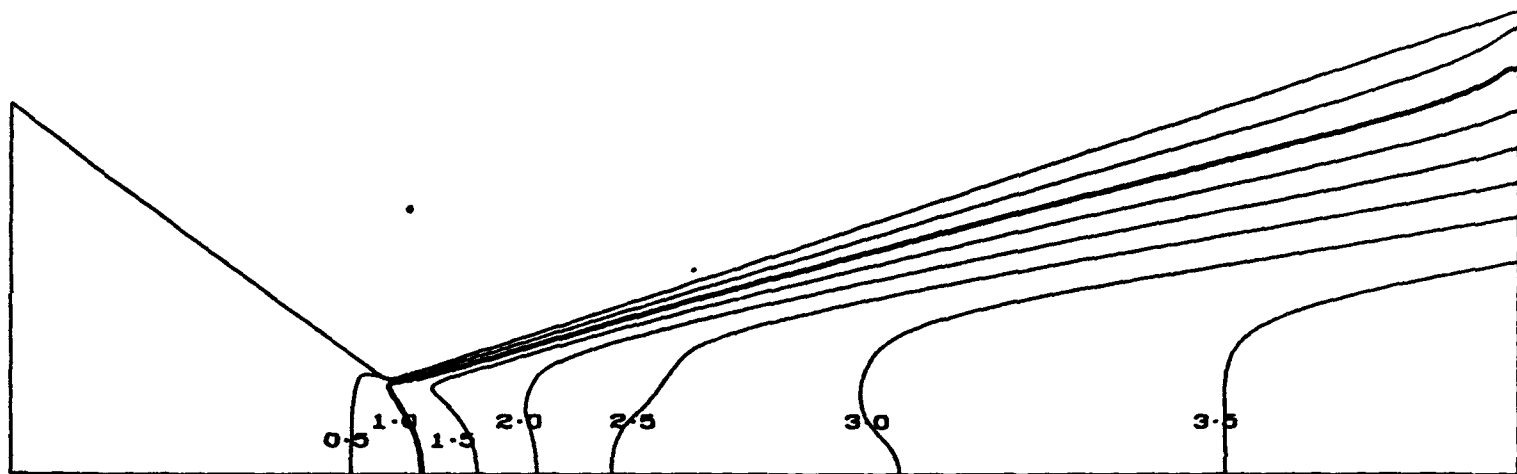
Mach Number

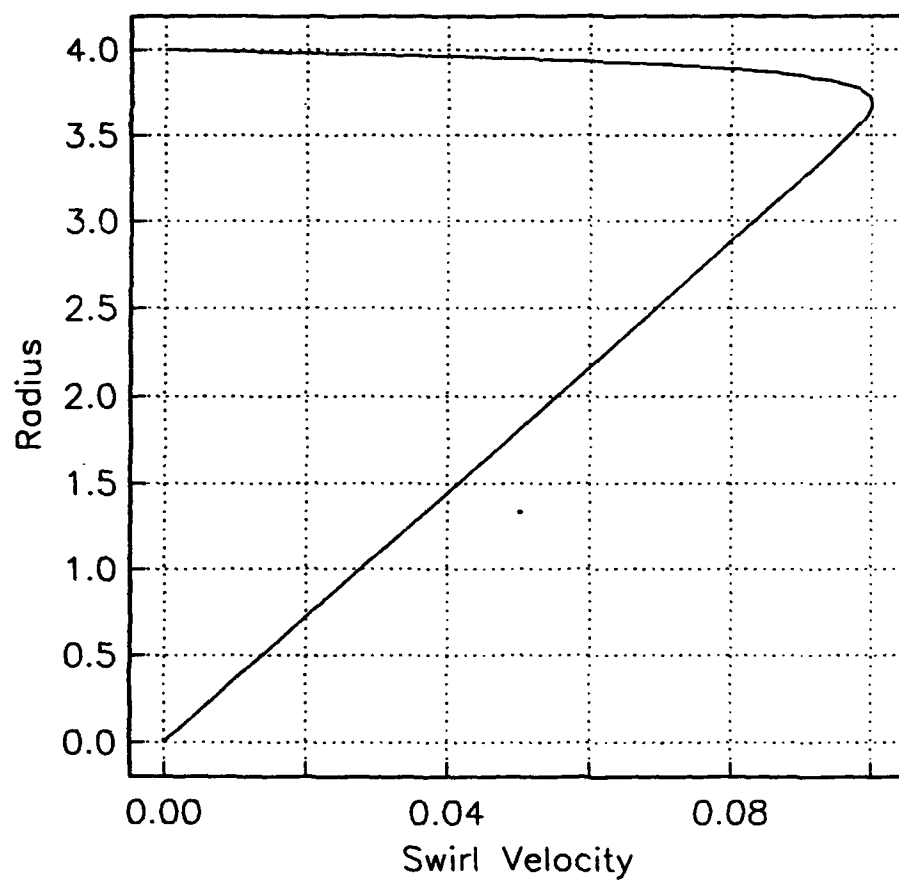




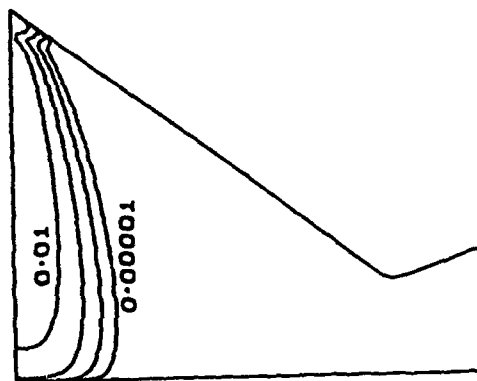








13/2



APPENDIX B

IEPC-93-129

**VIBRATIONAL NON-EQUILIBRIUM
IN ARCJET FLOWS**

V. BABU, S. AITHAL, AND V. V. SUBRAMANIAM

**Department of Mechanical Engineering
The Ohio State University
Columbus, Ohio 43210**

**23rd International Electric Propulsion
Conference**

September 13-17, 1993 / Seattle, Washington

ABSTRACT

Arcjets operating on molecular propellants such as ammonia or hydrazine are expected to produce significant amounts of diatomic species such as N_2 , NH , and H_2 in the discharge [1]. Internal mode energy exchange (Vibration-Vibration, Vibration-Electronic, Electronic-Electronic, and Vibration-Translation) between these molecules can result in highly non-Maxwellian distribution of energies within their internal modes of vibration, electronic excitation, and rotation. These diatomic species are also extremely effective in moderating electron energies via inelastic collisions involving their internal modes (vibration, electronic excitation, and rotation). Consequently, the electron energies in arcjets operating on such molecular propellants are strongly related to and determined by the distribution of molecules in various vibrationally and electronically excited states. Under these conditions therefore, the concept of an electron temperature loses meaning. Instead, one must refer to electron energy distribution, or an average electron energy if a meaningful average exists. The modelling of such inter-mode energy transfer is extremely complicated and presents a challenge to the areas of chemical physics and numerical analysis. In this paper, we present numerical solutions to quasi one-dimensional supersonic flows with state-specific vibrational rate kinetics. These simulations represent some of the energetics expected to occur in arcjets. This work is a necessary first step before complete modelling of the discharge including the effects of electron-impact processes (see also [2]). The numerical method used here is the Linearized Block Implicit (LBI) method of Briley & McDonald [3]. The LBI method has excellent stability properties and extends easily to multi-dimensions. Formulation of the boundary and initial conditions for this problem are discussed in detail, and these essentially carry over for similar 2-D

and 3-D cases.

Nomenclature

A	cross-sectional area of the nozzle (m^2)
e	internal energy per unit volume (J/m^3)
$E_{i,v}$	energy of vibrational level v of species i (J)
k	Boltzmann's constant (J/K)
$M_{i,v}$	molecular mass of the diatomic species (kg)
M_m	atomic or molecular mass of the diluent species (kg)
$n_{i,v}$	number density of vibrationally active species i at level v (m^{-3})
n_m	number density of diluent species m (m^{-3})
N_d	number of vibrationally active species
N_m	number of diluent species
p	pressure (N/m^2)
p_0	reservoir pressure (N/m^2)
t	time (s)
T	temperature (K)
T_0	reservoir temperature (K)
u	velocity (m/s)
V_{max}	highest vibrational level considered in the diatomic species
x	axial or streamwise coordinate (m)
ρ	mass density (kg/m^3)

1 Introduction

Arcjet thrusters are electrothermal devices where a propellant stream is ohmically heated and subsequently expanded to supersonic speeds. These thrusters are capable of robust operation using a variety of propellants including monatomic and polyatomic gases. The energy added into the gas is distributed into thermal heating (i.e. increase in translational mode temperature) and into various internal modes (electronic excitation, vibration, and rotation). However, it is mainly the thermal

heating which is subsequently converted into directed kinetic energy (i.e. useful thrust) in the nozzle. Thus, any energy distributed into the internal modes which is subsequently not recovered in translational motion is lost and referred to as a "frozen flow loss". This work is a first step toward predicting frozen flow losses.

The internal mode energy exchange between molecules in a discharge not only results in re-distribution of input electrical energy, but also determines, moderates, and governs electron energy distributions. Electrons which normally acquire large kinetic energies from applied electric fields in monatomic gases, are restricted from doing so in plasmas containing appreciable amounts of molecular species. This is because inelastic collisions between electrons and molecules results in transfer of electron kinetic energy to vibrational, electronic, or rotational excitation. Since energy exchange between molecules also occurs in these discharges, the well known non-Maxwellian distribution such as Treanor distribution[4] occurs among the molecules such as N_2 , thereby leading to highly non-Maxwellian electron energy distributions. Such distributions can occur at low pressures in molecules such as N_2 and CO (100 torr) [5] or supra-atmospheric pressures (20 atm.) [6]. Consequently, it is likely that the concept of an electron temperature in arcjet plasmas is meaningless and that one must resort to electron energies or a mean electron energy instead.

Arcjet thrusters operating at low or moderate powers in the range of 1 KW to 30 KW on ammonia (NH_3) or hydrazine (H_4N_2) are expected to produce significant amounts of N_2 , NH , and H_2 . The pressure varies from 100 torr in the nozzle to an atmosphere or several atmospheres in the constrictor or upstream of the constrictor. Typically, the E/N in these thrusters vary over a wide range: $10^{-23}V - m^2 \leq E/N \leq 10^{-16}V - m^2$ (or $10^{-19}V - cm^2 \leq E/N \leq 10^{-12}V - cm^2$). Molecular discharges

in N_2 have been studied extensively in the past (for instance see [5]) over a range that is partially applicable to arcjet flows. Such studies offer valuable insight into the nature of the electron energy distribution function. For instance, Fig. 1 from [5] shows the calculated Electron Energy Distribution Functions (EEDFs) in N_2 discharges for a variety of E/N ratios. It is to be emphasized that this figure is a semi-log plot so that a Maxwell-Boltzmann distribution would be shown as a sloping, straight line on such a plot. As can be seen from Fig.1, the *EEDFs are markedly non-Maxwellian*. This has dramatic consequences for evaluation of transport properties since cross-sections for collisional processes are averaged over energy distributions (usually taken to be Maxwellian).

It is also instructive to examine the "fractional power transfer" versus E/N for N_2 discharges as given by Nighan [5], shown here in Fig. 2. With respect to the arcjet, this figure may be interpreted as follows. At low powers characterized by the lower E/N values displayed in Fig. 2, it can be seen that much of the energy added to the discharge goes into the vibrational modes of N_2 . Electronic excitation gains prominence as E/N is increased, with ionization only beginning to consume input power at E/N s approaching $10^{-15}V - cm^2$. Note the conspicuous absence of dissociation, which is understandable since the dissociation energy of N_2 is 9.76 eV and the E/N s in Fig. 2 are lower than those corresponding to average electron energies less than 3 eV. It is therefore clear from this example that *scaling up in power* for arcjets operating on nitrogen, ammonia, or hydrazine is strongly dependent on the degree of dis-equilibria between the various internal modes. Frozen flow losses and losses in efficiency are therefore related to vibrational, electronic, and rotational mode non-equilibrium. Several recent works have already pointed to striking differences between rotational, vibrational, and translational energies in the plumes

of arcjet thrusters[1, 7].

Flows with high degree of vibrational, electronic, and chemical non-equilibrium occur in many other engineering applications. These include flow in gas dynamic lasers, rocket thrusters (chemical and electrical) and chemical vapor deposition (CVD) processes. A typical feature of these non-equilibrium flows is the large variation in characteristic times for internal processes which can vary by as much as thirty to forty orders of magnitude or more in various regions of a flow. In applications where the effects of state-specific kinetics or large number of elementary reactions have to be incorporated, there is a need for a robust, efficient, reliable, and accurate numerical method to simulate such flows.

Recently, numerical solutions to supersonic nozzle flows with high degree of vibrational non-equilibrium and state-specific kinetics have been presented [8]. These quasi 1-D solutions were obtained by integrating the steady forms of the governing equations using the stiff equation integrator LSODE [9]. While it is possible to obtain solutions to 1-D problems using this strategy, it does not extend to multi-dimensions. This is a serious drawback if one wants to study such flows in two- and three-dimensions, while including the effects of heat conduction and viscosity. Our interest in these multi-dimensional flows arises from the need to quantify the frozen flow losses and redistribution of input electrical energy in arcjet thrusters. Hence, it is desirable to have an efficient method that can handle such stiff problems and extend from 1-D all the way to 3-D. The Linearized Block Implicit (LBI) scheme of Briley & McDonald [3] is such a method. As we show in a recent work [2], this method is very well suited for studying viscous, internal flows in geometries with high exit to throat area ratios. Our ultimate goal is to be able to study these internal flows after including the effects of vibrational and chemical non-equilibrium with

state-specific kinetics.

In this paper, we tackle the first steps in calculating vibrational mode non-equilibrium, simulating the energy loading in the arcjet thruster. It must be pointed out at the outset that the results we present here do not account for the electric discharge in the arcjet unlike [2]. Rather, we simulate the energy loading of the arc as an initial total temperature to which the propellant stream is heated before expansion through the nozzle. Work incorporating vibrational/electronic mode disequilibrium together with the discharge phenomena is presently underway, and will be reported later. We focus here on flows of pure N_2 , N_2/H_2 , N_2/Ar , and $N_2/CO/Ar$ mixtures to illustrate the effects of inter-molecular and intra-molecular V-V (Vibration-to-Vibration) and V-T (Vibration-to-Translation) energy transfer. Our present work thus differs in approach and scope from previous or ongoing work [10, 11, 12, 13, 14, 15, 16, 17].

This paper is organized as follows. Formulation of the problem which differs from [8] is discussed in the next section, followed by a discussion of the numerical method in section 3. Results are discussed in section 4, followed finally by a summary and conclusions.

2 Formulation

In the arcjet, much of the ohmic dissipation takes place in the constrictor region and upstream of the nozzle. This addition of energy to the upstream subsonic propellant can be viewed as an addition of thermal energy to the flowing propellant stream driving it to choke and accelerate to supersonic speeds. Although the following is not a completely true description of the arcjet operation, the present results serve to illustrate the role of molecular energy transfer in arcjet flows. Since the problem formulation and solution methodology that is used

in the present work is completely different from that used in [8], we present them in detail here. The governing equations are the quasi 1-D gas dynamic equations together with species conservation equations [8]. These are written as follows :

$$\frac{\partial \rho}{\partial t} + \frac{1}{A} \frac{\partial(\rho u A)}{\partial x} = 0, \quad (1)$$

$$\frac{\partial(\rho u)}{\partial t} + \frac{1}{A} \frac{\partial(\rho u^2 A)}{\partial x} = -\frac{\partial p}{\partial x}, \quad (2)$$

$$\frac{\partial}{\partial t} \left(e + \frac{\rho u^2}{2} \right) + \frac{1}{A} \frac{\partial}{\partial x} \left[u A \left(e + p + \frac{\rho u^2}{2} \right) \right] = 0, \quad (3)$$

$$\frac{\partial n_{i,v}}{\partial t} + \frac{1}{A} \frac{\partial(n_{i,v} u A)}{\partial x} = VT_{i,v} + VV_{i,v} + SRD_{i,v}, \quad 1 \leq i \leq N_d, \quad 0 \leq v \leq V_{max} \quad (4)$$

$$\frac{\partial n_m}{\partial t} + \frac{1}{A} \frac{\partial(n_m u A)}{\partial x} = 0, \quad 1 \leq m \leq N_m \quad (5)$$

where the subscripts i, v refer to diatomic species i in vibrational state v and the subscript m refers to diluent species m (usually monatomic). In addition, only the diatomic species are assumed to be vibrationally active and $V_{max} + 1$ is the total number of vibrational levels considered in each of the diatomic species. $E_{i,v}$ is calculated by treating the diatomic molecules as anharmonic oscillators [8]. The heat of formation of various species can be included in the energy equation. However, since chemical reactions are not considered in the examples presented here, they have been left out of Eq. (3). Also, energy of the electronic levels is neglected as we do not include electronic transitions in the examples. The radiative loss which would appear as a sink term on the right hand side of Eq. (3), is neglected here since it is expected to be small for the

optically thin gases considered here. These assumptions do not indicate a loss of generality, since all these terms can be included in the formulation if applicable.

The pressure is related to the temperature and the number densities through the following equation of state :

$$p = \left(\sum_{i=1}^{N_d} \sum_{v=0}^{V_{max}} n_{i,v} + \sum_{m=1}^{N_m} n_m \right) kT, \quad (6)$$

and the mass density is related to the number densities as follows :

$$\rho = \sum_{i=1}^{N_d} \sum_{v=0}^{V_{max}} M_i n_{i,v} + \sum_{m=1}^{N_m} M_m n_m, \quad (7)$$

where M stands for the atomic or molecular mass of the respective species. The internal energy per unit volume is given by the following, assuming equilibrium between the translational and rotational modes :

$$e = \frac{3}{2} kT \sum_{m=1}^{N_m} n_m + \sum_{i=1}^{N_d} \sum_{v=0}^{V_{max}} n_{i,v} \left(\frac{5}{2} kT + E_{i,v} \right). \quad (8)$$

The terms on the right hand side of Eq. (4) represent the state-specific Vibration-Translation (VT), Vibration-Vibration (VV) and Spontaneous Radiative Decay (SRD) terms as described by Dunnwald et al. [18] and the reader is referred to their work for the detailed expressions for these terms.

2.1 Boundary Conditions

We assume that a large reservoir is present upstream of the nozzle and that the conditions in the reservoir such as temperature, pressure, and volume fractions of the various species present are known. Further, it is assumed that

the diatomic species are in Boltzmann equilibrium both in the reservoir and at the nozzle inlet plane and that the mixture is compositionally frozen between these two locations. In addition, heat losses and frictional losses in going from the reservoir to the nozzle inlet are assumed to be negligible, without any loss of generality.

With the above assumptions, we can relate the conditions at the nozzle inlet to those at the reservoir by conservation of energy. This gives us an equation that involves the velocity, temperature, and total number density ($= \sum_{i=1}^{N_d} \sum_{v=0}^{V_{max}} n_{i,v} + \sum_{m=1}^{N_m} n_m$) at the inlet. Since the volume fractions of the monatomic species at the inlet are known, we can relate the individual n_m 's to the total number density. For the diatomic species, the known volume fractions at the inlet together with the fact that they are in Boltzmann equilibrium [19] allows us to relate the $n_{i,v}$'s to the total number density. Finally, we can relate the inlet static pressure, and hence the total number density (see Eq. (6)), and temperature to their respective values at the reservoir through the isentropic equation of state [20]. In the present case, the velocity at the inlet of the nozzle is small because of the large inlet-to-throat area ratio and thus the use of the isentropic equation of state is acceptable. These conditions allow us to eliminate all the dependent variables except the velocity at the inlet, which is determined through an implicit extrapolation [3]. At the exit to the nozzle, implicit extrapolation is used for all the variables since we are interested only in supersonic flows.

Although the governing equations and boundary conditions have been presented in their dimensional form in this section, it must be pointed out that they are non-dimensionalized before being solved numerically. This we do by using upstream reservoir conditions as reference quantities. This choice is especially convenient, since the reservoir con-

ditions need to be specified as boundary conditions anyway as we have already seen.

3 Numerical Method

Equations (1)-(5) together with the boundary conditions are discretized in time and linearized implicitly using the procedure outlined by Briley & McDonald [3]. Artificial dissipation in the form of a second derivative in the axial or streamwise coordinate is added to the right hand side of equations (1)-(5) to ensure numerical stability [3]. These equations are then discretized using second order accurate central differences on a non-uniform grid with fine spacings near the throat region. After eliminating the boundary points from the resulting system of linear algebraic equations using the boundary conditions, a block tridiagonal system of equations results which can be solved by using standard block LU decomposition algorithms [21]. We must note at this point that this system is linearly dependent due to the relationship between the mass density ρ and the number densities through Eq. (7), which holds at each grid point. In order to make this system linearly independent, we arbitrarily replace one of the species equations, such as the one corresponding to $i=1$ and $v=0$ at each grid point with Eq. (7) applied at that grid point. Note that this is done implicitly so that overall stability is not lost. The system of equations is now rendered linearly independent and ready to be solved.

Since we are solving the unsteady form of the governing equations here, the frozen flow solution is prescribed as the initial guess to start the solution process. This solution is obtained by *numerically* solving the above system of equations with the right hand side of Eqs. (4) set identically to zero. In principle, a truly frozen flow cannot be used as an initial guess for non-equilibrium calculations. How-

ever, in practice, these solutions exhibit deviations from the truly frozen flow solution due to discretization and round-off errors normally present in such numerical solutions. Therefore, the frozen flow solution can be used as initial guess for the non-equilibrium calculations.

4 Results & Discussion

We consider the geometry of the nominal 30 KW arcjet. However, as mentioned earlier, we do not model the arc. Rather, the effect of the arc's heating of the flow is simulated as an effective upstream total temperature. The cross-section of the nozzle as a function of the axial coordinate is shown in Fig. 3. For all the results presented here, a total of 120 grid points in the axial direction is used. The unsteady, non-equilibrium calculations are stopped when the percent change in the variables is less than or equal to 0.00001 %. The size of the dimensionless time step is about 5×10^{-7} seconds for all the cases, even though larger values can be used for some of the cases. Since the number of grid points is the same for all the cases, the total computing time for each case depends almost entirely upon the size of the blocks in the block tridiagonal system, which is equal to $3 + N_m + N_d V_{max}$. In the present study, block sizes as large as 84 (corresponding to $N_m=1$, $N_d=2$ and $V_{max}=40$) are considered. The total computing time (including the time taken for generating the initial guess) for this case of largest block size is about 4 minutes in uniprocessor mode on the Cray Y-MP, while it is about 8 minutes for the cases with a single diatomic species.

We first consider the flow of pure N_2 with the reservoir temperature at 5000 K and the reservoir pressure at 2 atm. Only the ground electronic state is modeled. The mass density, velocity and temperature along the length of the nozzle are plotted in Fig. 4. As can be

seen in this figure, the gradients of these quantities are quite large near the constrictor, and the open symbols (shown only for the velocity for the sake of clarity) clearly show that the non-uniform grid is able to resolve these gradients very well. Fig. 5 shows normalized population distributions for N_2 at three sections, namely, inlet, throat (exit to the constrictor) and the exit. The distribution at the throat is very close to a Boltzmann distribution, while the distribution at the exit shows considerable departure from equilibrium. As is evident, the initial energy loading of the gas upstream (i.e. via a high stagnation temperature) is re-distributed into the upper vibrational levels as the gas suddenly expands and cools. This effect is well known, and referred to as anharmonic V-V (Vibration-Vibration) pumping [4]. This effect occurs when conditions are such that V-V rates are much faster than V-T rates, typical of conditions in supersonic expansions. These distributions agree well with those presented in [8].

The effects of adding diluents in the form of monatomic species was also studied. These diluents are added, depending on the application, in order to either inhibit or promote V-T relaxation downstream of the constrictor region. For the 20% N_2 /80% Ar mixture shown in Fig. 6, the N_2 is seen to be less V-V pumped than for the pure N_2 case (Fig. 5). Evidently, the vibrational modes of N_2 are de-excited via V-T transfer to argon. Addition of 10% H_2 also results in de-excitation of the vibrational modes of N_2 comparable to the 20% N_2 /80% Ar case, as can be seen from Fig. 7. The population distributions, however, are not as sensitive to small changes in the percentages of H_2 in the mixture as was reported in [8]. This is due to an error in the values of the constants $A_{j,k}$, $B_{j,k}$ and $C_{j,k}$ (see Table 1 in de Roany et al. [8]) used for calculating the CO- H_2 V-T rates. The correct values for these constants are shown in Table 1.

As an illustration of inter-molecular energy transfer, we consider a mixture of 20% CO, 20% N_2 , and 60% Ar. In this mixture, both CO and N_2 are vibrationally active, but only their ground electronic manifolds are modeled. We neglect vibrational energy transfer to low-lying electronic levels, although the latter could also be included within the framework of the present method. The vibrational populations of these species at the exit plane are plotted in Fig. 8. The distributions show considerable non-equilibrium and the number densities of N_2 for vibrational levels above 5 are about 2 orders of magnitude lower than those of CO. These distributions agree qualitatively with those presented in [8]. The average vibrational energy per species, defined as $\sum_{v=0}^{V_{max}} n_{i,v} E_{i,v} / \sum_{v=0}^{V_{max}} n_{i,v}$ is plotted in Fig. 9 for CO and N_2 . Dramatic transfer of vibrational energy from N_2 which has more widely spaced energy levels, to CO which has more closely spaced levels can be seen in this figure. This is in agreement with theoretical predictions [4] as well as the numerical results presented in [8]. When ammonia or hydrazine is used, species such as N_2 , H_2 , and NH are produced in the discharge. Thus vibrational energy transfer can take place between these species, ultimately affecting the electron energy distribution and making it markedly non-Maxwellian. The presence of such vibrationally excited molecules will thus influence transport properties such as electrical conductivity.

5 Summary & Conclusions

Representative quasi 1-D solutions for flow in a nominal 30 KW arcjet geometry exhibiting strong vibrational non-equilibrium, are presented. Although the arc is not modeled, its presence is simulated using a high value for the inlet stagnation temperature. The results are therefore somewhat representative of the vi-

brational populations of the ground electronic states of the relevant diatomic molecules. Since electron energies are primarily dependent on inelastic collisions with molecules such as N_2 , their distribution in non-Boltzmann or non-Maxwellian since these diatomic species exhibit significant departures from equilibrium. Hence transport properties which depend on cross sections averaged over these distributions are markedly affected. This work underscores the importance of considering inelastic electron impact processes for evaluating transport properties in arcjet flows correctly.

These solutions are obtained with the LBI scheme of Briley & McDonald [3] using state-specific kinetics. This algorithm has excellent stability properties and allows the use of quite large time steps even in such stiff systems. This feature is particularly desirable when performing such calculations in multi-dimensions. The boundary and initial conditions that are discussed here carry over to multi-dimensional problems as well. The present method is therefore well suited to studying high speed, multi-dimensional, reacting, plasma flows such as those encountered in arcjet thrusters. Incorporation of the detailed kinetic processes discussed herein into a 2-D axi-symmetric model reported in [2] is presently underway.

ACKNOWLEDGEMENTS

This work was supported by the Air Force Office of Scientific Research under Grant No. AFOSR 91-0318. Additionally, we gratefully acknowledge a grant from the Ohio Supercomputer Center for use of their Cray Y-MP.

APPENDIX

The detailed expressions for the VT, VV and the SRD terms are given here. Even though the expressions presented here look identical to those given in [8], there are some minor differences between the two due to typographical errors in [8].

$E_{i,v}$, the vibrational energy at level v of species i is given by :

$$E_{i,v} = \frac{1.6022 \times 10^{-19}}{8065.479} \left[\omega_{ei} \left(v + \frac{1}{2} \right) - \omega_{ei} \chi_{ei} \left(v + \frac{1}{2} \right)^2 \right]$$

where the electronic energy has been neglected since we consider only ground electronic states here. In general, $E_{i,v}$ is also dependent on the rotational quantum number [22], but in this work we treat the rotational modes as being in equilibrium with the translational modes. ω_{ei} (in cm^{-1}) and χ_{ei} (dimensionless) are the spectroscopic constants for molecules of species i (see Table 4).

Vibration-Translation (VT) term

The VT term in the species equation (4) can be written in form as

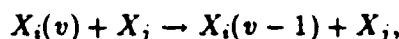
$$VT_{i,v} = \sum_{j=1}^{N_d+N_m} n_j \left[P_{i,j}^{v+1,v} (n_{i,v+1} - \exp(-\Delta E_i^v/kT) n_{i,v}) - P_{i,j}^{v,v-1} (n_{i,v} - \exp(-\Delta E_i^{v-1}/kT) n_{i,v-1}) \right]$$

where

$$n_j = \sum_{w=0}^{V_{max}} n_{j,w}$$

in the case of a vibrationally active species and $n_j = n_m$ in the case of a diluent species.

Also, $P_{i,j}^{v,v-1}$ is the rate constant (in m^3/s) of the VT transition :



where $X_i(v)$ refers to species i in vibrational state v . The rate constant is given by [8],

$$P_{i,j}^{v,v-1} = P_{i,j} \frac{v}{1 - \chi_{ei} v} F(\lambda_{i,j}^{v,v-1}),$$

where

$$F(\psi) = \frac{1}{2} (3 - e^{-2\psi/3}) e^{-2\psi/3}$$

with

$$\lambda_{i,j}^{v,v-1} = 2^{-3/2} \sqrt{\frac{\Theta_{i,j}^*}{T}} \frac{|\Delta E_i^{v-1}|}{k\Theta_i}.$$

Here $\Delta E_i^{v-1} = E_{i,v} - E_{i,v-1}$ is the difference in energy between products and reactants in the VT transition; $\Theta_i = hc\omega_{ei}/k$ (with c , the speed of light in cm/s) is the vibrational characteristic temperature (in K) of species i ; $\Theta_{i,j} = 16\pi^4 \mu_{i,j} c^2 \omega_{ei}^2 l^2 / k$ is in K where $\mu_{i,j}$ is the reduced mass in kg and $l (= 0.2 \times 10^{-10} \text{ m})$ is the range parameter [23].

In the above expression for the rate constant, $P_{i,j}$ is a coefficient that allows for fitting to the available experimental relaxation data for the 1-0 transition rate i.e. $P_{i,j}^{1,0}$. It is given (in m^3/s) as :

$$P_{i,j} = \frac{10^{-13} (1 - \chi_{ei}) kT}{(\tau p)_{i,j} F_{i,j}^{1,0} [1 - \exp(-\Theta_i/(T))]}$$

Here $(\tau p)_{i,j}$ is the vibrational relaxation time in $\mu\text{s.atm}$ and is expressed as :

$$\ln(\tau p)_{i,j} = A_{i,j} + B_{i,j}(T)^{-1/3} + C_{i,j}(T)^{-2/3}$$

where $A_{i,j}$, $B_{i,j}$ and $C_{i,j}$ are empirical constants chosen to match the experimental data. They are given in Table 1.

Vibration-Vibration (VV) term

The VV term in the species equation (4) can be written in as

$$VV_{i,v} = \sum_{j=1}^{N_d} \sum_{w=0}^{V_{max}} Q_{i,j;w,w+1}^{v+1,v} [n_{i,v+1} n_{j,w} - \exp(-(\Delta E_i^v - \Delta E_j^w)/kT) n_{i,v} n_{j,w+1}] - Q_{i,j;w,w+1}^{v,v-1} [n_{i,v} n_{j,w} - \exp(-(\Delta E_i^{v-1} - \Delta E_j^w)/kT) n_{i,v-1} n_{j,w+1}]$$

where $Q_{i,j;w-1,w}^{v,v-1}$ is the rate constant (in m^3/s) of the V-V transition :



The rate constant is written as a sum of a short range and a long range contribution [8] as follows :

$$Q_{i,j;w-1,w}^{v,v-1} = Z_{i,j} (S_{i,j;w-1,w}^{v,v-1} + L_{i,j;w-1,w}^{v,v-1}) e^{-(\Delta E_i^{v-1} - \Delta E_j^{w-1})/2kT}$$

with

$$Z_{i,j} = 10^{-6} \times 400 \sigma_{i,j}^2 \sqrt{\pi kT/2\mu_{i,j}}$$

where $Z_{i,j}$ is the collision number in m^3/s and $\pi \sigma_{i,j}^2$ is the collision cross-section in cm^2 with $\sigma = 3.75 \times 10^{-8}$ cm. We also have

$$S_{i,j;w-1,w}^{v,v-1} = S_{i,j} T \frac{v}{1 - \chi_{ei} v} \cdot \frac{w}{1 - \chi_{ej} w} F(\lambda_{i,j;w-1,w}^{v,v-1})$$

and

$$L_{i,j;w-1,w}^{v,v-1} = \frac{L_{i,j}}{T} \left(\frac{g_i^{v,v-1}}{g_i^{1,0}} \right)^2 \left(\frac{g_j^{w-1,w}}{g_j^{1,0}} \right)^2 \cdot \exp \left(-\frac{(\Delta E_i^{v-1} - \Delta E_j^{w-1})^2}{b_{i,j} k^2 T} \right),$$

where $S_{i,j}$ (in K^{-1}), $L_{i,j}$ in K and $b_{i,j}$ in K are empirical parameters fitted to available experimental data. Their values are given in Table 2. Also, $F(\lambda)$ is the same as before in the case of VT transfer while the expression for λ now becomes

$$\lambda_{i,j;w-1,w}^{v,v-1} = 2^{-3/2} \sqrt{\frac{\Theta_{i,j}}{T}} \frac{|\Delta E_i^{v-1} - \Delta E_j^{w-1}|}{k\Theta_i}.$$

Finally

$$\left(\frac{g_i^{v,v-1}}{g_i^{1,0}} \right)^2 = \left(\frac{a_i + 1}{a_i + 3 - 2v} \right)^2 \cdot \frac{v(a_i + 2 - 2v)(a_i + 4 - 2v)}{a_i(a_i + 3 - v)},$$

where $a_i = 1/\chi_{ei}$.

Spontaneous Radiative Decay term

The SRD term in the species equation (4) for radiative transition between levels of the same electronic species can be written as [8]

$$SRD_{i,v} = \sum_{w=1}^{w'} \mathcal{A}_i^{v+w,v} n_{i,v+w} - \mathcal{A}_i^{v,v-w} n_{i,v}$$

where, \mathcal{A} , the Einstein A coefficients are given by

$$\frac{\mathcal{A}_i^{v,v-w}}{\mathcal{A}_i^{1,0}} = \frac{1}{(a_i - 2)(a_i - 3)} w \cdot \frac{v!}{(v-w)!} \frac{b_v(b_v + w)(b_v + 2w)}{\prod_{q=0}^{w-1} (a_i - v + q)}$$

with $b_v = a_i - 2v - 1$ and w' and $\mathcal{A}_i^{1,0}$ (in $1/s$) are given in Table 3.

References

- [1] Lichtin, D. A., Janson, S. W., Pollard, J. E., Schultess, D. R., and Cohen, R. B., "Arcjet Plume Characterization Part

- I : Mass/Velocity Analyzer Results", Paper AIAA-90-2642, Presented at the 21st International Electric Propulsion Conference, July 18-20, 1990, Orlando, Florida.
- [2] Babu, V., Aithal, S., and Subramaniam, V. V., "On the Effects of Swirl in Arcjet Thruster Flows", Paper IEPC-93-183, Presented at the 23rd International Electric Propulsion Conference, September 13-17, 1993, Seattle, Washington.
 - [3] Briley, W. R., and McDonald, H. "Solution of the Multidimensional Compressible Navier-Stokes Equations by a Generalized Implicit Method", *Journal of Computational Physics*, Vol. 24, 1977, pp. 372-397.
 - [4] Treanor, C. E., Rich, J. W. and Rehm, R.G. "Vibrational Relaxation of Anharmonic Oscillators with Exchange-Dominated Collisions", *Journal of Chemical Physics*, Vol. 48, No. 4, 1968, pp. 1798-1807.
 - [5] Nighan, W., "Electron Energy Distributions and Collision Rates in Electrically Excited N_2 , CO and CO_2 ", *Physical Review A*, Vol. 2, No. 5, 1970, pp. 1989-2000.
 - [6] Rich, J. W., and Bergman, R., " C_2 and CN Formation by Optical Pumping of CO/Ar and CO/ N_2 /Ar Mixtures at Room Temperatures", *Chemical Physics*, Vol. 44, No. 1, 1979.
 - [7] Crofton, M. W., Welle, R. P., Janson, S. W., and Cohen, R. B., "Temperature, Velocity and Density Studies in the 1 kW Ammonia Arcjet Plume by LIF", Paper AIAA-92-3241, Presented at the AIAA/SAE/ASME/ASEE 28th Joint Propulsion Conference and Exhibit, July 6-8, 1992, Nashville, Tennessee.
 - [8] Chiroux de Gavelle de Roany, A., Flament, C., Rich, J. W., Subramaniam, V., and Warren, W. R. "Strong Vibrational Nonequilibrium in Supersonic Nozzle Flows", *AIAA Journal*, Vol. 31, No. 1, 1993, pp. 119-128.
 - [9] Hindmarsh, A. C., "LSODE and LSODI, Two Initial Value Ordinary Differential Equation Solvers", *ACM SIGNUM Newsletter*, Vol. 15, 1980, pp. 10-11.
 - [10] Rhodes, R., and Keefer, D., "Numerical Modeling of an Arcjet Thruster", paper AIAA-90-2614, presented at the 21st International Electric Propulsion Conference, July 18-20, 1990, Orlando, Florida.
 - [11] Rhodes, R., and Keefer, D., "Comparison of Model Calculations with Experimental Data From Hydrogen Arcjets", paper IEPC-91-111, presented at the 22nd International Electric Propulsion Conference, October 14-17, 1991, Viareggio, Italy.
 - [12] King, D. Q., and Butler, G. W., "Modeling and Measurement of N_2 Arcjet Performance", paper AIAA-90-2616 presented at the 21st International Electric Propulsion Conference, July 18-20, 1990, Orlando, Florida.
 - [13] Butler, G. W., Kashiwa, B. A., King, D. Q., "Numerical Modeling of Arcjet Performance", paper AIAA-90-1474 presented at the AIAA 21st Fluid Dynamics, Plasma Dynamics, and Lasers Conference, June 18-20, 1990, Seattle, Washington.
 - [14] Miller, S. A., and Martinez-Sanchez, M., "Multifluid Nonequilibrium Simulation of Electrothermal Arc-jets", paper AIAA-93-2101, presented at the AIAA/SAE/ASME/ASEE 29th Joint Propulsion Conference and Exhibit, June 28-30, 1993, Monterey, California.

- [15] Krier, H., and Burton, R., AFOSR Contractors Meeting, Atlantic City, New Jersey, June, 1993.
- [16] Okamoto, H., Nishida, M., and Tanaka, K., "Numerical Studies of the Flow Field in a Low Power DC Arcjet Thruster Using Navier-Stokes Equations", Paper IEPC-91-112, Presented at the 22nd International Electric Propulsion Conference, October 14-17, 1991, Viareggio, Italy.
- [17] Glocker, B., Schrade, H. O., and Sleziona, P. C., "Numerical Prediction of Arcjet Performance", Paper AIAA-90-2612, 21st International Electric Propulsion Conference, 1990, Orlando, Florida.
- [18] Dunnwald, H., Siegel, E., Urban, W., Rich, J. W., Homicz, G. F., Williams, M. J., "Anharmonic Vibration-Vibration Pumping in Nitric Oxide by Resonant IR-Laser Irradiation", *Chemical Physics*, Vol. 94, 1985, pp. 195-213.
- [19] Vincenti, W. G and Kruger, C. H., *Introduction to Physical Gas Dynamics*, John Wiley & Sons, New York, 1965.
- [20] Anderson, D. A, Tannehill, J. C and Pletcher, R. H. *Computational Fluid Mechanics and Heat Transfer*, Hemisphere Publishing Corporation, McGraw-Hill Book Company, New York, 1984.
- [21] Isaacson, E and Keller, H. B. *Analysis of Numerical Methods*, Wiley, New York, 1966.
- [22] Huber, K. P., and Herzburg, G., *Molecular Spectra and Molecular Structure, Vol. 4, Constants of Diatomic Molecules*, Van Nostrand Reinhold, New York, 1978.
- [23] Yardley, J. T., *Introduction to Molecular Energy Transfer*, Academic, New York, 1980.
- [24] Flament, C., George, T., Meister, K. A., Tufts, J. C., Rich, J. W., Subramaniam, V. V., Martin, J. P., Piar, B., and Perrin, M. Y., "Nonequilibrium vibrational kinetics of carbon monoxide at high translational mode temperatures", *Chemical Physics*, Vol. 163, 1992, pp. 241-262.
- [25] Poulsen, L. L., and Billing, G. D., "Vibrational Deactivation of CO($v=1$) by $p-H_2$. The Importance of Higher-order Multipole Moments", *Chemical Physics*, Vol. 89, No. 2, 1984, pp. 219-222.

TABLE 1.

VT					
Species	$A_{i,j}$	$B_{i,j}^* (K^{1/3})$	$C_{i,j}^* (K^{2/3})$	$\Theta_{i,j}^*/\Theta_i^{*2} (K^{-1})$	Ref.
CO-CO	-15.23	280.5	-549.6	45.6×10^{-2}	[24]
CO-Ar	10.38	0.0	0.0	53.72×10^{-2}	[24]
CO- H_2	-26.22	-10.61	-12.80	6.089×10^{-2}	[25]
N_2 - H_2	-26.22	-10.61	-12.80	6.089×10^{-2}	[25]
CO- N_2	-7.934	147.7	0.0	45.6×10^{-2}	[8]
N_2 - N_2	-12.539	258.9	-390.9	45.6×10^{-2}	[8]
N_2 -Ar	-15.62	168.95	0.0	53.72×10^{-2}	[8]

TABLE 2.

VV				
Species	$S_{i,j}^* (K^{-1})$	$\mathcal{L}_{i,j}^* (K)$	$b_{i,j}^* (K)$	Ref.
CO-CO	1.64×10^{-6}	1.6142	40.36	[23]
CO- N_2	7.006×10^{-8}	1.897×10^{-2}	191.42	[8]
N_2 - N_2	9.37×10^{-8}	0.0	-	[8]

TABLE 3.

SRD			
Species	w'	$A^{*1.0}$ (1/s)	Ref.
CO-CO	4	30.3	[23]
N_2-N_2	-	0.0	[8]

TABLE 4.

Spectroscopic Constants				
Species	ω_{ei} (cm^{-1})	$\omega_{ei}\chi_{ei}$ (cm^{-1})	Θ_i^* (K)	Ref.
CO-CO	2169.8	13.288	3121.0	[22]
N_2-N_2	2358.6	14.324	3396.8	[22]

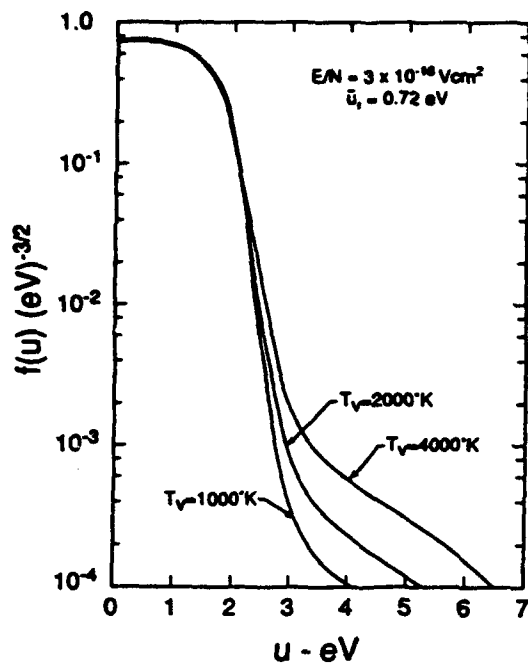


Fig. 1: Electron Energy Distribution Functions (EEDFs) for an electric discharge in nitrogen (from ref.[5]). A Maxwellian distribution would appear linear on this plot.

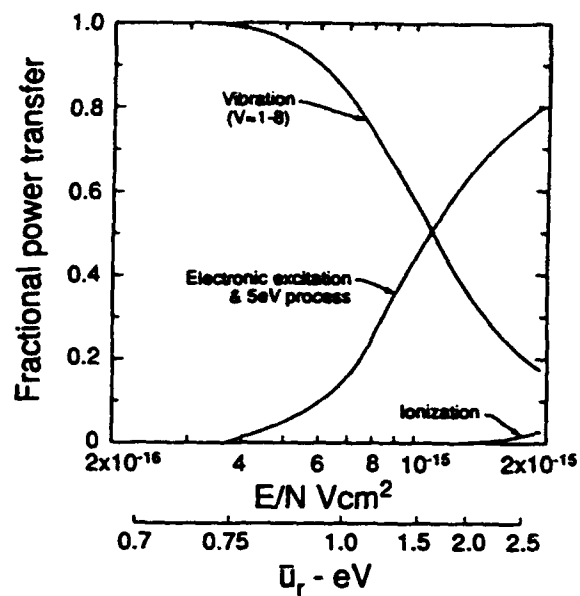


Fig. 2: Normalized fractional power is shown here versus E/N for an electric discharge in nitrogen (from ref.[5]).

30-kW Arcjet Geometry

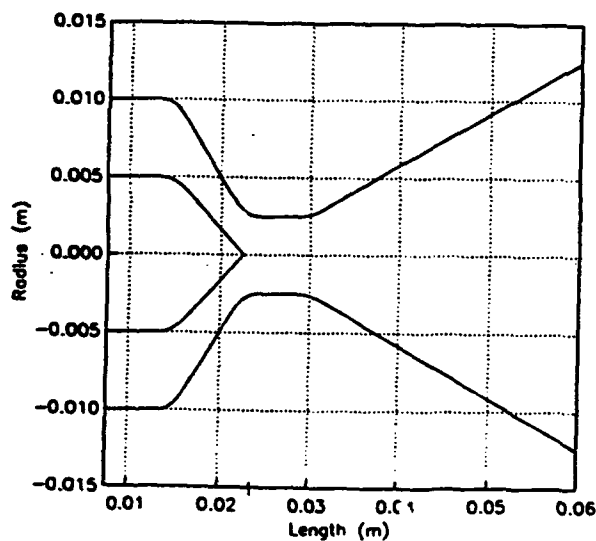


Fig. 3: Schematic of the 30 kW arcjet geometry used in the quasi 1-D calculations.

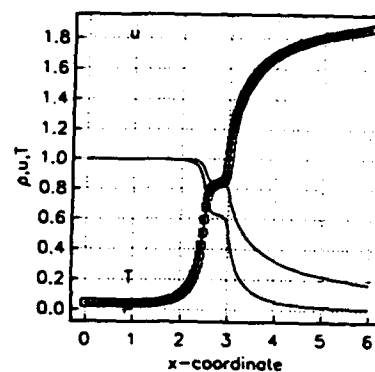


Fig. 4: Profiles of mass density (normalized by 0.1365 Kg/m^3), temperature (normalized by 5000 K), and axial velocity (normalized by 1442 m/s) are shown here versus the streamwise coordinate (normalized by 0.01 m).

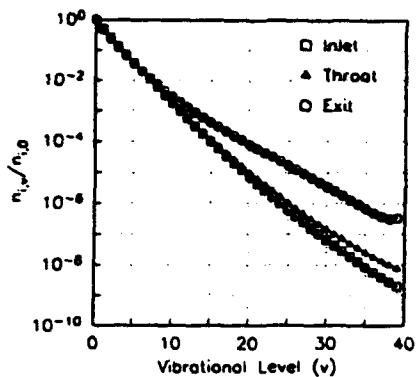


Fig. 5: Populations of vibrationally excited nitrogen molecules normalized by the ground vibrational populations at the respective locations is shown here versus vibrational quantum number v . This is for flow of pure N_2 .

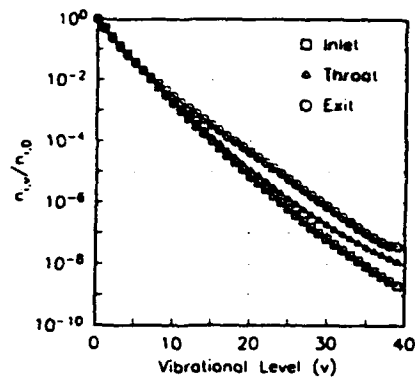


Fig. 6: Populations of vibrationally excited nitrogen molecules normalized by the ground vibrational populations at the respective locations is shown here versus vibrational quantum number v . This is for flow of N_2/Ar .

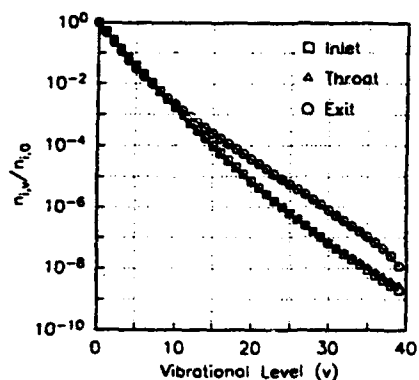


Fig. 7: Populations of vibrationally excited nitrogen molecules normalized by the ground vibrational populations at the respective locations is shown here versus vibrational quantum number v . This is for flow of N_2/H_2 .

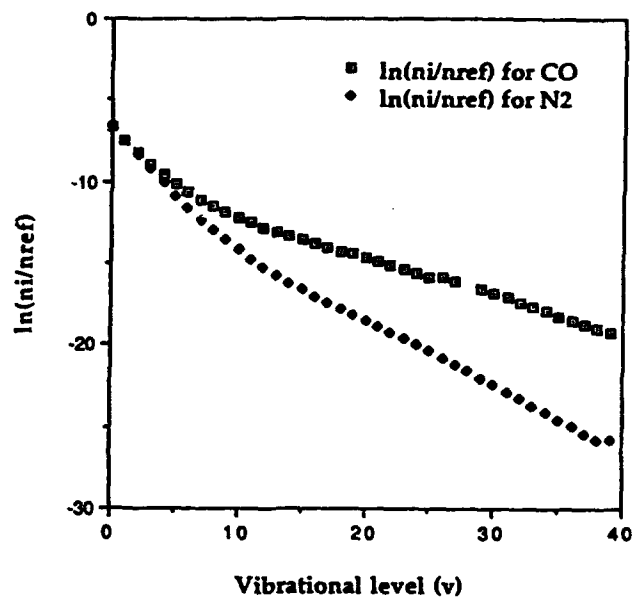


Fig. 8: Populations of vibrationally excited nitrogen molecules normalized by the ground vibrational populations at the respective locations is shown here versus vibrational quantum number v . This is for flow of $N_2/CO/Ar$.

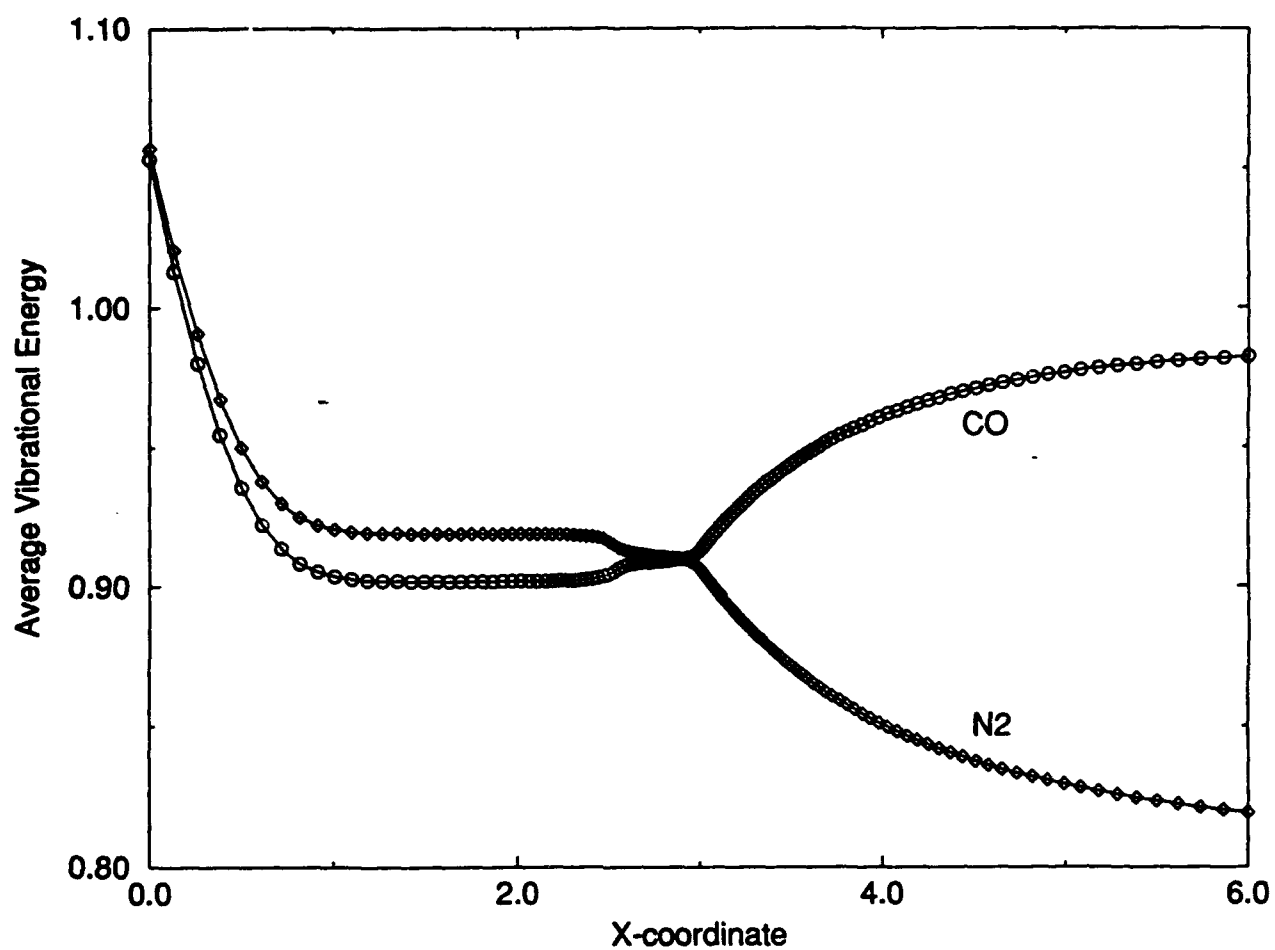


Fig. 9: The average vibrational energy per particle (normalized by 6.903×10^{-20} J) is plotted here versus streamwise coordinate (normalized by 0.01 m) for flow of $N_2/CO/Ar$. Note how the nitrogen up-pumps the CO via vibrational energy transfer and is de-excited in the process.

APPENDIX C

IEPC-93-183

ON THE EFFECTS OF SWIRL IN ARCJET THRUSTER FLOWS

V. BABU, S. AITHAL, AND V. V. SUBRAMANIAM

Department of Mechanical Engineering
The Ohio State University
Columbus, Ohio 43210

23rd International Electric Propulsion
Conference

September 13-17, 1993 / Seattle, Washington

ABSTRACT

Swirl has long been thought to be necessary to sustain arcs in high-speed flows. In this paper, we explore the effect of injected swirl on both the cold flow (i.e. non-ionized and non-reacting) and the plasma flow in arcjet thrusters. The fully implicit Linearized Block Implicit (LBI) scheme of Briley & McDonald[1] is used to develop highly accurate solutions to internal, viscous, supersonic flows of the type encountered in arcjet thrusters. In the case of cold flow, it is found that the injected swirl persists downstream for low mass flow rates (on the order of mg/s) and is actually enhanced at the constrictor entrance, near the cathode tip. However, for higher mass flow rates (on the order of g/s), the injected swirl is overcome by the torque due to viscous forces (both in the flow as well as at the walls) and fails to persist far enough downstream. Consequently, swirl stabilization of the flow in arcjets can only succeed under certain operating conditions. The actual plasma flow is also investigated in the presence of swirl, but our present simulations show continuous decay of injected swirl. As we show in this paper, this is an artefact and limitation of our present simulation. Real arcjet flows should experience the effects we observe in our cold flow simulations. This effect has important ramifications for the design and locations of the swirl injectors and overall arcjet performance. On-going improvements to our simulation to rectify this problem are discussed.

Nomenclature

B_θ	magnetic induction (T)
e	internal energy per unit volume (J/m^3)
j_r	radial component of current density (A/m^2)
j_z	axial component of current density (A/m^2)
k	thermal conductivity ($\text{W}/\text{m}^2 \text{ K}$)

k_B	Boltzmann's constant (J/K)
m_a	mass of an argon atom (kg)
n_a	number density of atoms (particle / m^3)
n_e	number density of electrons (particle / m^3)
p	pressure (N/m^2)
r	radial coordinate (m)
t	time (s)
T	temperature (K)
u	radial velocity (m/s)
v	swirl velocity (m/s)
w	axial velocity (m/s)
z	axial coordinate (m)
ϵ_i	ionization potential (J)
μ	coefficient of viscosity (Ns/m^2)
μ_0	permeability of free space (Tm/A)
ρ	mass density (kg/m^3)
ψ	magnetic stream function (Tm)
σ	electrical conductivity (mho/m)

1 Introduction

Despite the near flight-readiness of arcjet thrusters, the plasma flow in these devices is only beginning to be understood. Unlike its distant cousin, the Magnetoplasma-dynamic (MPD) thruster, the arcjet is basically an electrothermal device. The propellant (either monatomic or molecular) stream is heated by an electric arc and expanded through a converging-diverging nozzle to supersonic speeds. Although the device is simple in structure, the phenomena that govern flow in the device are quite complicated and are yet to be deciphered. Among these is the question of whether or not injected swirl is necessary for effective operation, and whether this swirl plays any role in arcjet fluid dynamics in the first place. Swirl in the flow-field forms the central focus of this paper.

The compressible Navier-Stokes equations

govern the physics of flow fields in arcjets. These flows are often times further complicated by the effects of departure from thermodynamic equilibrium of the internal modes of molecular motion. This disequilibrium between internal modes (vibration, rotation and electronic excitation) and external modes i.e. translational molecular motions gives rise to complicated chemistry. Many numerical methods have been devised to solve the compressible, Navier-Stokes equations, the most popular of these being the MacCormack scheme [2], the Beam-Warming scheme [3] and the Linearized Block Implicit (LBI) scheme of Briley & McDonald [1]. Our ultimate aim is to study arcjet flows including the effects of finite-rate chemistry and internal mode disequilibrium. We have chosen the LBI method for this purpose. This method has the advantages of being able to handle large numbers of species as well as being extendable from quasi-1D through 2-D, to fully 3-D with relative ease.

Recently, several groups have begun numerical simulations of arcjet flows [4, 5, 6, 7, 8, 9, 10]. Perhaps the earliest of these simulations were those of Keefer et. al. [4] and Butler et. al. [6, 7]. Both groups have identified σ , the electrical conductivity, as the single most important property that governs arcjet flow. This is because σ varies by orders of magnitude between regions in the arc and regions near the colder electrode boundaries. σ determines the current distribution in the gas, and hence the ohmic heating. The Ohmic heating in turn determines temperatures and ionization fraction. The latter has a profound influence on other properties, most notably the viscosity [11] so that the device performance is inevitably altered. Furthermore, the distribution of σ profoundly affects the heat addition not only in the subsonic portion of the flow but also in the supersonic portion. Although the latter is unavoidable, it is important to minimize heating the supersonic flow as specific impulse will suffer. In

addition, no existing work has systematically examined the effects of injected swirl on the flow-field or conductivity distribution in arcjets.

In this paper, we systematically examine the effects of injected swirl using an axis-symmetric 2-D model of a nominal 30 KW arcjet. Both cold-flow and flow including the arc are examined. We find that the key to obtaining solutions to these flows is the proper modelling of the boundary conditions and specification of the proper initial conditions so that the flow can accelerate smoothly from subsonic to supersonic speeds.

This paper is organized as follows. The governing equations and boundary conditions are presented first, followed by the numerical method. As brief illustration of code verification, sample solutions comparing against experiments solutions are presented for a converging-diverging nozzle similar but not identical to the nominal 30 KW arcjet geometry. Cold-flow and 2-D axisymmetric arcjet solutions with and without swirl are discussed next, followed by a summary and conclusions of this work.

2 Formulation

The equations that govern the cold (i.e. non-reacting) viscous, supersonic flow are the compressible Navier-Stokes equations. For the arcjet, these equations become considerably more complicated by the presence of a body force, heat generation, species diffusion, chemical reaction, ionization and recombination, and variable properties. However in this paper, we concern ourselves only with a monatomic propellant (Argon) and defer consideration of molecular propellants in a companion paper [12]. We further neglect species diffusion terms, assume quasi-neutrality, and take the electron and heavy-particle temperatures to be equal.

While significant departures from the latter are known to occur in the colder regions of the flow[11], we are mainly interested here in the flow away from the electrode-adjacent regions. The governing equations in cylindrical polar coordinates form are:

$$\frac{\partial \rho}{\partial t} + \frac{1}{r} \frac{\partial(r\rho u)}{\partial r} + \frac{\partial(\rho w)}{\partial z} = 0, \quad (1)$$

$$\begin{aligned} & \frac{\partial(\rho u)}{\partial t} + \frac{1}{r} \frac{\partial(r\rho u^2)}{\partial r} + \frac{\partial(\rho uw)}{\partial z} - \frac{\rho v^2}{r} \\ &= -\frac{\partial p}{\partial r} + \mu \left[\frac{\partial^2 u}{\partial r^2} + \frac{1}{r} \frac{\partial u}{\partial r} + \frac{\partial^2 u}{\partial z^2} - \frac{u}{r^2} \right] \\ &+ \frac{\mu}{3} \frac{\partial}{\partial r} (\nabla \cdot \vec{u}) + \frac{\partial \mu}{\partial r} \left[\frac{4}{3} \frac{\partial u}{\partial r} - \frac{2}{3} \frac{u}{r} - \frac{2}{3} \frac{\partial w}{\partial z} \right] \\ &+ \frac{\partial \mu}{\partial z} \left[\frac{\partial u}{\partial z} + \frac{\partial w}{\partial r} \right] - j_z B_\theta, \end{aligned} \quad (2)$$

$$\begin{aligned} & \frac{\partial(\rho v)}{\partial t} + \frac{1}{r} \frac{\partial(r\rho uv)}{\partial r} + \frac{\partial(\rho vw)}{\partial z} + \frac{\rho uv}{r} \\ &= \mu \left[\frac{\partial^2 v}{\partial r^2} + \frac{1}{r} \frac{\partial v}{\partial r} + \frac{\partial^2 v}{\partial z^2} - \frac{v}{r^2} \right] \\ &+ \frac{\partial \mu}{\partial r} \left[\frac{\partial v}{\partial r} - \frac{v}{r} \right] + \frac{\partial \mu}{\partial z} \frac{\partial v}{\partial z}, \end{aligned} \quad (3)$$

$$\begin{aligned} & \frac{\partial(\rho w)}{\partial t} + \frac{1}{r} \frac{\partial(r\rho uw)}{\partial r} + \frac{\partial(\rho w^2)}{\partial z} \\ &= -\frac{\partial p}{\partial z} + \mu \left[\frac{\partial^2 w}{\partial r^2} + \frac{1}{r} \frac{\partial w}{\partial r} + \frac{\partial^2 w}{\partial z^2} \right] \\ &+ \frac{\mu}{3} \frac{\partial}{\partial z} (\nabla \cdot \vec{u}) + \frac{\partial \mu}{\partial r} \left(\frac{\partial u}{\partial z} - \frac{w}{r} \right) \\ &- \frac{\partial \mu}{\partial z} \left(-\frac{2}{3} \frac{\partial u}{\partial r} - \frac{2}{3} \frac{u}{r} + \frac{4}{3} \frac{\partial w}{\partial z} \right) + j_r B_\theta, \end{aligned} \quad (4)$$

$$\begin{aligned} & \frac{\partial}{\partial t} \left[e + \rho \frac{u^2 + v^2 + w^2}{2} \right] \\ &+ \frac{1}{r} \frac{\partial}{\partial r} \left[e + p + \rho \frac{u^2 + v^2 + w^2}{2} \right] \end{aligned}$$

$$\begin{aligned} & + \frac{\partial}{\partial z} \left[e + p + \rho \frac{u^2 + v^2 + w^2}{2} \right] \\ &= \frac{1}{r} \frac{\partial}{\partial r} \left(k \frac{\partial T}{\partial r} \right) + \frac{\partial}{\partial z} \left(k \frac{\partial T}{\partial z} \right) \\ &+ \mu \Phi + \frac{j_r^2 + j_z^2}{\sigma} + j_r w B_\theta - j_z u B_\theta, \end{aligned} \quad (5)$$

where, Φ is the dissipation function given by,

$$\begin{aligned} \Phi = 2 & \left[\left(\frac{\partial u}{\partial r} \right)^2 + \left(\frac{u}{r} \right)^2 + \left(\frac{\partial w}{\partial z} \right)^2 \right] \\ &+ \left(\frac{\partial v}{\partial z} \right)^2 + \left(\frac{\partial u}{\partial z} + \frac{\partial w}{\partial r} \right)^2 \\ &+ \left(\frac{\partial v}{\partial r} - \frac{v}{r} \right)^2 - \frac{2}{3} \left(\frac{\partial u}{\partial r} + \frac{u}{r} + \frac{\partial w}{\partial z} \right)^2, \end{aligned}$$

and e is the internal energy per unit volume given by:

$$e = \frac{3}{2} (2n_e + n_a) k_B T + n_e \epsilon_i, \quad (6)$$

and the p is the pressure given by:

$$p = (2n_e + n_a) k_B T \quad (7)$$

In the above equations,

$$\nabla \cdot \vec{A} = \frac{e_r}{r} \frac{\partial}{\partial r} (r A_r) + e_z \frac{\partial A_z}{\partial z},$$

and

$$\nabla^2 \phi = \frac{\partial^2 \phi}{\partial r^2} + \frac{1}{r} \frac{\partial \phi}{\partial r} + \frac{\partial^2 \phi}{\partial z^2},$$

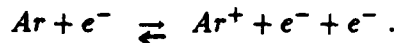
where, $\vec{A} = A_r \hat{e}_r + A_\theta \hat{e}_\theta + A_z \hat{e}_z$ is any vector and ϕ is a scalar.

In addition, we have the following species rate and magnetic diffusion equations:

$$\begin{aligned} & \frac{\partial n_e}{\partial t} + \frac{1}{r} \frac{\partial}{\partial r} (n_e u) + \frac{\partial}{\partial z} (n_e w), \\ &= k_f n_e n_a - k_r n_e^3 \end{aligned} \quad (8)$$

$$\nabla \times (\nabla \times \bar{\psi}/r) - \frac{\nabla \sigma}{\sigma} \times (\nabla \times \bar{\psi}/r) - \mu_0 \sigma (\nabla \times (\bar{u} \times \bar{\psi}/r)) = 0. \quad (9)$$

The thermal conductivity, coefficient of viscosity, and electrical conductivity are computed from mean free path theory and are given by [13]. Here k_f and k_r are the forward and reverse rates [11] of the reaction



The mass density ρ in the above equations is related to the number densities as follows :

$$\rho = m_a(n_e + n_a) \quad (10)$$

where m_a is the mass of a neutral atom.

2.1 Boundary Conditions

Boundary conditions for the eight dependent variables ($\rho, u, v, w, p, \psi, n_e, T$) need to be specified along the inlet and exit boundaries, on the wall, and along the centerline of the nozzle geometry.

No-slip conditions are imposed on all solid boundaries. In the case of the ionizing arcjet flows, the temperature at the anode is held constant at 1500 K, while the cathode temperature is held at 1000 K along its straight portion and ramped linearly to 2000 K along its sloping face up to the tip. The mass density at the wall is obtained by applying the radial component of the momentum equation on the wall. The choice of the radial component instead of the normal component is dictated by the need for simplicity. The electron number density on the wall is obtained by setting its radial derivative to zero there.

Symmetry conditions are imposed along the centerline for all the variables except the swirl and radial components of velocity v and u , which are set equal to zero, identically.

Prescribing boundary conditions at the inlet and exit planes of the nozzle depends on whether the flow is subsonic or supersonic. All the solutions presented here consider subsonic inlets. Hence, following Briley & McDonald [1], the stagnation temperature and stagnation pressure at the inlet are specified. In addition, at the inlet, the radial component of velocity is set to zero and the swirl component of velocity is either zero or set to some prescribed distribution corresponding to injection. It is important to note here that the axial component of velocity which determines the mass flow rate through the nozzle, is not specified at the inlet but is determined from an implicit extrapolation of the interior values, as is n_e . In addition, the mass density at inlet is determined by using the isentropic relation between the stagnation and static pressures and temperatures there.

Along the exit plane, the flow is subsonic-supersonic. All the variables (including n_e) except mass density on the exit plane are evaluated by implicit extrapolation from the interior [1]. If the local Mach number M defined as w/a , where $a^2 = \frac{5}{3}(1 + \frac{n_e}{n_e + n_a})k_B T/m_a$ is the frozen speed of sound is greater than one at a point on the exit plane, then the mass density is also evaluated by extrapolation. If, on the other hand, $M < 1$ at some point on the exit plane, then the exit static pressure is specified and the mass density is evaluated from the equation of state. The correct value of the exit static pressure would usually not be known, unless the plume is modelled as well. Care must be exercised in choosing a value for the exit static pressure, for, if it is too high, the boundary layer on the wall in the diverging section of the nozzle can separate. This is an important detail that often escapes mention in the literature.

The boundary conditions on ψ could use improvement. In this work, we prescribe and hold ψ fixed at a certain value based on the total current [4] on the anode wall from the inlet until the exit to the constrictor. Beyond this point,

ψ is varied linearly along the anode wall to zero at the exit. ψ is taken to be identically zero at the exit plane and at the centerline (i.e. $r=0$). Along the inlet plane, ψ is varied linearly from its value on the anode wall to 0.99 times that value, and maintained at that value along the straight portion of the cathode as well as on the sloping face of the cathode until 5 grid points from the tip. For these 5 grid points near the cathode tip, ψ is decreased linearly from 0.99 times the maximum value to zero in order to force most of the current contours to approach the cathode axially.

2.2 Initial Conditions

Due to the wave nature of the governing equations, initial conditions must be prescribed with care. In general, arbitrary initial values for the dependent variables will not yield stable solutions for any numerical method. Furthermore, since it is impossible to simulate the breakdown process that initiates the discharge n_e cannot be expected to start from 0 (i.e. completely non-ionized state). In this work, we prescribe an upstream stagnation temperature (also equal to the reference temperature used for non-dimensionalization) of 10,000 K, an upstream stagnation pressure (which depends on the desired mass flow rate), $u = 0$, $v = 0$ (except at the inlet, if swirl is injected), $w = 0.1a_0$ where a_0 is the frozen speed of sound evaluated at the inlet stagnation temperature, and $n_e = 0.1n_{ref}$ where n_{ref} is computed from the stagnation pressure and stagnation temperature.

It is evident at the outset that an unrealistically high value must be prescribed for the initial stagnation temperature and electron number density. This is a drawback of the present formulation. It suffices to state at this time that for supersonic flows of the type encountered in arcjets, the upstream inlet static pressure, temperature, and densities

must adjust themselves in order to accommodate the presence of the arc downstream. In other words, some level of ionization (and temperature commensurate with this initial value of ionization) must be prescribed to start the calculation. Obviously, the final converged steady state solutions must be independent of the initial value chosen for n_e . In this work, we use a simple way to calculate the static temperature at the inlet from the stagnation temperature. As a result of this simplicity, our inlet temperatures must be necessarily high in order to conserve overall energy in the converged state. Physically, this alludes to the fact that some concentrated region of Ohmic heating must exist upstream of the constrictor that pre-ionizes the gas before it enters the main arc region.

3 Numerical Method

Equations (1)-(5),(8) are solved on a non-staggered non-uniform grid. This grid in the physical domain is transformed into a uniform grid in a computational domain using an analytical coordinate transformation. The transformation is such that the nozzle contour is transformed into a rectangle in the computational domain [14, section 5-6.1]. The governing equations together with boundary conditions are transformed to the computational domain and solved there.

The transformed forms of the governing equations (except for the magnetic diffusion equation) are solved using the LBI scheme of Briley & McDonald [1]. Since all the details of the scheme have already been reported elsewhere [1], they will not be given here. At each time step in the time-marching sequence, the magnetic diffusion equation is solved using odd-even point SOR with the relaxation factor ω set to 1.0. Thus, the ψ field is solved for independently at each time step. The other coupled, linear algebraic equations resulting from

the other governing equations are then solved by using the Douglas-Gunn ADI method. The ADI method itself involves the solution of block tridiagonal systems in each coordinate direction, with block size equal to the number of dependent variables, which, in our case is eight. These systems can be solved using existing efficient LU decomposition methods [15]. Following Briley & McDonald [1], we add dissipation in the form a second derivative in the axial coordinate to the unsteady governing equations.

4 Cold Flow

4.1 C-D Nozzle

In this section, we present viscous 2-D axisymmetric solutions for flow in a C-D nozzle. These are for cold-flow (i.e. non-reacting and non-ionizing) of air ($\gamma = 1.4, \mu = 18 \times 10^{-6} \text{ N s/m}^2, Pr = 0.701$) and are presented for the purposes of code verification. The nozzle geometry is identical to the geometry of the 30 kW Arcjet thruster (shown in Fig. 1) but without the inlet plenum and the constrictor. The transition from the converging to the diverging section is achieved within five grid points through the use of a quadratically varying profile for the outer radius. The exit to throat area ratio for this nozzle geometry is 25. Solutions presented here are obtained on a non-uniform grid with 256 points in the axial direction and 64 points in the radial direction. The most interesting feature of this flow is the presence of weak compression waves in the diverging section. Profiles of Mach number along the radial grid lines $j = 0$ and $j = 38$ are shown in Fig. 2 together with the Mach number profile from the corresponding frictionless, quasi 1-D solution. Here, the grid line corresponding to $j = 0$ represents the centerline. The profile along the $j = 38$ grid line is closest to the quasi 1-D profile. The maximum exit Mach number in the viscous case is about 4.6, which is less

than the value of about 5.0 for the frictionless, quasi 1-D case. The profile along the centerline shows a sharp drop in the Mach number near a dimensionless axial coordinate of 8. One can see from the Mach number contours in Fig. 3, a change in the shapes of these contours near the same axial location ($z = 8$). In this figure, the sonic line ($M=1$) is shown as the thick line. The radial Mach number profiles have their maxima located on the centerline up until $z = 8$ and these maxima move to a location near the center of the channel once we cross this particular axial location. These contours look very similar to those obtained using the method of characteristics [16] for inviscid flow in a similar geometry. They also agree very well qualitatively with the experimental results presented in [17]. It was first shown by Darwell & Badham [16] that compression waves could be generated in C-D nozzle geometries from the location where the curved throat section meets the diverging conical section, if the radius of curvature of the nozzle wall profile is discontinuous at this location. These compression waves can coalesce at the centerline at a point downstream to form a weak oblique shock. Experiments conducted subsequently by Back et al. [18, 19] and Cuffel et al. [17] showed this to be indeed true. The sharp drop in the Mach number along the centerline in Fig. 2 is due the oblique shocks intersecting the centerline and the change in the shapes of the Mach number contours mentioned before is due to these incoming and reflected weak oblique shock waves. Further evidence of these waves can be seen in Fig. 4, where a plot of the radial velocity along the grid line $j = 8$. The radial velocity is negative in the converging section and then it rapidly turns around at the throat becoming positive in the diverging section. The radial velocity then decreases sharply in the neighbourhood of $z = 8$ and becomes negative as the flow traverses the incident oblique shock waves. The fluid is turned in a clockwise direction towards the centerline by

these waves, since they are right running. The radial velocity then increases just as rapidly, as the flow traverses the oblique shocks that are reflected from the centerline. These turn the fluid in an anti-clockwise direction away from the centerline, being left running waves. The radial velocity settles down to a constant value after about $z = 14$. The overturning of the fluid as it goes through the throat is evident from this figure when one compares the value of the radial velocity near $z \approx 7$ with the final value for $z > 14$.

The exact mechanism by which these compression waves are generated is discussed in detail in [16, 19]. As the flow passes through the throat, the regions of the flow close to the wall are overturned so as to be parallel to the wall. Consequently, when the location where the discontinuous change in wall curvature occurs is reached, the flow must be turned back towards the centerline, i.e. away from the wall. This can only occur through a series of compression waves.

It is likely that such compression waves are generated in the constrictor region of the arcjet. Depending on the physical shape of the arc, it is possible that flow turning such as the type just discussed occur at the constrictor exit. Another way this effect can happen in arcjets is via actual changes in the contour of the nozzle (anode) wall due to electrode erosion. The amount of erosion needed to trigger such compression waves is rather small. Very subtle changes in the geometry can trigger these compression waves. When a discharge is first struck, the arc attaches either inside the constrictor or just at the exit of the constrictor. As the supersonic flow becomes established and steady state conditions are reached, the arc attachment on the anode shifts in the downstream direction. This shifting of the anode arc attachment is in reality accompanied by erosion. Generation of such compression waves with possible coalescence downstream into in-

tersecting weak oblique shocks has very important consequences for any experimental measurements that are made at the exit plane.

4.2 30 kW Arcjet Geometry

Cold flow calculations similar to those described in the previous section, have been performed for the 30 KW arcjet geometry. No evidence of compression waves is seen in this geometry for the case of cold flow. However, the introduction of swirl at the inlet to the thruster leads to some interesting results. The profile of the inlet swirl velocity that we use is such that it is peaked very close to the anode wall, typically within 5 grid points (see Fig. 5). This type of swirl will be observed, for example, if the fluid were injected through ports peripheral to the anode wall. Shown in Figs. 6 and 7 are the contours of swirl velocities for mass flow rates of the order of a few grams per sec and a few milligrams per second respectively. It can be seen that the introduced swirl is dissipated in the former while it is enhanced to values higher than the inlet values for the latter case. We find that for the swirl to enhance in the case of higher mass flow rates, the plenum should be shorter.

The phenomena governing the enhancement or decay of swirl can be explained from simple considerations of conservation of angular momentum. Injection of swirl at the inlet represents an influx of angular momentum. Thus for any station downstream, the efflux of angular momentum will equal this influx minus the total torque due to viscous forces. If this torque is sufficient to overcome the influx of angular momentum, then the injected swirl decays in the upstream plenum region itself. However, if this torque is smaller than the influx of angular momentum, then the swirl will decrease but can persist until the beginning of the converging section. Once this converging section is reached, the decreasing area can if the condi-

tions are right, lead to an increase in the swirl component of the velocity from overall conservation of angular momentum. The total torque is composed of two quantities. The first is the torque due to the wall shear stresses (at anode and cathode), and the second is the torque due to the shear stress integrated across the flow volume between cathode and anode. Of these, the torque due to the wall shear at the anode is the most important.

The critical parameter which determines whether or not the swirl persists and is amplified, is the propellant mass flow rate. At higher mass flow rates (and hence higher Reynolds numbers), the boundary layers are closer to the walls so that the wall shear stresses are high. Consequently, the torque due to viscous forces can overcome the influx of angular momentum and the swirl will perish long before it reaches the cathode tip. In contrast, at the lower mass flow rates (or lower Reynolds numbers), the boundary layers are thicker so that wall shear stresses are smaller leading to reduced torque due to viscous forces. Therefore, *regardless of the magnitude of the viscosity there is some limiting mass flow rate beyond which the injected swirl will decay.* Obviously, the higher the viscosity the smaller the limiting mass flow rate. Thus, this mechanism for swirl enhancement can indeed be operative at higher temperatures. *The mass flow rate and inlet plenum length are thus key design parameters.*

5 Arcjet Flow

In this section, we present results for a 30 kW arcjet geometry, current of 50 A, argon mass flow rate of 100 mg/s. We wish to illustrate the solutions to the one temperature model described in sections 2 and 3. We emphasize at the outset that no "limits" or "floors" are applied to the electrical conductivity as in [7, 6]. The inlet stagnation temperature is 10000 K

and the inlet stagnation pressure is 10^4 Pa. The initial current distribution is as shown in Fig. 8. A non-dimensional time step of 10^{-3} (dimensional value is 5×10^{-9}) is used and convergence to at least three decimal places is achieved after 2500 time steps. The CPU time on the Cray Y-MP was 10 minutes.

Two cases were considered, one without swirl and one with the inlet swirl profile as shown in Fig. 5. Figs. 9 through 18, summarize the results obtained after convergence. It can be seen from Fig. 9 that the current contours have shifted downstream compared to the initially prescribed contours. This shift is caused by the varying conductivity as the supersonic flow becomes established. This reflects reality quite well as when the arc is first struck, it is usually just downstream of the constrictor exit on the anode. As the steady supersonic conditions are reached, the anode attachment moves downstream. The density of current contours near $r=0$ suggests that the current densities and hence ohmic heating are highest in that region. As expected the temperature and electron number density contours follow this very well as can be seen from Figs. 11 and 12. The calculated temperatures upstream of the cathode tip are in our opinion unrealistically high. This is an inevitable consequence of having to prescribe a high inlet stagnation temperature in order to enable the gas to ionize. This is an artifact of our simulation and caused by the non-conservative treatment of the ohmic heating term in the energy equation. We are at present pursuing a conservative treatment of the ohmic heating term which should yield much lower temperatures in the inlet plenum section. The maximum temperature is 33000 K and occurs just downstream of the cathode as can be seen from Fig. 11.

Close examination of the Mach contours in Fig. 10 and the Mach profiles in Fig. 14, reveal that the flow reached supersonic speeds in the nozzle and becomes subsonic by the time

the exit plane is reached. Heat addition to a supersonic flow is well known to slow it down. Examination of Figs. 10 and 14 shows some similarity to the cold flow solutions obtained for the C-D nozzle (see Figs. 2 and 3). The successive bumps in the Mach profiles of Fig. 14 suggests the generation of weak compression waves which coalesce at the centerline forming an oblique shock. This complex series of oblique shocks then reflect and exit the domain via the exit plane. The generation of such compression waves is due to the fact that once supersonic, the flow at the exit of the constrictor and beyond is forced to turn direction due to variations in ohmic heating and transport properties. Turning of supersonic flows as is well known is always accompanied by generation of oblique shocks or expansion fans.

Contours of pressure are shown in Fig. 13 and exhibit a decrease only until approximately midway in the nozzle. Although not shown in the figure, the pressure exhibits an increase near the exit plane indicating the passage of the flow through an oblique shock. Note the differences in the contours due different boundary conditions used here vs. [5]. Fig. 16 shows voltage as a function of streamwise distance. The power expended in the discharge is approximately 1 kW. Fig. 17 shows contours of swirl velocity indicating that the swirl decays and fails to survive for this case. The swirl is attenuated because the torque due to the shear stress at the anode is large. This is an artifact of our abnormally high inlet values of static temperature (approximately 10000 K) and ionization fractions (approximately 0.01). Elimination of the inlet plenum does not result in amplification of the swirl as can be seen in Fig. 18. Again this is due to the high temperatures and ionization levels encountered by the flow before the cathode tip. We must emphasize that we do not believe this to be a true representation of the arcjet. Had we treated the inlet boundary conditions accounting for ohmic heating, the

temperature and ionization level would be far lower, thus decreasing the viscosity by orders of magnitude below the level for this case.

As far as the effects of swirl are concerned, the present cold flow results appear to simulate real arcjet flows better. Amplification of swirl near the cathode tip would be beneficial in providing much needed cooling to confine and maintain the arc spot attachment area.

6 Summary & Conclusions

Both cold flow and ionizing flow in an arcjet thruster have been successfully simulated. These simulations provide insight as to the effects of boundary conditions on the results and serve to identify the behavior of the injected swirl at the inlet. It is clear that swirl injection (both magnitude and location of the maximum) is intimately tied to two key design parameters: the operating mass flow rate and the distance from the inlet plenum to the beginning of the converging section.

Improvements are certainly in adequately specifying the inlet boundary conditions, and conservative treatment of the ohmic heating certainly would be one. A two-temperature model along the lines of Miller et al. [5] could be an improvement for arcjets operating on monatomic propellants or hydrogen. However, the two-temperature treatment is suspect in the case of arcjets operating on ammonia or hydrazine due to the presence of large amounts of N_2 and other diatomic species [12]. Further work incorporating non-Maxwellian distributions of the EEDF would be essential for ammonia and hydrazine arcjets.

ACKNOWLEDGEMENTS

This work was supported by the Air Force Office of Scientific Research under Grant No.

AFOSR 91-0313. We also gratefully acknowledge a grant from the Ohio Supercomputer Center for use of their Cray Y-MP. Helpful discussions with Prof. Briley of Mississippi State University are gratefully acknowledged.

References

- [1] Briley, W. R, and McDonald, H. "Solution of the Multidimensional Compressible Navier-Stokes Equations by a Generalized Implicit Method", *Journal of Computational Physics*, Vol. 24, 1977, pp. 372-397.
- [2] MacCormack, R. W. "A Numerical Method for Solving the Equations of Compressible Viscous Flow", Paper AIAA-81-0110, presented at the AIAA 19th Aerospace Sciences Meeting, January 12-15, 1981, St. Louis, Missouri.
- [3] Beam, R. M and Warming, R. F. "An Implicit Factored Scheme for the Compressible Navier-Stokes Equations", *AIAA Journal*, 16, No. 4, pp. 393-402, 1978.
- [4] Rhodes, R., and Keefer, D., "Numerical Modeling of an Arcjet Thruster", paper AIAA-90-2614, presented at the 21st International Electric Propulsion Conference, July 18-20, 1990, Orlando, Florida.
- [5] Miller, S. A., and Martinez-Sanchez, M., "Multifluid Nonequilibrium Simulation of Electrothermal Arc-jets", paper AIAA-93-2101, presented at the AIAA/SAE/ASME/ASEE 29th Joint Propulsion Conference and Exhibit, June 28-30, 1993, Monterey, California.
- [6] King, D. Q., and Butler, G. W., "Modeling and Measurement of N₂ Arcjet Performance", paper AIAA-90-2616 presented at the 21st International Electric Propulsion Conference, July 18-20, 1990, Orlando, Florida.
- [7] Butler, G. W., Kashiwa, B. A., King, D. Q., "Numerical Modeling of Arcjet Performance", paper AIAA-90-1474 presented at the AIAA 21st Fluid Dynamics, Plasma Dynamics, and Lasers Conference, June 18-20, 1990, Seattle, Washington.
- [8] Auweter-Kurtz, M., Kurtz, H. L, Schrade, H. O and Sleziona, P. C. *Journal of Propulsion and Power*, 5, No. 1, pp. 49-55, 1989.
- [9] Okamoto, H., Nishida, M., and Tanaka, K., "Numerical Studies of the Flow Field in a Low Power DC Arcjet Thruster Using Navier-Stokes Equations", Paper IEPC-91-112, Presented at the 22nd International Electric Propulsion Conference, October 14-17, 1991, Viareggio, Italy.
- [10] Krier, H., and Burton, R., AFOSR Contractors Meeting, Atlantic City, New Jersey, June, 1993.
- [11] Subramaniam, V. V., and Lawless, J. L., "Electrode-adjacent boundary layer flow in magnetoplasma dynamic thrusters", *Physics of Fluids*, Vol. 31, No. 1, pp. 201-209, 1988.
- [12] Babu, V., and Subramaniam, V. V., "Vibrational Non-equilibrium in Arcjet Flows", Paper IEPC-93-129, Presented at the 23rd International Electric Propulsion Conference, September 13-17, 1993, Seattle, Washington.
- [13] Mitchner, M., Kruger, C. H., "Partially Ionized Gases", Wiley, 1973.
- [14] Anderson, D. A, Tannehill, J. C and Pletcher, R. H. *Computational Fluid Mechanics and Heat Transfer*, Hemisphere Publishing Corporation, Washington, 1984.

- [15] Isaacson, E and Keller, H. B., *Analysis of Numerical Methods*, Wiley, New York, 1966.
- [16] Darwell, H. M and Badham, H. "Shock Formation in Conical Nozzles", *AIAA Journal*, 1, No. 8, pp. 1932-1934, 1963.
- [17] Cuffel, R. F, Back, L. H and Massier, P. F. "Transonic Flowfield in a Supersonic Nozzle with Small Throat Radius of Curvature", *AIAA Journal*, 7, No. 7, pp. 1364-1366, 1969.
- [18] Back, L. H and Cuffel, R. F. "Detection of Oblique Shocks in a Conical Nozzle with a Circular-Arc Throat", *AIAA Journal*, 4, No. 12, pp. 2219-2221, 1966.
- [19] Back, L. H, Massier, P. F and Cuffel, R. F. "Flow Phenomena and Convective Heat Transfer in a Conical Supersonic Nozzle", *Journal of Spacecraft*, 4, No. 8, pp. 1040-1047, 1967.

30-kW Arcjet Geometry

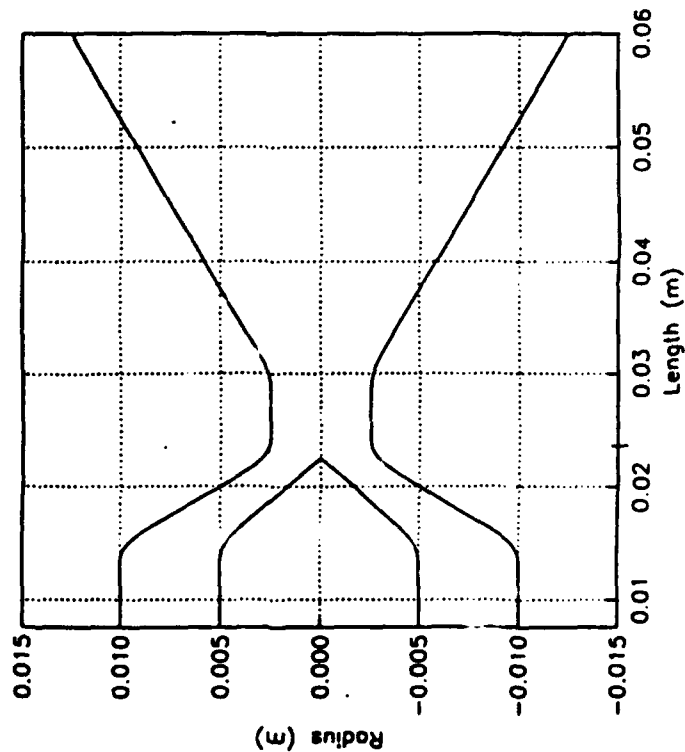


Fig. 1: Schematic of the nominal 30 kW arcjet geometry. The C-D nozzle is the same as this geometry, but without the inlet plenum or the constricter.

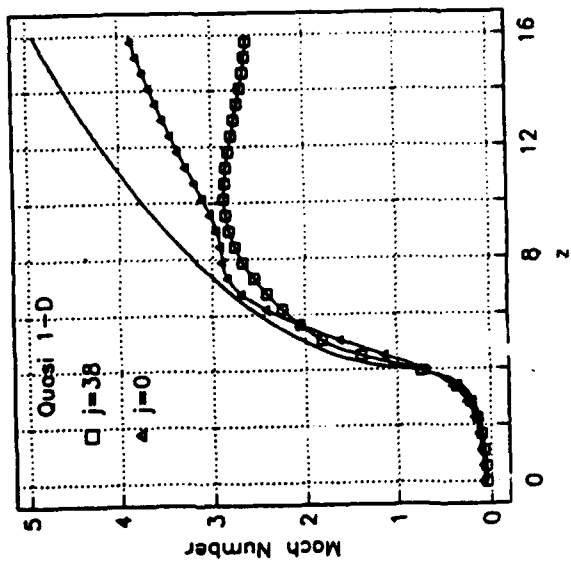


Fig. 2: Mach number is shown here for $j=0$ (centerline), and $j=38$ (near the anode) versus the streamwise coordinate.

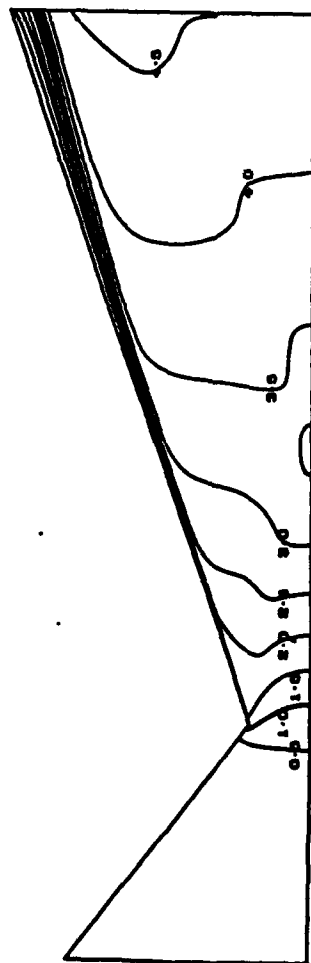


Fig. 2 Mach contours for the case of the high mass flow rate (g/s) in the C-D nozzle.

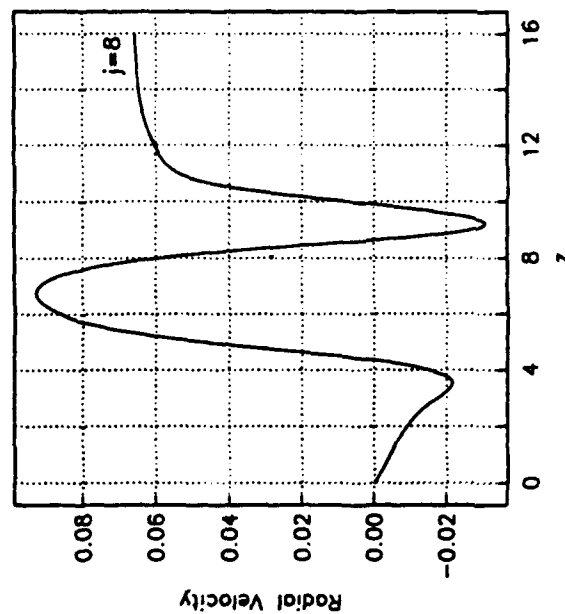


Fig. 4 Profile of the radial component of velocity versus the streamwise coordinate is shown here at $j=8$ (8 grid points above the centerline). Note the dramatic flow turning.

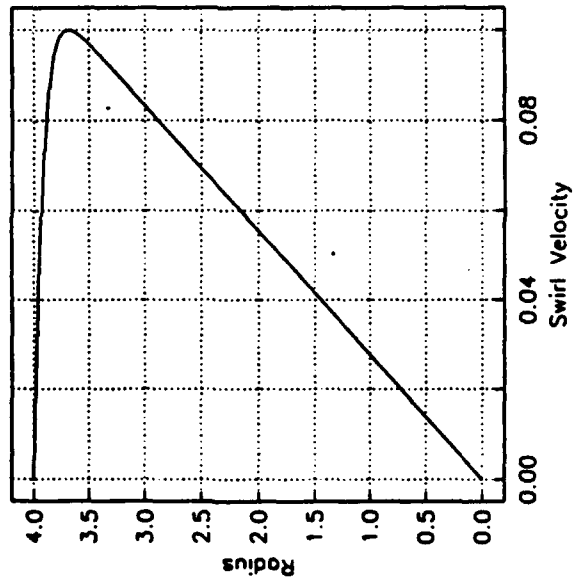


Fig. 5: Profile of the swirl (azimuthal) component of velocity introduced at the inlet.

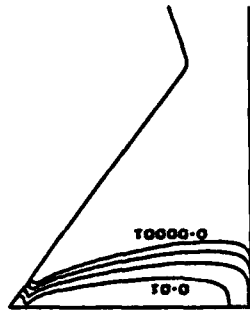


Fig. 6: Contours of the swirl component of velocity for the 30 KW arcjet geometry for high mass flow rates (g/s). Note the rapid decay of the injected swirl.

30-kW Arcjet Geometry



Fig. 7: Contours of the swirl component of velocity for the 30 kW arcjet geometry for low mass flow rates (mg/s). Note the persistence of the swirl through the entire flow field, and its amplification in the constrictor region. Note also the presence of swirl at the exit plane.

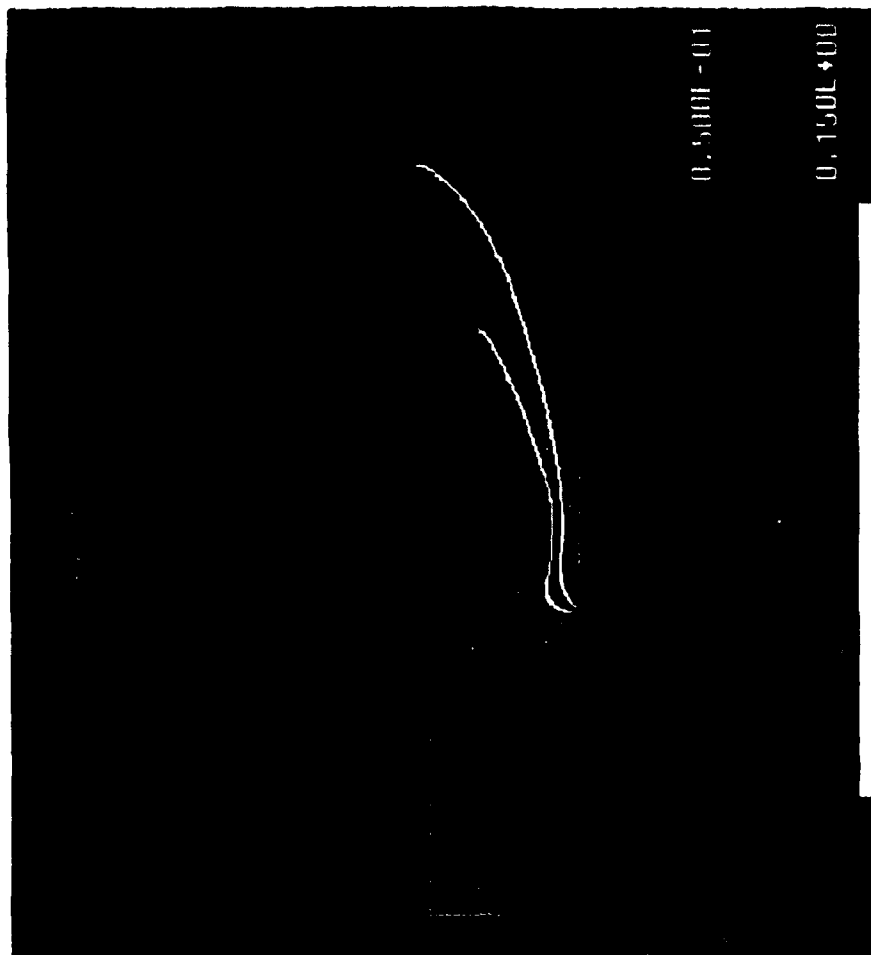


Fig. 8: Contours of current initially prescribed.

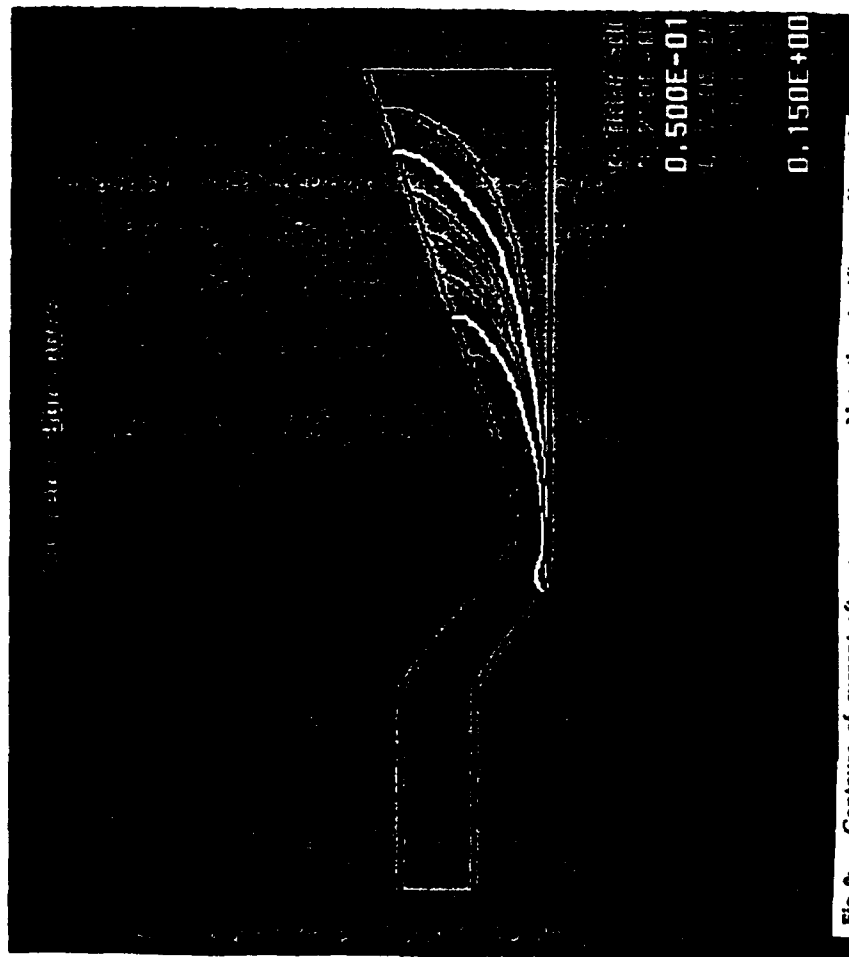


Fig. 9: Contours of current after convergence. Note the significant effect of electrical conductivity, especially in shifting the current distributing further downstream along the anode, as well as in concentrating the current along the centerline in the constriction. This case corresponds to Ar, 50 A, and a mass flow rate of ~ 100 mg/s.

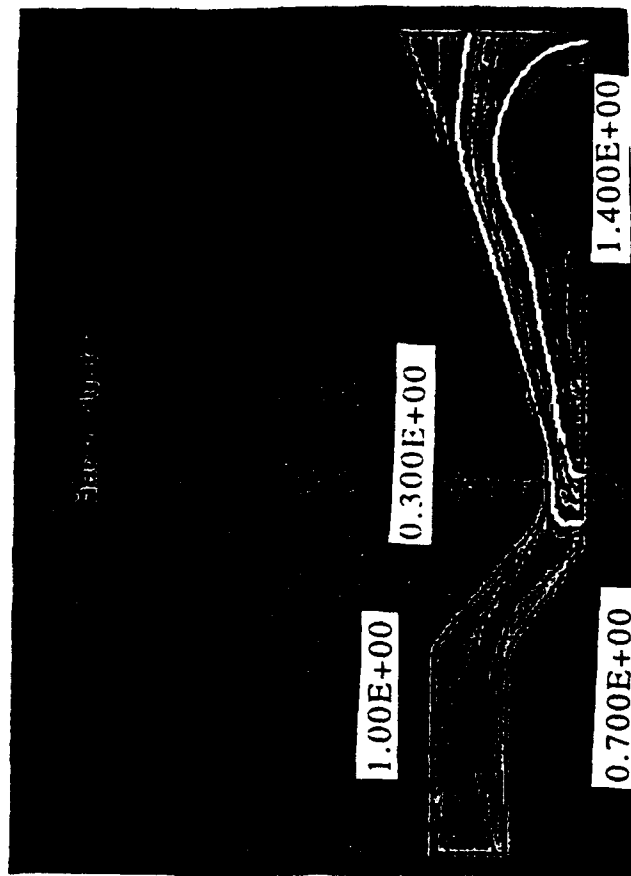


Fig. 10: Contours of Mach number for case of Ar, 50 A, and ~ 100 mg/s. The highest Mach contour is the bubble in the nozzle section, with a value of 1.4.

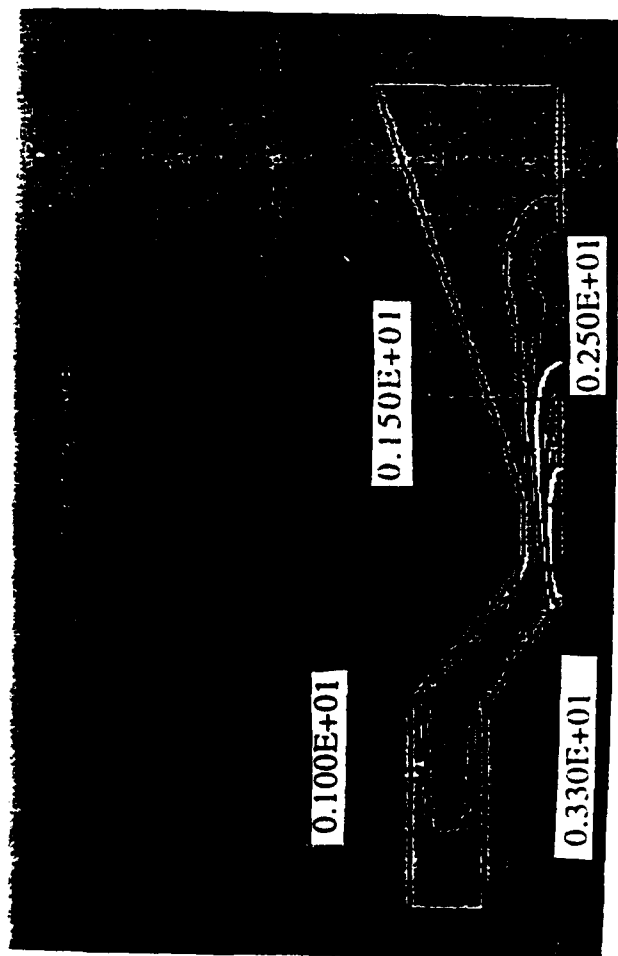


Fig. 11: Contours of temperature (normalized by 10,000 K) for Ar, at 50 A, and ~100 mg/s.

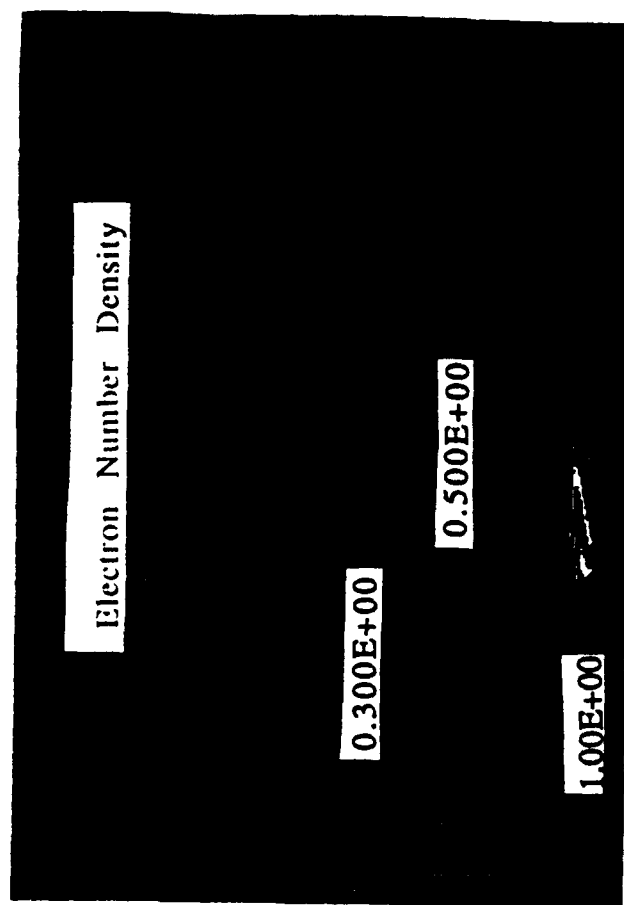


Fig. 12: Contours of electron number density (normalized by 2.1×10^{22}) for Ar, at 50 A, and ~100 mg/s.

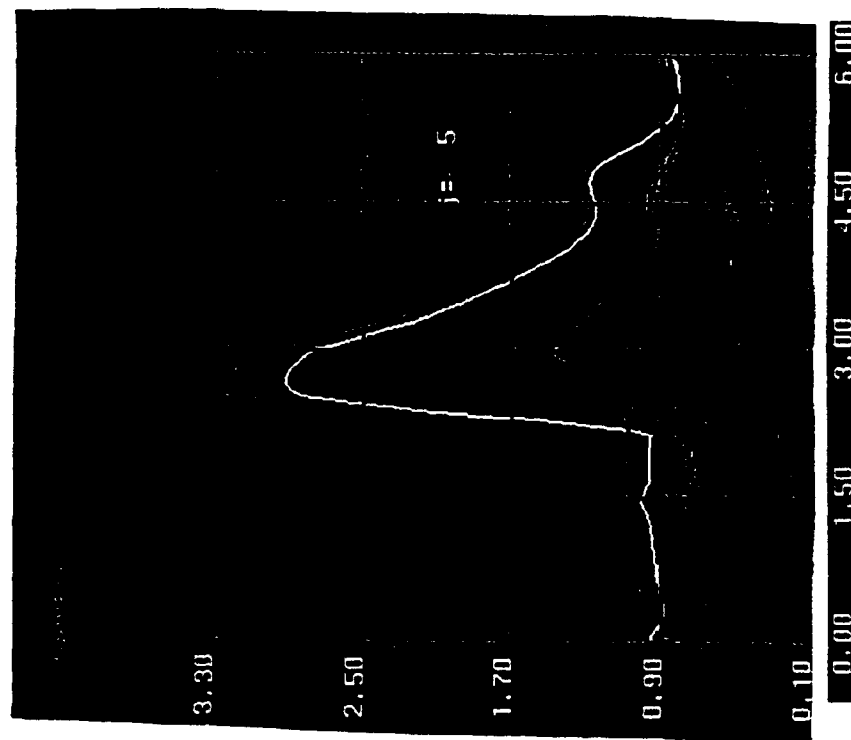


Fig. 15: Profile of temperature (normalized) versus streamwise coordinate at various radial stations (j).

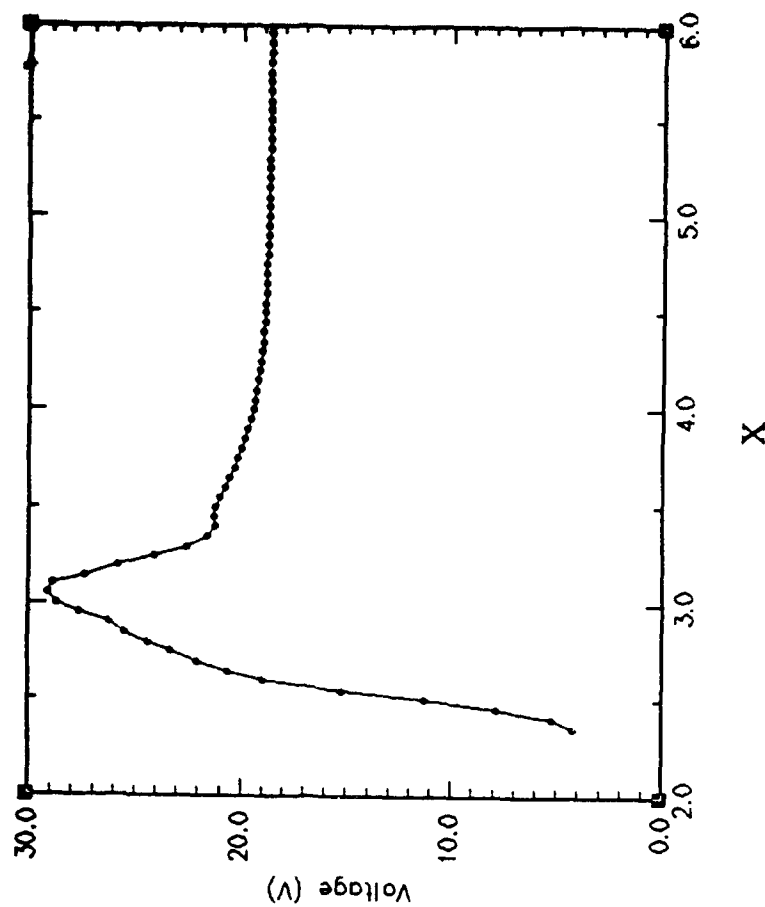


Fig. 16: Profile of voltage versus streamwise coordinate (normalized by $L=0.01$ m). This profile was computed by integrating the electric field from the cathode tip, along the centerline to various locations along the anode.

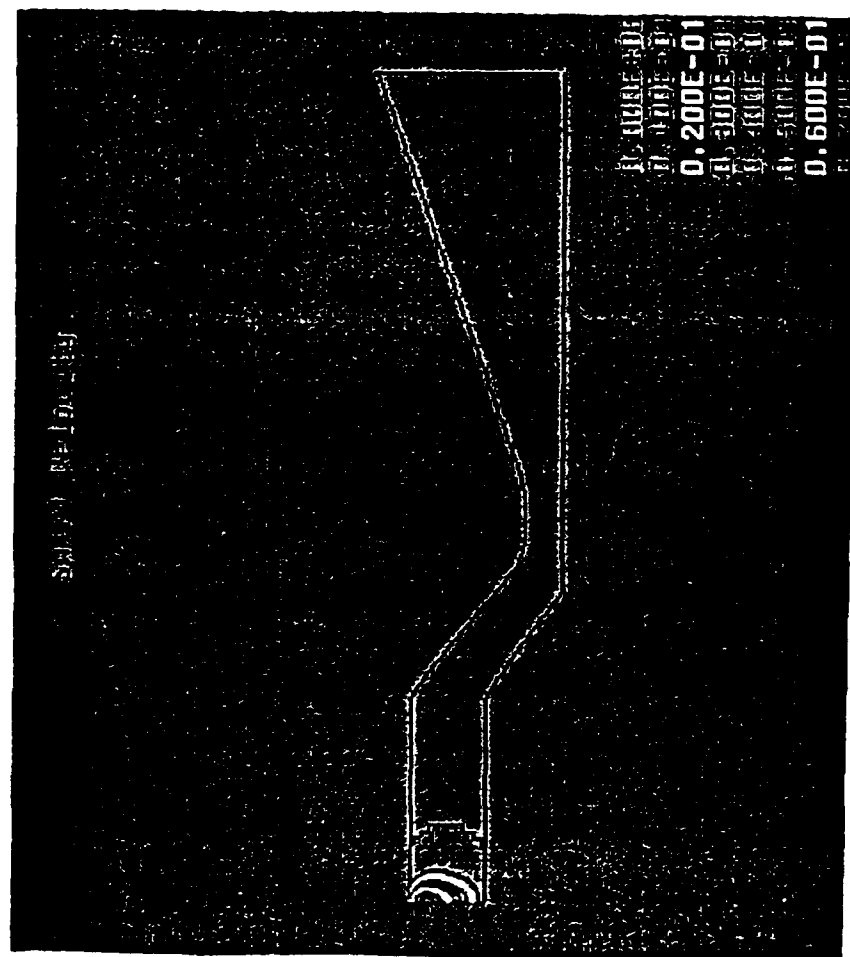


Fig.17: Contours of swirl (the swirl component of velocity is normalized by 1861 m/s) for Ar, at 50 A, and ~100 mg/s for the inlet swirl profile shown in Fig. 5

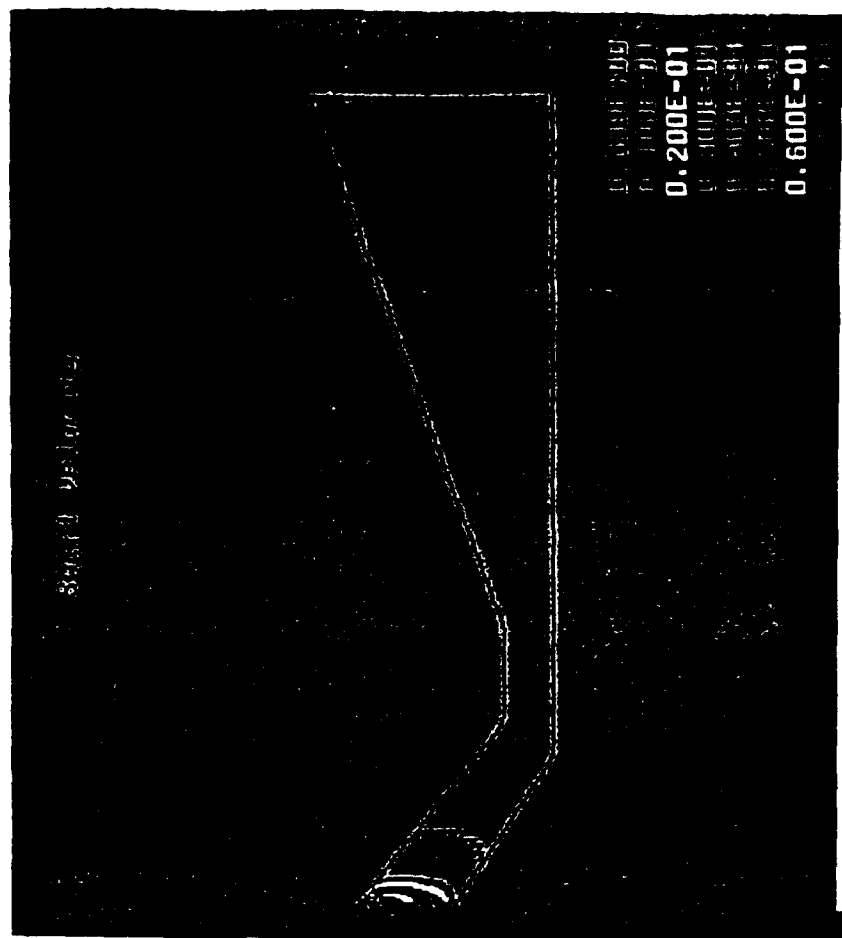


Fig.18: Contours of swirl (normalized) for Ar, at 50 A, and ~100 mg/s for the inlet swirl profile shown in Fig. 5. This is the case of the 30 KW arcjet geometry but with no inlet plenum.

Approved for public release;
distribution unlimited.

AIR FORCE OF SCIENTIFIC RESEARCH (AFSC)
NOTICE OF TRANSMITTAL TO DTIC

This technical report has been reviewed and is
approved for public release IAW AFR 190-12
distribution is unlimited.

Joan Boggs

STINFO Program Manager